EPFL

Development of Lamb wave resonators in thin film X-cut lithium niobate

Présentée le 27 janvier 2021

à la Faculté des sciences et techniques de l'ingénieur
Laboratoire de systèmes nano-électromécaniques
Programme doctoral en microsystèmes et microélectronique

pour l'obtention du grade de Docteur ès Sciences

par

Muhammad FAIZAN

Acceptée sur proposition du jury

Prof. J. Brugger, président du jury
Prof. L. G. Villanueva Torrijo, directeur de thèse
Dr A. Reinhardt, rapporteur
Dr V. Plessky, rapporteur
Prof. A. Skrivervik, rapporteuse

■ École
polytechnique
fédérale
de Lausanne

2021

Acknowledgments

Doing a PhD is like riding a roller coaster of emotions where if a successful experiment takes you to the moon, the next failed one will bring you back to the earth as quickly. It is fun, if done in the company of like-minded colleagues and a supportive supervisor, and I had been lucky in both regards.

First, I would like to thank my PhD supervisor, *Prof. Luis Guillermo Villanueva* for his invaluable technical guidance and unwavering personal support throughout the duration of my PhD. One of his best qualities is to sincerely listen to the student's problems and advise accordingly. His inspiring personality gave me the confidence to face the hard challenges and keep pushing forward in the tough times. I am honored to be one of his PhD students and I will always carry with me the valuable lessons taught during these four years.

I am thankful to all the former and current members of ANEMS lab for their companionship and camaraderie. Special shout out to *Annalisa* and *Andrea* for guiding me through the initial challenges of the PhD. I had quality time with *Tom, Marsha, Seniz, Kaitlin, Damien, Soumya, Marco, Daniel, Rebecca, Giulia* and *Silvan*, including all the interesting lunchtime discussions.

I am truly blessed to have the best parents (*Najib* and *Farhat*) in the world. Their prayers and rock-solid support have always guided me through the twists and turns of life. What I have achieved or will achieve, my parents will always have a major contribution in that.

This acknowledgment would not be complete without the mention of my beautiful 1-year old daughter, *Minahil*. She brought a completely new dimension in my life that I did not know existed. For me, COVID-19 lockdowns were a blessing in disguise where I got to spend quality time with my daughter. I enjoyed her first roll, first sit up, first stand up, first crawl and first walk. On the other hand, writing a PhD thesis locked in an apartment with the one year old would test every ounce of your patience. Thanks to my daughter figuring out that by touching the keyboard, something happens on the screen, I might have some typos.

Last but not the least, I am greatly thankful for my wife *Anam* who left her medical practice in Pakistan for me and joined me in this crazy and uncertain adventure. Not a day goes by that I am not grateful to have her in my life. Alongside her, I am excited to have finished this chapter of my life and to start the new one.

Abstract

Microelectromechanical systems (MEMS) is among the most revolutionary technologies of 21st century, with the applications ranging from industrial systems to consumer electronics. Using MEMS in battery-powered wireless devices has long been seen as the evolutionary step in achieving a highly miniaturized and efficient RF frontend (RFFE) for the next generation of communication systems. Piezoelectric MEMS resonators are the essential component of every RFFE as they do a phenomenal job of frequency generation and filtering while meeting the stringent specifications regarding power budget and form factor.

This thesis focuses on the design, fabrication and characterization of Lamb wave resonators on thin film LN for RF filters and oscillators. The goal of the project is to improve the electromechanical coupling (k_t^2) and quality factor (Q) of the resonators by first selecting an appropriate LN cut and in-plane device orientation for the intended mode and secondly, by optimizing different geometrical parameters such as electrode coverage (duty factor), gap, bus and anchor dimensions.

With the goal to improve k_t^2 of the resonator, we fabricate devices with varying electrode coverages from 20% to 70% for Al and Pt electrodes. Our results show that low electrode coverages (20% to 40%) do not have significant effect on k_t^2, but for higher electrode coverages (> 40%), k_t^2 reduces by ~35% due to the non-linear increase in static capacitance (C_o). The electrode material does not show any significant dependence on k_t^2 but devices with Al electrodes show larger Q (in our case x2) than devices with Pt electrodes due to higher resistive losses. We demonstrate devices with the highest reported k_t^2 of 31% and 40% for S0 and SH0 mode resonators with Q of 720 and 590, operating at around 500 MHz and 300 MHz, respectively, in X-cut LN.

In our next effort to further enhance Q, we fabricate devices by varying the geometrical dimensions of different inactive region elements such as anchor, bus and gap of the resonator. Each element plays a very important role in containing energy within the resonator cavity resulting in Q improvement. Our measurements suggest that a square anchor ($L_a = W_a$), a wider bus ($W_b > 0.3\lambda$) and a longer gap ($g = 2\lambda$) helps to improve Q of the resonator. The highest Q of 1900 and k_t^2 of 41% is achieved for the design parameters of $g = 2\lambda$, $W_b = 3\lambda/4$, $W_a = 3\lambda/4$ and $L_a = 3\lambda/4$, resulting in the highest-ever achieved Figure-of-Merit (FoM) of 780 for SH0 mode resonators in X-cut LN.

We also demonstrated the fabrication of high performance A1 mode resonator operating in 3-6 GHz range in Z-cut LN. Our fabricated devices exhibit k_t^2 and Q up to 28% and 300, respectively. This performance is in agreement with the FEM simulations and is suitable for the 5G RF-filter technology.

Lastly, we use 2-port SH0 mode resonators to build oscillators and measure phase noise (PN) as it directly relates to its frequency stability. We investigate the dependence of PN on carrier power, Q and k_t^2 by measuring the PN for 60 oscillators using different SH0 mode resonators. Our results show that a higher carrier power and Q significantly reduces PN and improves frequency stability of the oscillator, whereas k_t^2 does not show significant influence on PN. We achieve a low phase noise of -96 dBc/Hz and -129 dBc/Hz, at the offset frequency of 1 kHz and 10 kHz, respectively, for the resonator with Q of 2500.

Keywords:

Lithium niobate	Lamb wave resonators	E-beam lithography	Quality factor
Oscillators	Phase noise	Filters	Piezoelectricity

Résumé

Les systèmes microélectromécaniques (MEMS) font partie des technologies les plus révolutionnaires du 21e siècle, dont les applications vont des systèmes industriels à l'électronique grand public. L'utilisation des MEMS dans les appareils sans fil alimentés par batterie est considérée depuis longtemps comme une étape évolutive dans la réalisation d'un frontal RF (RFFE) hautement miniaturisé et efficace pour la prochaine génération de systèmes de communication. Les résonateurs MEMS piézoélectriques sont le composant essentiel de chaque RFFE car ils accomplissent un travail phénoménal de génération de fréquence et de filtrage tout en respectant les spécifications strictes concernant le budget d'énergie et le facteur de forme.

Cette thèse se concentre sur la conception, la fabrication et la caractérisation de résonateurs à onde de Lamb sur ces couches minces de niobate de lithium (LN) pour les filtres et oscillateurs RF. Le but du projet est d'améliorer le couplage électromécanique (k_t^2) et le facteur de qualité (Q) des résonateurs en sélectionnant d'abord une coupe LN appropriée et une orientation du dispositif dans le plan pour le mode prévu et ensuite, en optimisant différents paramètres géométriques tels que la couverture des électrodes (facteur de service), l'espacement, les dimensions du bus et de l'ancrage.

Dans le but d'améliorer k_t^2 du résonateur, nous fabriquons des dispositifs avec des couvertures d'électrodes variables de 20 à 70 % pour les électrodes en aluminium (Al) et platine (Pt). Nos résultats montrent que les faibles couvertures d'électrodes (20 % à 40 %) n'ont pas d'effet significatif sur k_t^2, mais pour les couvertures d'électrodes plus élevées (>40 %), k_t^2 diminue de ~35 % en raison de l'augmentation non linéaire de la capacité statique (C_o). Le matériau des électrodes ne présente pas de dépendance significative par rapport à k_t^2, mais les dispositifs avec des électrodes en Al présentent un Q plus important (dans notre cas x2) que les dispositifs avec des électrodes en Pt en raison de pertes résistives plus élevées. Nous démontrons les dispositifs avec les k_t^2 les plus élevés rapportés de 31% et 40% pour les modes S0 et SH0 avec un Q de 720 et 590, fonctionnant à environ 500 MHz et 300 MHz, respectivement, en LN dans une coupe X.

Dans notre prochain effort pour améliorer encore le Q, nous fabriquons des dispositifs en faisant varier les dimensions géométriques de différents éléments de la région inactive tels que l'ancre, le bus et l'espace du résonateur. Chaque élément joue un rôle très important en contenant l'énergie dans la cavité du résonateur, ce qui permet d'améliorer le Q. Nos mesures suggèrent que des ancres carrées ($L_a = W_a$), un bus plus large ($W_b > 0.3\lambda$) et une fente plus longue ($= 2\lambda$) contribuent à améliorer le Q du résonateur. Le Q le plus élevé de 1900 et k_t^2 de 41% sont atteints pour les paramètres de conception de $g = 2\lambda$, $W_b =$

$3\lambda/4$, $W_a = 3\lambda/4$ et $L_a = 3\lambda/4$, ce qui donne le chiffre de mérite (FoM) le plus élevé jamais atteint de 780 pour les résonateurs en mode SH0 dans la coupe X LN.

Nous avons également démontré la fabrication d'un résonateur haute performance en mode A1 fonctionnant dans la gamme 3-6 GHz en LN dans la coupe Z. Nos dispositifs fabriqués affichent k_t^2 et Q jusqu'à 28% et 300, respectivement. Cette performance est en accord avec les simulations FEM et convient à la technologie du filtre RF 5G.

Enfin, nous utilisons des résonateurs à 2 ports en mode SH0 pour construire des oscillateurs et mesurer le bruit de phase (*phase noise*, PN) car il est directement lié à la stabilité du résonateur en fréquence. Nous étudions la dépendance du PN par rapport à la puissance de la porteuse, Q et k_t^2 en mesurant le PN pour 60 oscillateurs utilisant différents résonateurs en mode SH0. Nos résultats montrent qu'une puissance porteuse et un Q plus élevés réduisent considérablement le PN et améliorent la stabilité de la fréquence de l'oscillateur, alors que k_t^2 ne montre pas d'influence significative sur le PN. Nous obtenons un faible bruit de phase de -96 dBc/Hz et -129 dBc/Hz, à la fréquence de décalage de 1 kHz et 10 kHz, respectivement, pour le résonateur avec Q de 2500.

Mots-clés:

Niobate de lithium	Résonateurs à ondes de Lamb	Lithographie par faisceau d'électrons	Facteur de qualité
Oscillateurs	Bruit de phase	Filtres	Piézoélectricité

Contents

List of Figures

1 Introduction

Communication and connectivity with the distant parties has always been a very important aspect of human life. Over time, we have invented different ways of communication starting from smoke signals and pigeon mails to all the way to mobile, satellite and web communication. The 21st century of hyper-connected world is dependent on the reliable and efficient functioning of billions of devices connected together and sharing information for day-to-day operations of the society. The number of devices connected to the internet grew from 15 billion devices in 2015 to 30 billion devices in 2020 with the forecast projecting over 75 billion devices connected by 2025 (Figure 1.1a) [1]. The phenomenal growth and adoption of smart phones, laptops and tablets and rise of Internet of things (IoT) are the main drivers of this parabolic growth of connected devices. More connected devices translate to more data generation. The global internet traffic has increased three fold from 2015 to 2020 from 53.2 Exabytes data generated per month in 2015 to 161 Exabytes data generated per month in 2020, which is equivalent to burning data on 40 billion DvDs per month [2].

The use of broadband services such as sharing photos and clips and streaming high-resolution videos ''over the air'' using mobile data is a parabolic trend that will continue to rise in the decades to come, mainly driven by the increasing number of mobile phone subscriptions and data volume per subscription (Figure 1.1b) [3]. This explosive increase in data generation and transmission needs to be supported by the communication infrastructure that requires next generation of networks with higher frequency bands to be deployed every ten years. The currently used 3G and LTE bands are over congested and unable to provide the required bandwidth and high-speed internet needed for different smartphone apps. Fifth generation (5G) of networks is the next step in the evolution of communication infrastructure that will be deployed in the next 3-5 years with the goal to support the ever-growing number of new users while providing low latency and high bandwidth to all the connected devices. The dual connectivity of LTE and 5G bands demand a dramatic evolution of Radio Frequency Front End (RFFE) architecture and additional on board components. The mobile phone RFFE and WiFi sector is expected to grow from $15 billion in 2017 to $35 billion in 2023 [4]. Among different components, RF filters are expecting the biggest market growth due to the presence of 100+ filters in the 5G RFFE architecture for addressing different frequency bands (Figure 1.1c). For this reason, a modern communication device needs a cost effective, miniaturize and power efficient RFFE that can pack 100's of electronic components such as amplifiers, RF filters, mixers and antennas.
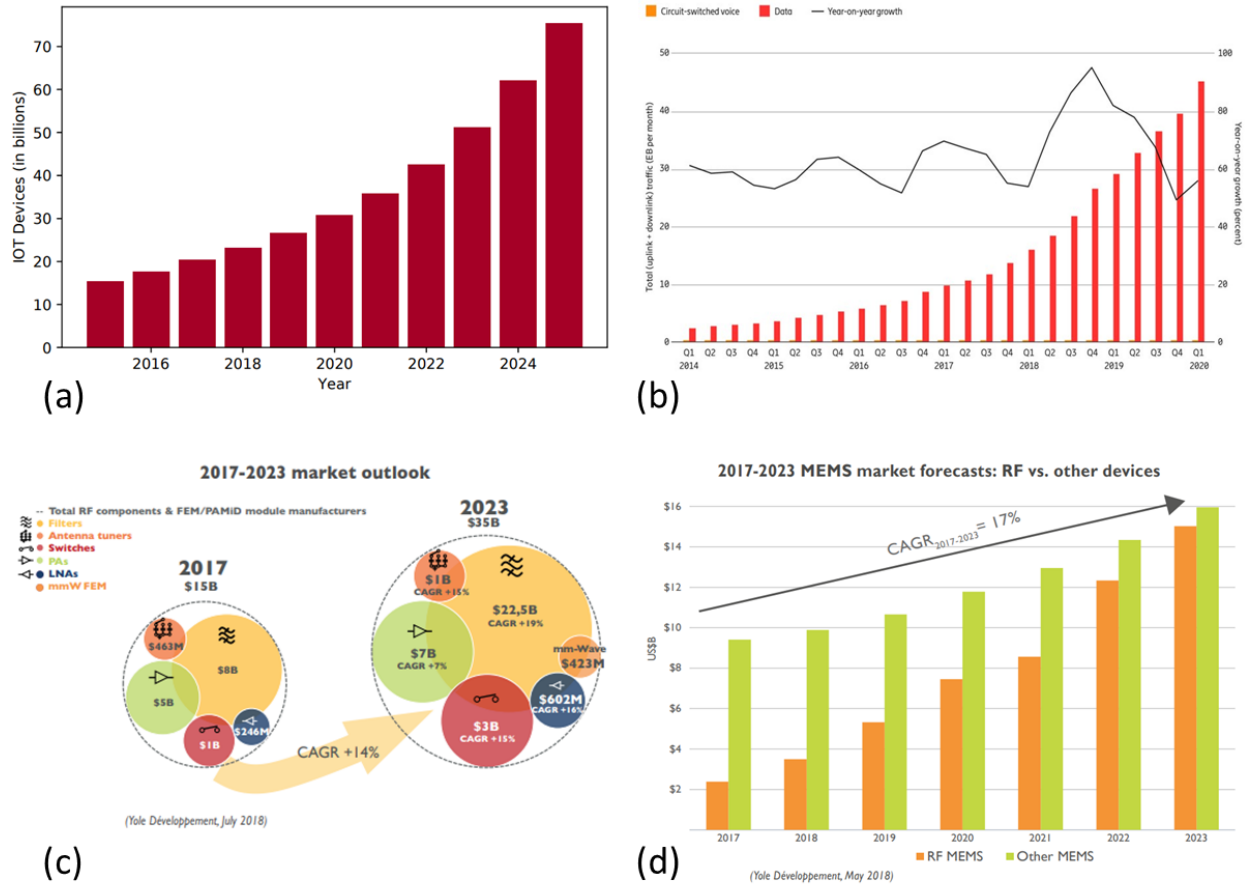
Figure 1.1: (a) Forecast suggesting a parabolic increase in connected devices to the internet with estimated 75 billion connected devices in 2025. (b) Global mobile network data traffic showing a huge demand for data as compared to voice calls [3]. (c) Enormous increase in revenue for different category of RFFE components due to the emergence of 5G technology [4]. (d) Growth of RF MEMS sector year-over-year with respect to the whole MEMS industry [5].

Microelectromechanical Systems (MEMS) is a technology that enables the large-scale production of highly miniaturized and cost effective devices. MEMS components can be monolithically integrated with the on board electronics and provides a complete system on-chip solution that can interact with the physical world, perform computation and communicate with other devices [6]. MEMS technology is already used for variety of industrial applications such as airbag sensors [7][8], pressure sensors [9], inject nozzles [10], MEMS microphones [11] and micro-optics [12]. However, the Market and Technology report published by Yole in 2018 declared RF MEMS the largest growing segment of MEMS industry (Figure 1.1d) [5]. RF

MEMS technology enables the production of miniaturized and high performance communication modules such as RF filters, MEMS switches, MEMS oscillators, high quality factor (Q) inductors and resonators with frequency scalability to ultra and super high frequency bands (< 30 GHz) [13][14]. Now a day, every smartphone contains MEMS filters for frequency control and filtering purposes and the need to pack more number of filters in RFFE is only going to increase due to the emergence of 5G technology. Therefore, the use of MEMS acoustic devices such as Surface Acoustic Waves (SAW) and Bulk Acoustic Waves (BAW) for RF filters due to their small form factor and power efficiency has emerged as the most viable solution to address the ever-growing demand for higher number of frequency bands [15].

The present day RFFE employs a super-heterodyne architecture that involves the frequency up conversion (transmitter end) and frequency down conversion (receiver end) of the baseband signal to an intermediate frequency (IF) which eases the processing of the signal such as filtering, amplification and modulation/demodulation. These tasks are achieved by mostly using off-chip components that takes sizeable portion of the board and drives up the overall cost of the RFFE. However, many of these components can be replaced by the implementation of on-chip RF MEMS components such as MEMS resonators which can enable a paradigm shift in transceiver architecture with highly configurable and tunable filter and oscillator modules [16]–[19]. Figure 1.2 shows the system-level block diagram of super-heterodyne receiver with coloured sub-blocks that can be replaced by the RF MEMS components as well as a modified receiver architecture featuring highly configurable blocks entirely implemented using high Q MEMS resonators. The modified blocks include (1) an RF frontend multi-channel selector with several filtering functions consisting of 100's of high Q switchable MEMS resonators. (2) Highly tunable local oscillator consisting of bank of MEMS resonators for switching from one oscillation frequency to another thus supporting wide range frequencies that can be handled by the mixer while achieving excellent phase noise performance and eliminating the need for power hungry phase locking circuits. (3) MEMS resonator based mixer-filter block capable of up- and down-converting signals along with band pass filtering on a single chip allowing higher level of system integration at the lower cost [20][21].

MEMS resonators based on thin-film lithium niobate (LN) technology for filtering and timing applications has been a topic of intense research both in academia as well as in industry due to high Q and electromechanical efficiency (k_t^2) of LN resonators. High Q directly translates to low insertion loss for the filters resulting in longer battery life for mobile hands and high k_t^2 yields wider bandwidth, a highly desirable feature especially for 5G supported bands (n77, n78 and n79) [22]. Whereas, in MEMS based oscillators high Q resonators leads to low phase noise performance while offering multiple frequencies of

operation on a single chip [23]. Among different types of LN acoustic resonators, SAW, BAW and Lamb wave resonators are the most popular and extensively used for the above-mentioned applications [24]. A detailed description of LN based SAW, BAW and Lamb wave resonator along with its laterally vibrating and thickness dependent modes will be presented in the next section.
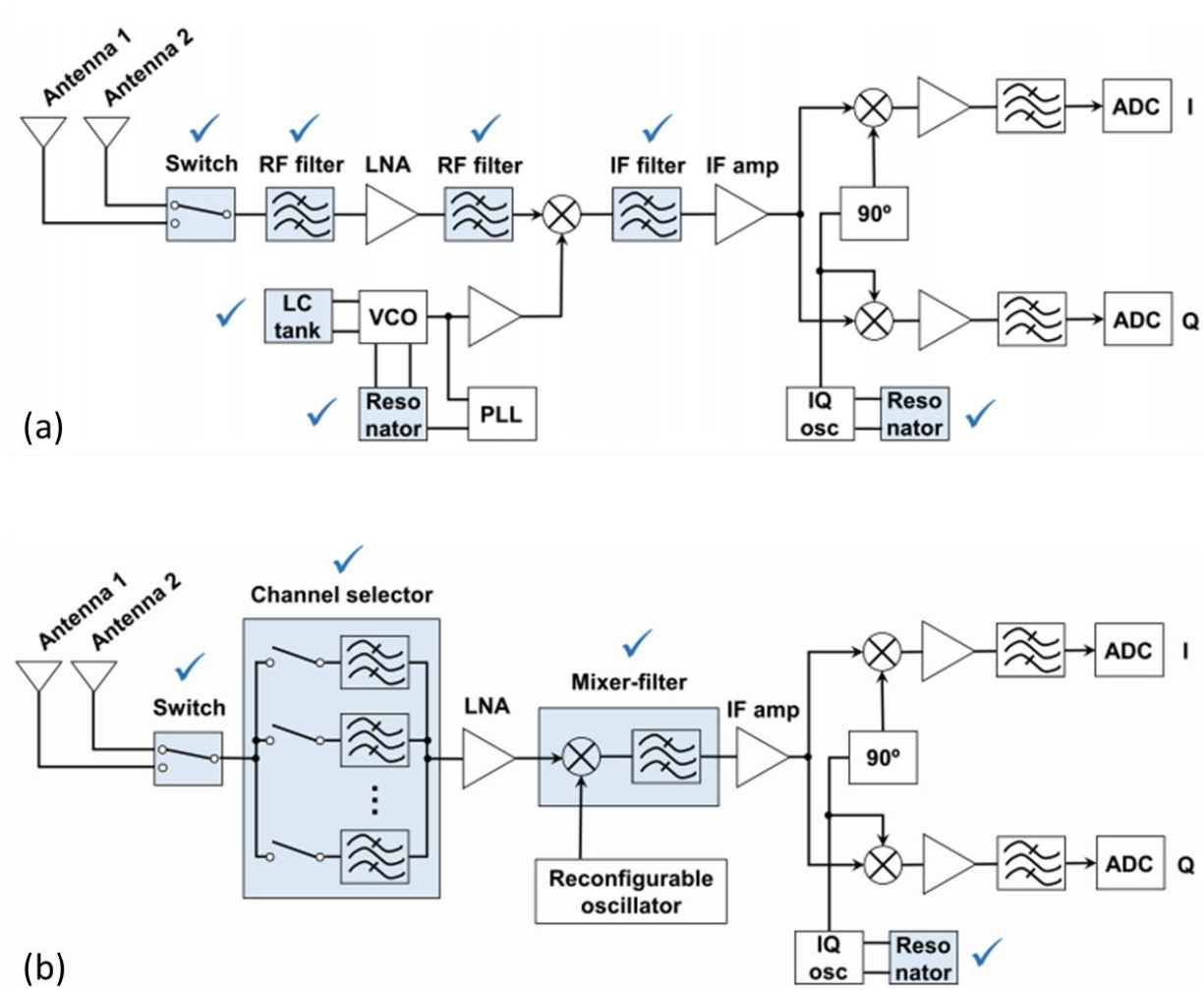
Figure 1.2: Expected evolution of RF frontend architecture with the advancement of RF MEMS technology. (a) Block diagram of a super-heterodyne receiver highlighting elements that can be replaced by high performance RF MEMS components. (b) Block diagram of a modified super-heterodyne receiver with multi-channel selector, reconfigurable oscillator and mixer-filter blocks consisting of 100's of high Q MEMS resonators.

4

1.1 Lithium niobate-based SAW and BAW resonators

As we are moving towards 5G communication systems, MEMS-based electroacoustic technology is being rapidly used to satisfy the stringent requirements of high frequency filtering and control. The main reason for this is that, the velocity of sound in solid materials is $\sim 10^5$ times slower than the speed of light in air, yielding acoustic wavelength of only a few microns at 1GHz operational frequency. This enables electro-acoustic devices with extremely small sizes to be built, making them suitable for filters and delay lines in modern mobile phones. Commercially, there are two electroacoustic technologies available to do said tasks. One is Surface Acoustic Wave (SAW) and the other is Bulk Acoustic Wave (BAW) technology, both of which are used in a concurrent manner. Conventionally, SAW devices use lithium niobate and lithium tantalate as the piezoelectric material whereas BAW devices are based on AlN. SAW technology is widely used in different applications ranging from few MHz to 2 GHz, while higher frequency bands are dominated by BAW devices [15].

SAW is a mechanical wave which mostly propagates through the material surface. It looks similar to ripple on water surface. Indeed, in SAW devices, the wave amplitude decays exponentially in the vertical direction, leaving the energy confined very close to the surface. SAW devices consist of a single crystal piezoelectric material such as quartz, lithium niobate (LN) or lithium tantalate (LT). They use a comb-shaped interdigitated transducer (IDT) on the top of the piezo substrate to transduce electrical into acoustic energy and vice versa. The frequency of a SAW device is determined by the lateral distance between the comb fingers (pitch) and can therefore be lithographically adjusted to yield multiple frequency devices on the same die. It also uses periodic gratings known as Bragg reflectors at both ends of the IDT to reflect acoustic energy and trap it in the IDT region thus minimizing energy loss and improving the quality factor. Figure 1.3 shows the illustration of a SAW device with an input IDT used to generate SAW on piezo substrate and an output IDT to detect and convert SAW back into the voltage. An array of shorted electrodes on both edges of the device behaves like mirrors to reflect SAW, creating a resonator cavity.

SAW devices' performance severely degrades as the operational frequency goes above 2 GHz. A higher frequency corresponds to a smaller pitch and narrower electrodes, which not only pushes the desirable resolution of optical lithography to its limits but also questions the power handling capability of the device. Narrow comb fingers have to carry large current densities, and this can cause problems like overheating and electromigration [25] whereas a small pitch makes the device vulnerable to electrostatic discharge [26]. Even more importantly, the mechanical losses in narrow fingers devices are very important since it

becomes increasingly difficult to generate surface waves and not have them leak into the substrate. However, a variant of SAW technology, I.H.P SAW (Incredibly high performance SAW) has demonstrated excellent performance by confining the acoustic energy in the vicinity of surface by using multi-layered structure consisting of a piezoelectric layer, a functional layer and a higher velocity layer on top of a substrate (for example, $LiNbO_3$/SiO_2/AlN/Si substrate) resulting in higher electromechanical efficiency and quality factor and smaller TCF (temperature coefficient of frequency) [27].
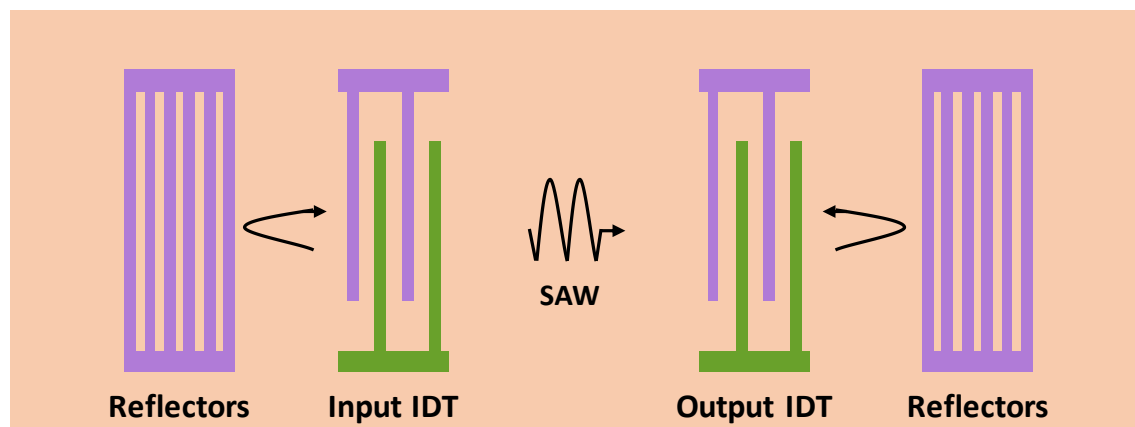
Figure 1.3: Top-view schematic of a SAW resonator with input and output IDTs to excite and detect SAW modes respectively. An array of floating electrodes known as SAW reflectors on both edges of the device traps acoustic energy and forms a resonator cavity.

BAW resonators use a thin layer of piezoelectric material sandwiched between two metal electrode layers for transduction of thickness modes. Unlike SAW resonators, a standing wave is generated in the vertical direction within the thin piezo layer. The resonance frequency of BAW resonators is mostly determined by the thickness of the piezo layer. This allows the fabrication of high frequency devices (> 2 GHz) by depositing a thin piezo layers (thinner than 2 μm). As a result, it is difficult to have wide range of frequency devices on the same wafer, since the thickness of the deposited layer are for the most part very difficult to be modified. BAW resonators also show an excellent power handling capability, as there are no small features prone to failure due to electromigration and overheating. We can classify BAW resonators according to the way that they avoid acoustic leakage to the substrate, which is either by being suspended

on a micro-machined membrane known as Film Bulk Acoustic Resonator (FBAR), or by being solidly mounted on acoustic reflectors known as Solidly Mounted Resonator (SMR) [28]–[30].

In the first case, where all three layers form a membrane or they are deposited on a supporting membrane layer, can be seen in Figure 1.4a. The presence of air on top and bottom of the resonators helps to achieve a high quality factor as the acoustic impedance of air is 10^5 times lower than of solid materials, limiting the flow of energy. The second type, where the piezo stack is placed on top of several layers with alternating values of high and low acoustic impedance known as acoustic mirrors, is schematically shown in Figure 1.4b. Each layer in the acoustic mirror is a quarter wavelength thick and the ensemble acts as a Bragg's reflector. The acoustic wave is reflected from every interface between the different acoustic impedance layers and adds up in phase at the resonator cavity [31][32]. SMR have an excellent heat dissipation capability, as there is a direct heat path through the mirrors down to the substrate acting as a heat sink [33].
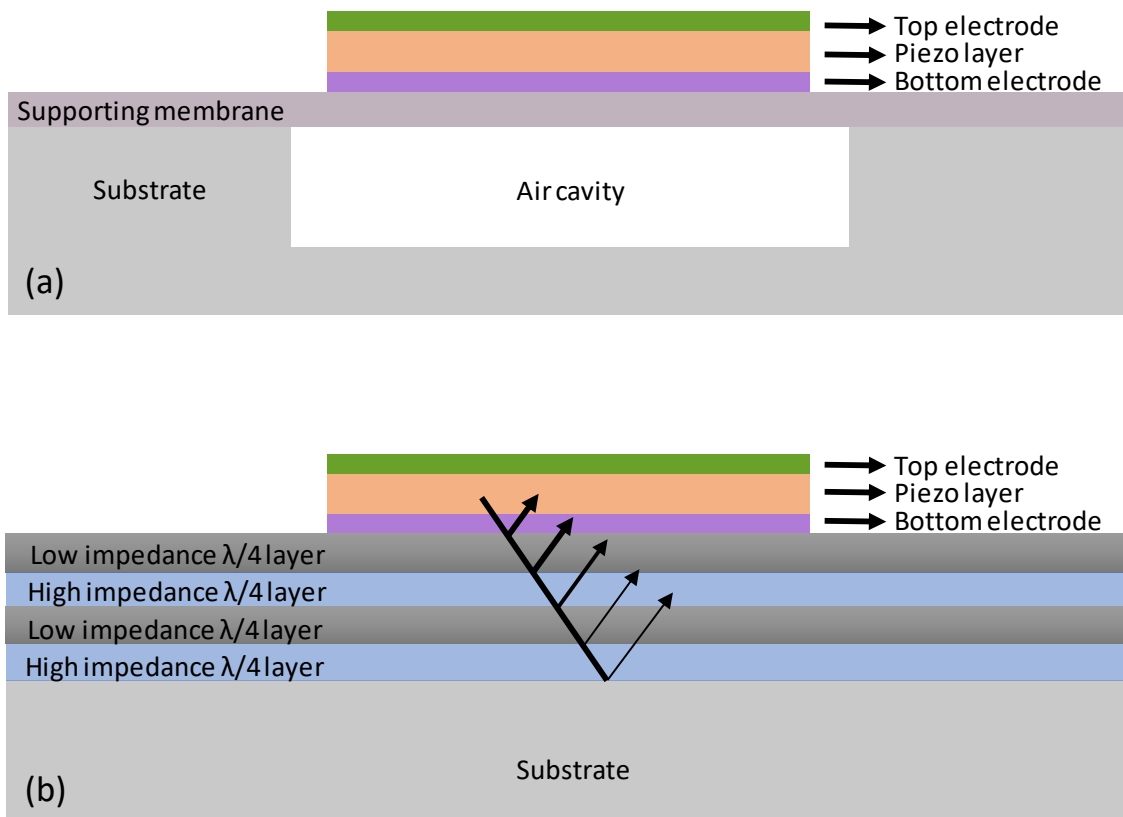
Figure 1.4: Schematic cross section of (a) membrane-type BAW resonator with piezo stack suspended on a membrane and (b) solidly mounted BAW resonator with piezo stack placed on acoustic mirrors.

1.2 Lithium Niobate based Lamb wave resonators

Learning from the above-mentioned mature technologies, there is an emerging class of electroacoustic resonators known as Lamb wave resonators that combine the advantages of SAW and BAW devices while addressing the problem of low resonance frequency limitation faced by SAW, and multiple frequency devices restriction faced by BAW resonators [34]. Lamb wave resonator consists of an IDT (similar to SAW) on top of a mechanically suspended thin film of piezoelectric material (similar to BAW) tethered to the substrate via anchors (typically two). IDT fingers are made of metal and are alternatively connected to two values of potential, for example, the signal and the ground. When RF potential is applied to the electrode fingers, the electric field develops inside the piezoelectric material from high to low potential electrode and consequently the material is deformed. The induced electric field generates acoustic standing waves in the resonator cavity that ultimately excites symmetrical (S), shear horizontal (SH) and asymmetrical (A) modes in the resonator. For the laterally vibrating modes such as S and SH modes, the resonance frequency (f_s) of the device to the first approximation is set by the distance between the IDT's fingers know as pitch (p):

$$f_s = \frac{v}{2p} \tag{1.1}$$

where v is the acoustic velocity of the excited mode. Depending on the piezo plate thickness to wavelength ratio (h/λ), nth order lamb wave modes represented as Sn, SHn and An are supported. For ultra-thin piezo plate ($h = 0.02 - 0.2\lambda$), only the lowest order modes are observed. S0, SH0 and A1 modes in LN plate have a weak dispersion, a high acoustic velocity and a large electromechanical coupling as compared to their higher order modes making them more interesting for communication applications [35].

1.2.1 Lithium Niobate as a piezoelectric material

Lithium niobate (LN) has been used in acoustic devices for several decades. It gained tremendous popularity due to its pronounced piezoelectric and electro-optical properties. Nowadays, SAW and BAW

devices are implemented in many communication systems as filters and delay lines. Recently, researchers have started to explore Lamb wave modes in LN thin film to be used in MEMS resonators.

LN is a highly anisotropic material, and its acoustic properties change with respect to the direction of the acoustic wave propagation in different LN cuts. Typically, LN is grown as a single crystal along z-axis and later it is sliced in different cuts. This provides an additional degree of freedom for designing acoustic devices and achieving higher electromechanical coupling for certain acoustic modes [36]. Commonly used nomenclature for different cuts such as X-cut, Y-cut and Z-cut represents x, y and z-axis being normal to the surface of the wafer, respectively. However, it is possible to achieve LN wafers with virtually any axis being perpendicular to the surface, for example the cut (XZ 30°) is achieved by rotating X-cut 30° about z-axis as shown in Figure 1.5a.

The rigidity matrix (c), piezoelectric coupling matrix (e), and dielectric matrix (ε) are among the most important material properties of LN. They dictate the overall electromechanical coupling, acoustic velocity, and resonance frequency of the device. Most of the time, suppliers only provide the material properties of Z-cut of LN, which is a typical cut for the growth of LN crystal. Therefore, Euler angle transformation can be performed to attain the material properties of other orientation cuts. Cartesian coordinates (x, y, z) are rotated sequentially by Euler angles (φ, θ, ψ) based on z-x-z convention where the x-y-z frame is rotated first about the z-axis by an angle φ then about the new x-axis by an angle θ and then about the rotated z-axis by an angle ψ, as shown in Figure 1.5b. Material properties for different cuts can be achieved by using following transformation equations for matrix rotation:

$$c' = M.c.M^T \tag{1.2}$$

$$e' = a.e.M^T \tag{1.3}$$

$$\varepsilon' = a.\varepsilon.a^T \tag{1.4}$$

where c', e', ε' are stiffness, piezoelectric and dielectric rotated matrixes of the desired LN cut and c, e and ε are un-rotated matrixes or typically matrixes of Z-cut LN. M and a are bond and transformation matrixes , respectively, that can be obtained using Euler angles pertaining to the desired cut [37].
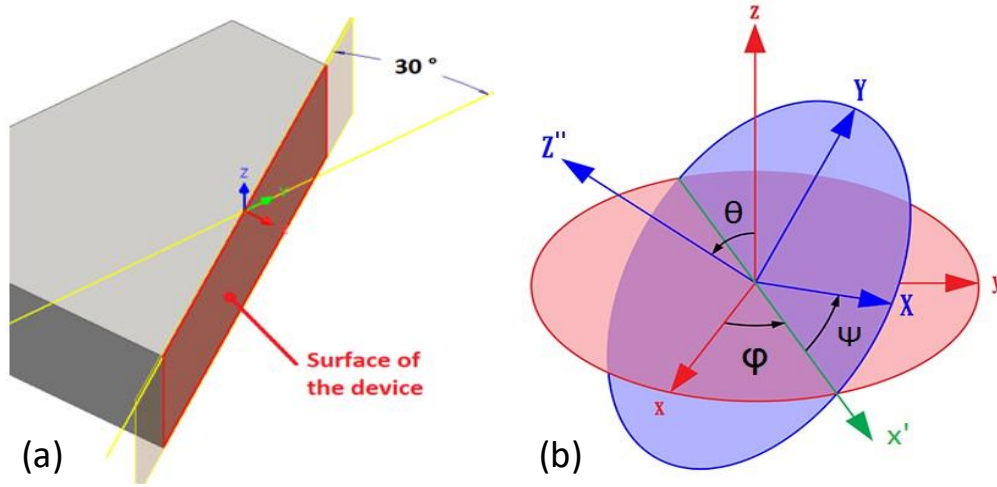
Figure 1.5: (a) Highlighted red surface representing XZ 30° cut after rotation from Z-cut. (b) Schematic diagram of planer surfaces showing Euler angle (φ, θ, Ψ) transformation of the Cartesian coordinates (x, y, z)

1.2.2 Symmetrical mode (S0) resonator

An S0 mode resonator is also known as a contour mode resonator that consists of an IDT on top of a suspended thin film of LN utilizing piezoelectric coefficient e_{x1} to generate a lateral mode with x being the orientation of E-field. For S0 mode resonators without the bottom metal, the applied electric field and the resulting strain are both in the longitudinal direction (x-axis). The highly anisotropic nature of LN requires the correct selection of LN cut and in-plane device orientation to maximize the electromechanical coupling for S0 mode.

The highest electromechanical coupling of S0 mode in X-cut LN is achieved with the in-plane device orientation of 30° from y-axis [38]. The in-plane device orientation means fabricating a device in such a way that the lateral vibration of electrodes is at 30° from the position of the positive y-axis of LN wafer as shown in Figure 1.6. This can be verified by using the transformation equations (Eq. 1.2-1.4) to calculate elastic-stiffness, piezoelectric coupling and dielectric matrixes from 0° to 180° in X-cut LN and using the following equation:

$$K^2 = \frac{e_{11}^2}{c_{11} \times \varepsilon_{r11}\varepsilon_0} \tag{1.5}$$

Where e_{11}, c_{11} and ε_{r11} represents the piezoelectric coefficient, stiffness coefficient and relative permittivity coefficient when the applied electric field and resulting strain in the device are in lateral direction (x-axis). K^2 represents the intrinsic electromechanical coupling of a piezoelectric material and is independent of resonator's geometry.
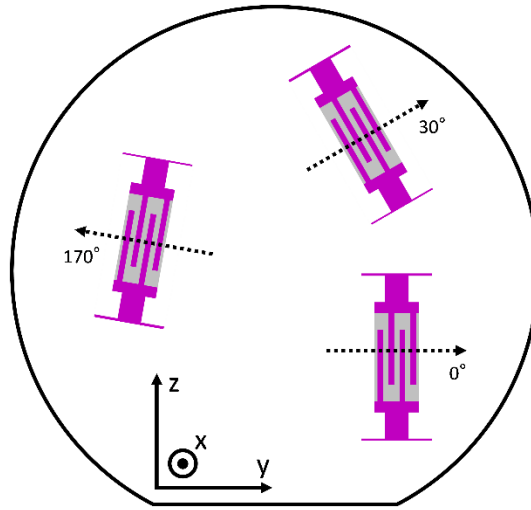
Figure 1.6: Schematic illustration of X-cut LN wafer with x-axis perpendicular to the yz plane. Devices are oriented at specific angles with respect to wafer's flat (y-axis) in order to maximize K^2 for the intended mode. K^2 for S0 and SH0 modes is enhanced with device orientation of 30° and 170° respectively.
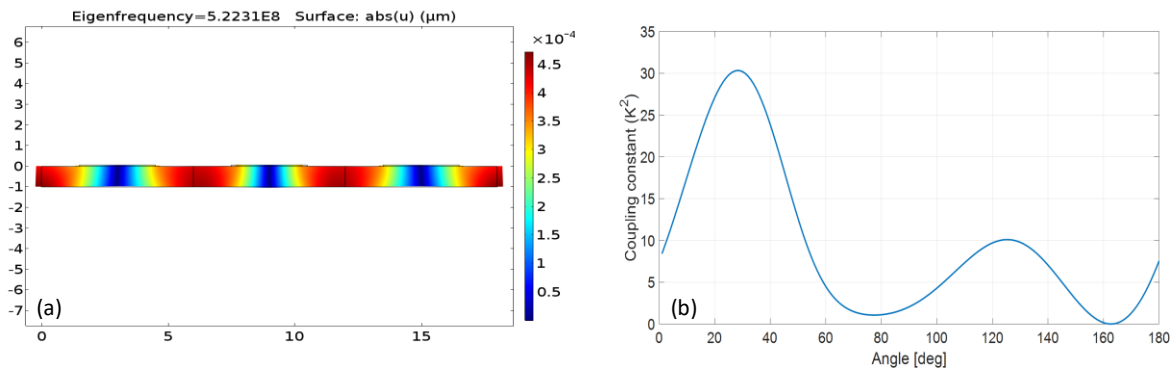
Figure 1.7: (a) 2D simulation of S0 mode with three electrode fingers where blue and red portions represent compression and expansion, respectively. The mode only exits in longitudinal direction. (b) Graph

illustrating piezoelectric coupling constant of S0 modes as a function of in-plane device orientation in X-cut LN plate. Highest K^2 is obtained at 30°.

Figure 1.7a shows the S0 mode shape in 2D model where red and blue colours show lateral expansions and contractions respectively. Fig. 1.7b shows K^2 of S0 mode as the in-plane orientation of the device changes from 0° to 180° in X-cut LN. It can be seen that the maximum coupling constant ($K^2 \sim 31\%$) is obtained with an orientation of 30° which is in close agreement with the reported results.

1.2.3 Shear Horizontal (SH0) mode resonator

Just like a conventional contour (S0) mode resonator, SH0 mode can be generated with a similar geometry configuration but with a different in-plane device orientation. In X-cut LN, SH0 mode is predominantly produced with device orientation 170° from y-axis. In a 2-D rectangular plate, symmetrical modes are mainly excited by generating acoustic waves in longitudinal direction only but shear horizontal modes are the result of superposition of acoustic waves generated in both longitudinal and transverse directions (Figure 1.8a) [39]. As a result, resonance frequency (f_s) of SH0 mode is set by the set by the IDT pitch (p) and the length of the resonator (L) is given as:

$$f_s = v \times \sqrt{\left(\frac{1}{2p}\right)^2 + \left(\frac{1}{2L}\right)^2} \approx \frac{v}{2W_p} \tag{1.6}$$

where v is the acoustic velocity with the typical value of around 3800 m/s for SH0 mode in X-cut LN. For $L \gg p$, the f_s is mainly determined by the p of the resonator, allowing frequency diversity on a single wafer. Figure 1.8b shows the maximum achievable coupling constant (K^2) of SH0 mode as a function of in-plane device orientation. Our theoretical model for SH0 mode resonator shows the same dependence of K^2 for different in-plane orientation angles, as indicated by other works [38],with the maxima at 170° to y-axis. However, our absolute value of K^2 is significantly larger than the ones previously reported and hence, it requires further investigation.
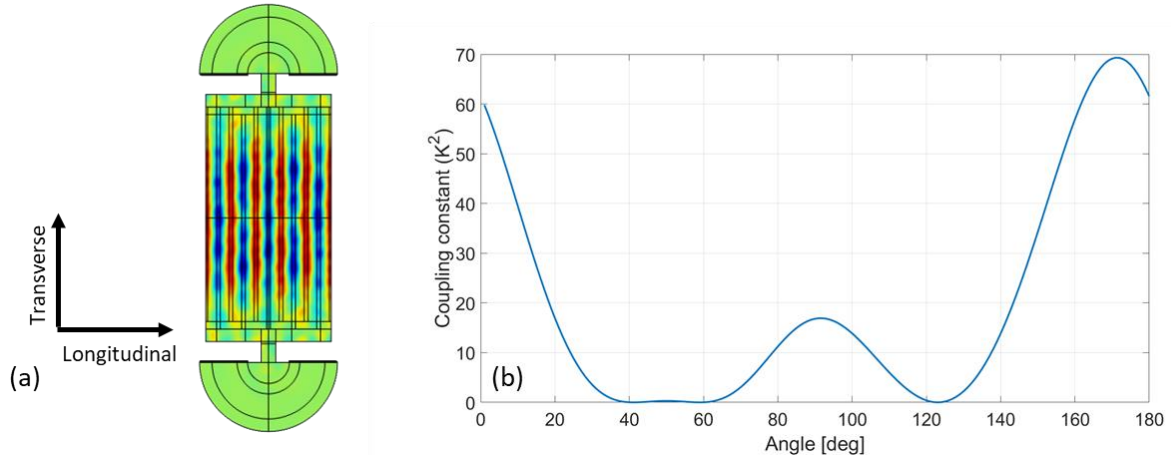
Figure 1.8: (a) 3D simulation of SH0 mode where blue and red portions represent the deformation in y-plane. The mode exits in longitudinal as well as in transverse direction. (b) Graph illustrating piezoelectric coupling constant of SH0 mode as a function of in-plane device orientation in X-cut LN plate. Highest K^2 is obtained at 170°.

1.2.4   Asymmetrical mode (A1) resonator

Asymmetrical modes, also referred as thickness modes are generated by using IDT on top of a suspended plate of LN anchored to the substrate from all sides. By using IDT, the electric field is generated in the lateral direction with the resultant displacement in the vertical direction. Figure 1.9 shows the displacement mode shapes and stress distribution of the first seven modes (A1-A7) where even order modes have equal and opposite stress components that lead to zero electromechanical coupling as the resultant stress is negligible. On the other hand, odd order modes can be excited with a high coupling due to non-zero stress in the piezo plate [40]. The resonance frequency is mainly determined by the thickness of the piezoelectric layer and is expressed as:

$$f = \frac{v}{2t}$$
(1.7)

Where v acoustic velocity and t is the thickness of piezoelectric layer.
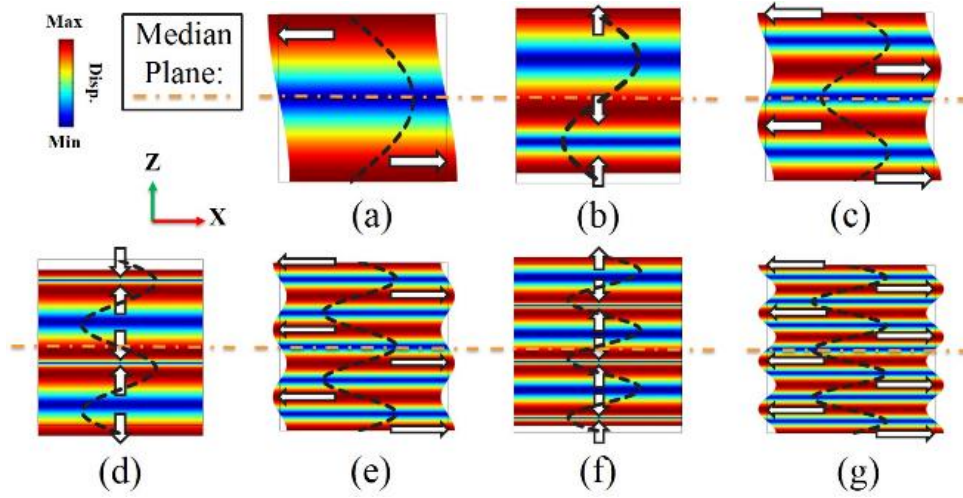
Figure 1.9: Asymmetrical mode shapes from (a) A1 mode − (g) A7 mode. The arrows represent the displacement field whereas black dashed line shows the stress distribution for each mode [40].

S0 and SH0 mode resonators have shown a great potential for enabling wideband RF filters due to their high electromechanical coupling and quality factor but suffer from degraded performance at 5G frequencies due to high electrical losses of narrow electrodes. On the other hand, first order asymmetrical mode (A1) in Z-cut LN plate is a thickness-dependent mode where the frequency is set by the thickness of piezo layer and can easily be scaled to 5 GHz range by using ultra-thin LN layer. It has a high acoustic velocity and a large electromechanical coupling that makes it suitable for the realization of high frequency and wideband devices [41].

1.2.5   Resonator geometry and characterization

The geometry of Lamb wave resonators, especially S0 and SH0 mode resonators consists of IDT on top of a suspended plate of piezoelectric material tethered from two ends known as anchors (Figure 1.10). Anchors are used to route electrical signal to the IDT via the buses. Similar to SAW devices, resonance frequency of the device is determined by the distance between the adjacent electrodes known as the pitch (p). The IDT consists of a number of electrode pairs (N_p) and two half electrodes on the free edges of the resonator. These half electrodes are designed to behave as $\lambda/4$ reflectors to enhance the fundamental mode and supress/reduce the unwanted modes. The other important design parameters of IDT are the metallization ratio or electrode coverage (EC), which is the ratio of electrode's width over

pitch; and the aperture, which is the overlap region of the electrodes. Both parameters affect the electromechanical coupling and quality factor of the resonator.

Several other parameters such as anchor length (L_a) and width (W_a), gap (g), metal thickness (t) and bus width (W_b) determine the overall mechanical stiffness of the resonator that ultimately affects its resonance frequency. The length of the resonator (L_{res}) is defined as the sum of the aperture, bus and gap: $L_{res} = L_a + 2(W_b + g)$; whereas the total number of electrode pairs and the two reflectors sets the width of the resonator (W_{res}), expressed as:

$$W_{res} = \frac{\lambda}{2}(N_p + 1) \tag{1.8}$$
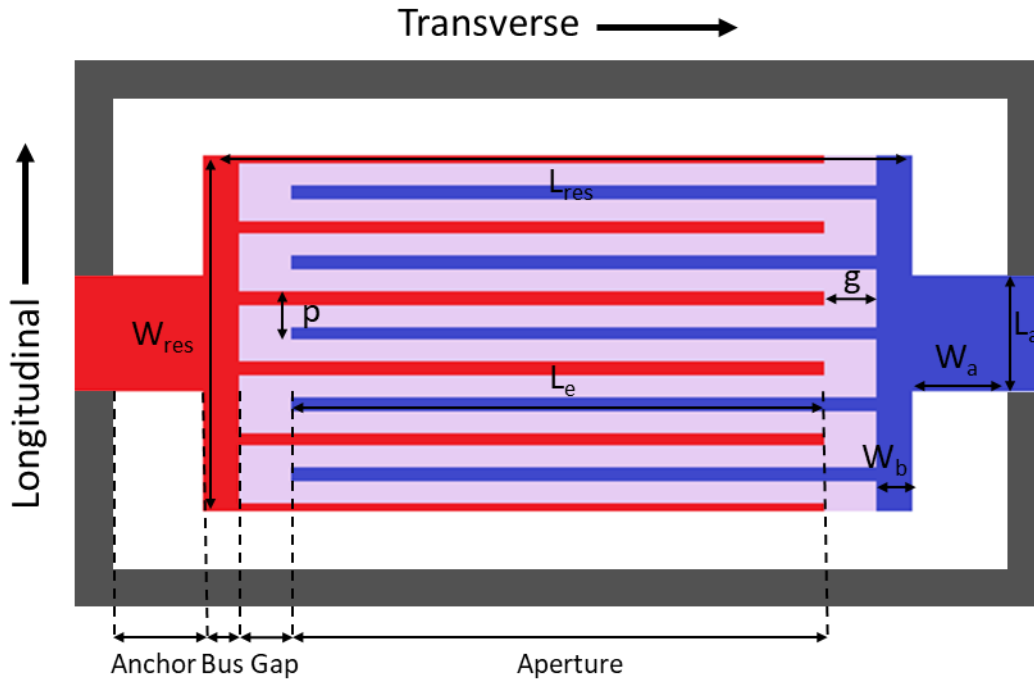
Figure 1.10: Top view of a S0 and SH0 mode resonator's geometry. Four important regions including anchor, bus, finger-to-bus gap and aperture are illustrated. Geometrical parameters affecting resonator's performance are resonator length (L_{res}) and width (W_{res}), anchor length (L_a) and width (W_a), gap (g), aperture (L_e), pitch (p) and bus width (W_b).

Lamb wave resonators can be characterized in 1-port or 2-port configurations [42]. When used as 1-port resonator, one port is connected with the signal while the other is grounded. The same first port is also used to readout the response from the resonator using the scattering parameter S_{11}. In 2-port configuration, one port is connected to the input signal while the other port is used for the readout. The transmitted power from one port is measured at the second port using the scattering parameter S_{21}. Figure 1.11a shows the schematic diagram of mBVD model for a 1-port resonator. It consists of a motional branch employing motional resistor (R_m), capacitor (C_m) and inductor (L_m) responsible for transducing mechanical motion and a parasitic branch consisting of static capacitance (C_o) and substrate losses (R_0). Ground-Signal-Ground (GSG) pads connected to the resonator are represented in mBVD model by R_s (series resistance of pads and electrodes) and C_p (capacitance offered by the pads) [43].

Figure 1.11b shows the admittance response (Y_{11}) of 1-port resonator with a resonance peak at frequency f_s and an anti-resonance peak at frequency f_p due to the presence of a parasitic branch in parallel with the motional branch. mBVD model is fitted with the admittance response of the resonator to find the important circuit parameters as expressed below:

$$C_m = \frac{8}{\pi^2} C_0 k_t^2 \tag{1.9}$$

$$R_m = \frac{1}{\omega_0 Q C_m} = \frac{\pi^2}{8} \frac{1}{\omega_0 C_0} \frac{1}{k_t^2 Q} \tag{1.10}$$

$$L_m = \frac{\pi^2}{8} \frac{1}{\omega_0^2 C_0} \frac{1}{k_t^2} \tag{1.11}$$

$$C_o = \frac{2\varepsilon_o \varepsilon_r L_e t}{\lambda(1 - EC)} \times (N_p + 1) \tag{1.12}$$
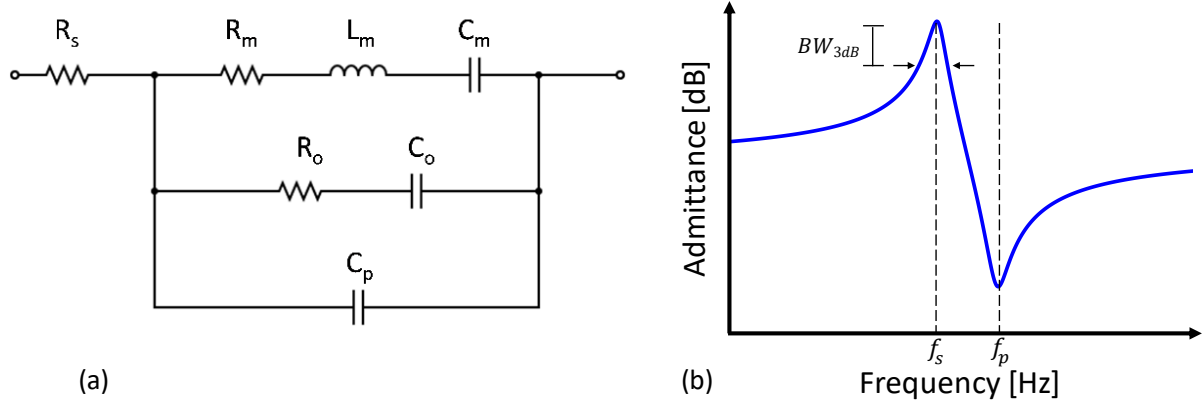
Figure 1.11: (a) Electrical representation of a Lamb wave resonator using mBVD model. R_m, L_m and C_m represents the motional parameters whereas R_0 and C_o represents the dielectric loss and static capacitance respectively. Parasitic capacitance due to pads and overall electrical losses are represented by C_p and R_s respectively. (b) Admittance curve (Y_{11}) shows the frequency response of a Lamb wave resonator where f_s and f_p are the resonance and anti-resonance frequencies used to calculate electromechanical coupling. Resonance peak (f_s) and its 3 dB bandwidth is used to determine quality factor.

1.2.6 Resonator performance and Figure of Merit (FoM)

Electromechanical coupling coefficient (k_t^2) and Quality factor (Q) are the two main parameters that are used to judge the performance of micro-resonators for different applications. For example, when used for RF filtering, the bandwidth, insertion loss and skirt steepness of a filter is governed by the coupling and the quality factor of the micro-resonators involved. k_t^2 shows the efficient conversion of energy between the electrical and mechanical domains, whereas Q indicates the rate of energy loss from the resonator cavity. For these reasons, the product of $k_t^2 \cdot Q$ is used as a Figure of Merit (FoM) of the resonator performance. For ultra-high frequency resonators (> 1Ghz), the FoM can be expressed as the product of $k_t^2 \cdot Q \cdot f$, where f is the resonance frequency of the resonator.

Electromechanical coupling

The constant pursuit to achieve a higher electromechanical coupling for MEMS resonators has always been the focus of research in next generation (5G) communication systems [44][45]. Several approaches

have been explored to optimize the coupling, either by structure optimization [46] or by utilizing materials with high piezoelectric coefficients such as AlScN, PZT and LiNbO₃.

Structure optimization includes proper selection of

(i) Device orientation when anisotropic piezoelectric material is used. For example, S0 and SH0 modes can be excited in X-cut LN plate with a high electromechanical coupling (30% for S0 mode and 40% for SH0 mode) with a device orientation of 30° and 170°, respectively

(ii) Substrate thickness to wavelength ratio (h/λ) as most of the energy is stored in fundamental modes in the ultra-thin piezoelectric plate ($h = 0.02 - 0.2\lambda$)

(iii) Electrode configuration by using optimum electrode coverage. For S0 and SH0 modes, the electrode coverage of 30% [47] and reflectors at the two free edges of resonator help to maximize electromechanical coupling [48].

In literature of acoustic MEMS, electromechanical coupling has been defined in many different ways yielding different formulas to calculate it [49]. The most commonly used forms are the piezoelectric coupling constant (K^2) and the electromechanical coupling coefficient (k_t^2). K^2 is a material-dependent parameter and sets the upper theoretical limit on the energy conversion efficiency of a resonator for a given piezoelectric material. It does not take in effect the resonator's design whereas k_t^2 is a design-dependent parameter. It gives the conversion efficiency of electrical energy into mechanical energy and vice versa, based on both the piezoelectric material and the geometry of the resonator. For example, length of the resonator, electrode coverage and aperture are a few of the geometrical parameters that can significantly affect k_t^2 but not K^2.

Two commonly used and equivalent formulas are reported to calculate k_t^2 , where one uses the difference between the resonance and anti-resonance frequencies of the admittance response (Figure 1.11b) while the other extracts k_t^2 from the electrical response of the resonator as the ratio between the motional and static capacitances of mBVD model (Fig. 10a) [50].

$$k_t^2 = \frac{\pi^2}{8} \times \frac{f_p^2 - f_s^2}{f_s^2} = \frac{\pi^2}{8} \times \frac{C_m}{C_o} \tag{1.13}$$

Quality factor

Quality factor is a dimensionless quantity and refers to the ability of a resonator to confine its mechanical energy during the oscillatory motion. Generally, quality factor is defined as the ratio of energy stored to the energy dissipated per cycle due to the damping processes.

$$Q = 2\pi \frac{Energy\ stored}{Energy\ dissipated\ per\ cycle} \qquad (1.14)$$

Quality factor can be extracted from the frequency response of a resonator (Figure 1.11b), as it is the ratio of resonance frequency to its $3dB$ bandwidth, expressed as:

$$Q = \frac{f_s}{\Delta f_{3dB}} \qquad (15)$$

Different damping mechanisms affecting the quality factor of a resonator have been reported in the literature, broadly characterized as a material-dependent and a design-dependent loss. Material loss includes energy loss in the piezoelectric material and resistive loss due to the metallic electrodes. Material losses are difficult to avoid but can be minimized by optimizing deposition conditions for piezoelectric material and using low resistive metals such as aluminium (Al) or molybdenum (Mo) for the electrodes. On the other hand, design-dependent loss mainly depends on the geometrical features of anchors, aperture, buses and finger-to-bus gaps that cause acoustic energy to radiate outwards from the tethered points of the resonator. Different anchor designs have been stated in literature to minimize the flow of outward energy or to create an acoustic mismatch at the end of the anchor in order to reflect the radiated energy back to the resonator [51][52]. Aperture length represents the active area of the resonator responsible for piezoelectric transduction. Longer aperture better confines the acoustic energy in the active region and reduces the effect of anchor design on Q [44]. Air damping also plays a significant role in lowering Q , as energy is lost due to friction with the surrounding medium when resonator is operated in air. Such loss can be minimized by operating the device at higher frequencies or by using hermetic seal packaging.

1.2.7 Technology evolution

Back in the 2000s, SAW resonators consisting of a single crystal bulk LN were the only well-established technology available to realize high frequency filters ($\approx$ 1 Ghz). At the same time, characterization of Lamb wave modes in LN plate had been reported [53]. High acoustic velocity and thickness-dependent frequency of asymmetric modes in LN showed potential for achieving 4G and 5G compatible filters but only the lower frequency devices ($\approx$ 10MHz) were tested due to the limitation of technology to produce ultra-thin single crystal LN films (< 1 µm). In 2009, *Kadota et al* [54][55] proposed an alternative solution by depositing an ultra-thin LN layer using Chemical Vapour deposition (CVD) [56]. He achieved a 395nm thick c-oriented epitaxial LN thin film with full width half maximum (FWHM) of 0.2° in a rocking curve. He realized an A1 mode resonator in Z-cut LN plate at 4.5 GHz in order to address the need for high frequency tuneable filters for cognitive radio systems. The fabricated resonator showed moderate k_t^2 and Q of 18% and 170, respectively. However, Smart Cut™ technology invented by SOITEC and CEA-Leti to transfer single crystal ultra-thin films onto the carrier substrate paved the path for the development of high performance resonators employing single crystal piezoelectric materials, such as lithium niobate and lithium tantalate. For the first time in 2011, a team of researchers from CEA-Leti demonstrated the fabrication of a submicron thick single crystal LN based FBAR at 2.35 GHz using Smart Cut™ technology [57][58]. Since then, many researchers have used A1 mode to fabricate high frequency resonators with a significantly improved performance due to the availability of ultra-thin LN films ($\approx$ 250 nm). Recently, two different groups led by Dr. Plessky and Dr. Gong have reported ladder-type filters for fifth generation (5G) of mobile networks using A1 mode in Z-cut LN plate [22][59]. Both have achieved resonators with almost similar performance, yielding k_t^2 and Q of $\approx$ 28% and $\approx$ 400, respectively. *Plessky et al*, also reported FBAR type resonators using shear waves in rotated Y-cut LN at 4 GHz with the large k_t^2 of 60% for 5G filters [60]. Gong has also reported A1 mode resonator in Y-cut LN plate at 1.65 GHz with k_t^2 and Q of 14% and 3112, respectively, making it a potential candidate for LTE mobile filters [61][62].

Unlike asymmetric mode resonator which is famous for its scalability to high frequency [63], shear horizontal mode resonator drives its popularity by having the highest electromechanical coupling among all the other acoustic modes. *Kadota et al* [64][65] utilized a large k_t^2 of SH0 mode to achieve ultra-wideband filters for cognitive radios. He demonstrated SH0 mode resonators with 55% coupling at 500 MHz yielding filters with 41% fractional bandwidth at 6 dB attenuation. On the other hand, the resonators showed moderate quality factor with in-band spurious modes. Spurious modes introduce ripples in the passband and degrade the out-of-band rejection of the filter. The presence of spurious modes close to

the resonance mode severely degrades the performance of the filters, obstructing their deployment as commercial solutions for future radio systems. Despite the potential of SH0 mode resonators, the bottleneck remains in eradicating or suppressing the spurious modes. *Gong et al* [51] demonstrated the suppression of higher order transverse modes close to the resonance mode by modifying the acoustic boundary conditions in the transverse direction. He modified the straight top and bottom edges (anchors) of the resonator into arched or triangular shaped edges, thus dispersing the energy from the higher order transverse modes. The devices with arched shaped edges effectively suppressed transverse modes and improved Q of a factor $x2.6$ for the SH0 mode. In another study, *Gong et al* [66][67] presented a ''length controlled'' electrode configuration to subdue transverse modes by optimizing the overlapping length of adjacent electrodes (aperture). It was shown that the smaller aperture effectively modified the stress profile in the resonator cavity thus diminishing the coupling of transverse modes nearly to zero. The optimized aperture resonators showed spurious free response with twice the Q for SH0 mode than the conventional resonators. He also demonstrated that an array of single electrode pair resonators connected in parallel effectively subdue spurious modes and improve Q of a factor $x2$, as compared the multi electrode pair equivalent resonator [39][68].

S0 mode combines the advantages of above-mentioned SH0 and A1 modes due to its unique characteristics of high acoustic velocity, low dispersion and pitch-dependent operating frequency. The early work on S0 mode was demonstrated in 2012 by *Wang et al* in Y-cut [69] and *Gong et al* [70][71] in X-cut LN thin films. Wang reported S0 mode resonators in Y136 LN film operating at 463 MHz and 750 MHz. k_t^2 and Q of the 463MHz resonator were 7% and 1500, respectively, whereas the resonator at 750MHz showed k_t^2 of 8.6% and Q of 612. Gong studied various in-plane device orientations (0° to 180°) for different rotated LN cuts (X, Y and Z) and identified the X-cut with the in-plane orientation of 30° as the best choice for maximizing k_t^2 for S0 mode. The reported k_t^2 and Q were 11% and 352, respectively. Early works showed devices with excessive spurious in the electrical response and a significantly low k_t^2 than the analytical models. In another study, *Gong et al* [48][72] presented k_t^2 enhancement techniques using a weighted electrode configuration that gradually reduced the width of the electrode fingers towards the free edges of the device. He demonstrated $2x$ improvement in k_t^2 and $3x$ improvement in Q than before as the resonators showed k_t^2 of 21.7% and Q of 1300. Furthermore, *Pop et al* [73] improved k_t^2 to 30% by using half width fingers at the free edges of the resonator to behave as λ/4 reflectors. In another work [46], he studied the dependence of different geometrical parameters such as anchor length and width, gap and bus width on Q. The experimental data showed that thinner anchors and a larger gap

helped to achieve a higher Q whereas bus width did not show significant effect on Q. The best device showed a FoM of 360, with measured electrical Q = 1200 and k_t^2 = 30% at 395 MHz. In recent study, *Colombo et al* [44][74] studied different ambiance and temperature dependent loss mechanisms affecting Q of the resonator. Experimental results showed 25% improvement in Q under vacuum than in air suggesting loss due to air damping. Furthermore, Q improved by a factor $2x$ at cryogenic temperature as compared to Q at room temperature, which confirmed the impact of electrical loading due to electrodes and pads. The devices showed ultra-high FoM of 1600 with k_t^2 of 30% and Q of 5326 under vacuum. It is important to note that the fabricated devices were very long (≈1mm) and operating at a much lower frequency (50 MHz) than the one presented above, yielding a higher Q.

1.3   Thesis outline

This thesis is organised into three chapters that encompass the development of LN based Lamb wave resonators and their system-level implementation in MEMS oscillators, followed by conclusions drawn from this work and possible future improvements.

Chapter 2 deals with the design, fabrication and characterization of S0, SH0 and A1 mode resonators on thin film LN. It consists of three manuscripts along with the supplementary information sections. The first manuscript (section 2.1.1) describes the process flow developed for the fabrication of S0 and SH0 mode resonators operating at around 500 and 300 MHz, respectively. It also investigates the effect of electrodes' material and coverage (duty factor) on k_t^2 and Q of the resonators. The second manuscript (section 2.2.1) demonstrates the improved version of the previously developed fabrication process flow by allowing complete control on the shape and size of the undercut (released area) around resonator. It also reports the effect of different inactive region elements such as undercut, anchor, bus and gap on Q of the resonator. The third manuscript (section 2.3.1) mainly deals with the fabrication of A1 mode resonators operating around 5 GHz, explicitly designed to fulfill the requirements of 5G filters.

Chapter 3 presents the development of an RF-MEMS oscillator using a SH0 mode resonator operating at 300 MHz. Barkhausen criteria for the oscillations are met by using an amplifier, phase shift, coupler and attenuator in a closed feedback loop along with the 2-port resonator acting as a frequency determining element. The oscillator's performance is judged against its frequency stability, and the influence of kt2 and Q of the resonators on PN of the oscillator is also demonstrated.

Chapter 4 concludes the outcomes of this research work and enlists some future research directions.

1.4 References

[1]   R. Ruby, "A snapshot in time: The future in filters for cell phones," *IEEE Microw. Mag.*, vol. 16, no. 7, pp. 46–59, Aug. 2015.

[2]   Cisco, "Global - 2020 Forecast Highlights," 2015.

[3]   Ericsson, "Mobile network traffic Q1 2020 – Mobility Report," 2020. [Online]. Available: https://www.ericsson.com/en/mobility-report/reports/june-2020/mobile-traffic-q1. [Accessed: 30-Nov-2020].

[4]   Yole, "5G impact on RF Front End Modules & Connectivity for Cellphones," 2018.

[5]   Yole, "STATUS OF THE MEMS INDUSTRY 2018- Market & Technology report," 2018.

[6]   J. Iannacci, "Introduction to MEMS and RF-MEMS: From the early days of microsystems to modern RF-MEMS passives," in *RF-MEMS Technology for High-Performance Passives. The challenge of 5G mobile applications*, IOP Publishing, 2017, pp. 1–39.

[7]   S. Syed, V. T. Challa, Y. Maddi, and H. K. Kakarla, "Iot based mems crash sensor for airbag system," in *Advances in Cybernetics, Cognition, and Machine Learning for Communication Technologies*, vol. 643, Springer, 2020, pp. 401–413.

[8]   G. Shi, C. S. Chan, G. Zhang, W. J. Li, P. H. W. Leong, and K. S. Leung, "Towards a mobile airbag system using MEMS sensors and embedded intelligence," in *2007 IEEE International Conference on Robotics and Biomimetics, ROBIO*, 2007, pp. 634–639.

[9]   P. Song *et al.*, "Recent progress of miniature MEMS pressure sensors," *Micromachines*, vol. 11, no. 1, 2020.

[10]   Z. Guo, R. Xu, L. Geng, and B. Li, "High-Voltage Driver for Fully-Integrated Piezoelectric Inkjet Printhead Module," in *17th IEEE International Conference on IC Design and Technology, ICICDT 2019 - Proceedings*, 2019.

[11]   J. Jain and M. R. Tripathy, "Study of MEMS technology and development of condenser microphone," in *Proceedings of the 5th International Conference on Confluence 2014: The Next*

Generation Information Technology Summit, 2014, pp. 880–882.

[12] O. Solgaard, A. A. Godil, R. T. Howe, L. P. Lee, Y. A. Peter, and H. Zappe, "Optical MEMS: From micromirrors to complex systems," *J. Microelectromechanical Syst.*, vol. 23, no. 3, pp. 517–538, 2014.

[13] H. C. Kim and K. Chun, "RF MEMS technology," *IEEJ Trans. Electr. Electron. Eng.*, vol. 2, no. 3, pp. 249–261, May 2007.

[14] J. J. Yao, "RF MEMS from a device perspective," *J. Micromech. Microeng*, vol. 10, 2000.

[15] R. Aigner, "SAW and BAW technologies for RF filter applications: A review of the relative strengths and weaknesses," in *2008 IEEE Ultrasonics Symposium*, 2008, pp. 582–589.

[16] C. T. C. Nguyen, "MEMS technology for timing and frequency control," *IEEE Transactions on Ultrasonics, Ferroelectrics, and Frequency Control*, vol. 54, no. 2. Institute of Electrical and Electronics Engineers Inc., pp. 251–270, 01-Feb-2007.

[17] S. Sabbagh and K. Mafinezhad, "4-6.3 GHz microwave tunable filter employing RF MEMS switches," in *2012 6th International Symposium on Telecommunications, IST 2012*, 2012, pp. 37–41.

[18] A. Kourani and S. Gong, "A Tunable Low-Power Oscillator Based on High-Q Lithium Niobate MEMS Resonators and 65-nm CMOS," in *IEEE Transactions on Microwave Theory and Techniques*, 2018, vol. 66, no. 12, pp. 5708–5723.

[19] A. Reinhardt, E. Defay, F. Perruchot, and C. Billard, "Tunable composite piezoelectric resonators: A possible Holy Grail of RF filters?," in *IEEE MTT-S International Microwave Symposium Digest*, 2012.

[20] C. Nguyen, "Vibrating RF MEMS overview: applications to wireless communications," in *Proceedings of SPIE: Micromachining and Microfabrication Process Technologyand Microfabrication Process Technology*, 2005, vol. 5715, pp. 11–25.

[21] J. Iannacci, "Expectations versus actual market of RF-MEMS: Analysis and explanation of a repeatedly fluctuating scenario," in *RF-MEMS Technology for High-Performance Passives. *, IOP Publishing.

[22] V. Plessky, S. Yandrapalli, P. J. Turner, L. G. Villanueva, J. Koskela, and R. B. Hammond, "5 GHz

laterally-excited bulk-wave resonators (XBARs) based on thin platelets of lithium niobate," *Electron. Lett.*, vol. 55, no. 2, pp. 98–100, Jan. 2019.

[23] A. Kourani, R. Lu, A. Gao, and S. Gong, "A 300-500 MHz Tunable Oscillator Exploiting Ten Overtones in Single Lithium Niobate Resonator," in *IFCS/EFTF 2019 - Joint Conference of the IEEE International Frequency Control Symposium and European Frequency and Time Forum, Proceedings*, 2019.

[24] A. Reinhardt, G. Parat, E. Defaÿ, M. Aïd, and F. Domingue, "Acoustic technologies for advanced RF architectures," in *Proceedings of the 8th IEEE International NEWCAS Conference, NEWCAS2010*, 2010, pp. 161–164.

[25] D. Li and M. Liu, "Improved electromigration reliability of surface acoustic wave devices using Ti/Al-Mo/Ti/Al-Mo electrodes," *Rare Met.*, vol. 28, no. 6, pp. 554–558, Dec. 2009.

[26] T. Shiba, O. Hikino, D. Okajima, and N. Kamogawa, "Study of Electrostatic Discharge Durability for Surface Acoustic Wave Module," *Jpn. J. Appl. Phys.*, vol. 44, p. 4523, 2005.

[27] T. Takai *et al.*, "I.H.P. SAW technology and its application to microacoustic components (Invited)," in *IEEE International Ultrasonics Symposium, IUS*, 2017.

[28] R. Ruby, "Review and comparison of bulk acoustic wave FBAR, SMR technology," in *Proceedings - IEEE Ultrasonics Symposium*, 2007, pp. 1029–1040.

[29] M. Kadota and S. Tanaka, "Solidly mounted resonator using shear horizontal mode plate wave in LiNbO3 plate," in *2016 IEEE International Frequency Control Symposium, IFCS 2016 - Proceedings*, 2016.

[30] M. Gorisse *et al.*, "High Frequency LiNbO3 Bulk Wave Resonator," in *IFCS/EFTF 2019 - Joint Conference of the IEEE International Frequency Control Symposium and European Frequency and Time Forum, Proceedings*, 2019.

[31] A. Reinhardt *et al.*, "Multiple frequency Solidly Mounted BAW filters," in *Proceedings of the IEEE International Frequency Control Symposium and Exposition*, 2011.

[32] R. Aigner, "MEMS in RF-filter applications: Thin film bulk-acoustic-wave technology," in *Solid State Sensors and Actuators (TRANSDUCERS)*, 2005, vol. 1, pp. 5–8.

[33] Qorvo, "A New Generation of 5G Filter Technology," *Qorvo*, no. January, pp. 1–6, 2020.

[34] S. Gong, "Lithium Niobate for M/NEMS Resonators," in *Piezoelectric MEMS Resonators*, H. Bhugra and G. Piazza, Eds. Springer International Publishing Switzerland 2017, 2017, pp. 99–129.

[35] V. Yantchev and I. Katardjiev, "Thin film Lamb wave resonators in frequency control and sensing applications: A review," *J. Micromechanics Microengineering*, vol. 23, no. 4, 2013.

[36] R. S. Weis and T. K. Gaylord, "Lithium Niobate: Summary of Physical Properties and Crystal Structure," *Appl. Phys. A 37*, pp. 191–203, 1985.

[37] B. A. Auld, "Elastic Properties of Solids," in *Acoustic fields and waves in solids*, John Wiley and sons, 1973, pp. 57–99.

[38] I. E. Kuznetsova, B. D. Zaitsev, S. G. Joshi, and I. A. Borodina, "Investigation of acoustic waves in thin plates of lithium niobate and lithium tantalate," *IEEE Trans. Ultrason. Ferroelectr. Freq. Control*, vol. 48, no. 1, pp. 322–328, Jan. 2001.

[39] Y.-H. Song and S. Gong, "Arraying SH0 Lithium Niobate laterally vibrating resonators for mitigation of higher order spurious modes," in *MEMS*, 2016, vol. 7, no. January, pp. 111–114.

[40] Y. Yang, R. Lu, T. Manzaneque, and S. Gong, "Toward Ka Band Acoustics: Lithium Niobate Asymmetrical Mode Piezoelectric MEMS Resonators," *IFCS 2018 - IEEE Int. Freq. Control Symp.*, pp. 1–5, 2018.

[41] M. Kadota, T. Ogami, K. Yamamoto, H. Tochishita, and Y. Negoro, "High-frequency lamb wave device composed of MEMS structure using LiNbO3 thin film and air gap," *IEEE Trans. Ultrason. Ferroelectr. Freq. Control*, vol. 57, no. 11, pp. 2564–2571, 2010.

[42] G. Piazza, P. J. Stephanou, and A. P. Pisano, "One and two port piezoelectric higher order contour-mode MEMS resonators for mechanical signal processing," *Solid. State. Electron.*, vol. 51, no. 11–12, pp. 1596–1608, 2007.

[43] J. Bjurstrom, L. Vestling, J. Olsson, and I. Katardjiev, "An accurate direct extraction technique for the MBVD resonator model," in *34th European Microwave Conference*, 2004.

[44] L. Colombo, A. Kochhar, G. Vidal-Alvarez, and G. Piazza, "X-Cut Lithium Niobate Laterally Vibrating MEMS Resonator with Figure of Merit of 1560," *J. Microelectromechanical Syst.*, vol. 27, no. 4, pp. 602–604, Aug. 2018.

[45] S. Yandrapalli, V. Plessky, J. Koskela, V. Yantchev, P. Turner, and L. G. Villanueva, "Analysis of

26

XBAR resonance and higher order spurious modes," in *2019 IEEE International Ultrasonics Symposium (IUS)*, 2019, pp. 185–188.

[46]   F. V. Pop, A. S. Kochhar, G. Vidal-Alvarez, and G. Piazza, "Investigation of Electromechanical Coupling and Quality Factor of X-Cut Lithium Niobate Laterally Vibrating Resonators Operating Around 400 MHz," *J. Microelectromechanical Syst.*, vol. 27, no. 3, pp. 407–413, 2018.

[47]   M. Faizan and L. G. Villanueva, "Frequency-scalable fabrication process flow for lithium niobate based Lamb wave resonators," *J. Micromechanics Microengineering*, vol. 30, no. 1, p. 15008, Jan. 2020.

[48]   S. Gong and G. Piazza, "Figure-of-merit enhancement for laterally vibrating lithium niobate mems resonators," *IEEE Trans. Electron Devices*, vol. 60, no. 11, pp. 3888–3894, 2013.

[49]   R. Lu, M. H. Li, Y. Yang, T. Manzaneque, and S. Gong, "Accurate extraction of large electromechanical coupling in piezoelectric MEMS resonators," *J. Microelectromechanical Syst.*, vol. 28, no. 2, pp. 209–218, 2019.

[50]   C. Cassella, Y. Hui, Z. Qian, G. Hummel, and M. Rinaldi, "Aluminum Nitride Cross-Sectional Lamé Mode Resonators," *J. Microelectromechanical Syst.*, vol. 25, no. 2, pp. 275–285, Apr. 2016.

[51]   Y. H. Song and S. Gong, "Elimination of spurious modes in SH0 Lithium Niobate laterally vibrating resonators," *IEEE Electron Devices Lett.*, vol. 36, no. 11, pp. 1198–1201, 2015.

[52]   A. Lozzi, A. De Pastina, E. Ting-Ta Yen, and L. Guillermo Villanueva, "Engineered acoustic mismatch for anchor loss control in contour mode resonators," *Appl. Phys. Lett*, vol. 114, p. 103502, 2019.

[53]   Y. Jin and S. G. Joshi, "Characteristics of Ultrasonic Lamb Waves in 128° Rotated Y-cut Lithium Niobate," *IEEE Trans. Ultrason. Ferroelectr. Freq. Control*, vol. 41, no. 2, pp. 279–283, 1994.

[54]   M. Kadota, T. Ogami, Y. Kansho, N. Yasuhiro, and T. Hikari, "High-Frequency Lamb Wave Device Composed of LiNbO3 Thin Film," *Japanese J. Appl. Phys. To*, vol. 48, pp. 7–08, 2009.

[55]   M. Kadota, T. Ogami, K. Yamamoto, H. Tochishita, and Y. Negoro, "High-frequency lamb wave device composed of MEMS structure using LiNbO3 thin film and air gap," *IEEE Trans. Ultrason. Ferroelectr. Freq. Control*, vol. 57, no. 11, pp. 2564–2571, Nov. 2010.

[56]   M. Kadota, Y. Suzuki, and Y. Ito, "FBAR using LiNbO3 thin film deposited by CVD," in *Proceedings -*

IEEE Ultrasonics Symposium, 2010, pp. 91–94.

[57] B. Imbert *et al.*, "LiNbO3 thin single crystal layer for RF applications," in *Proceedings of the IEEE International Frequency Control Symposium and Exposition*, 2011.

[58] A. Reinhardt *et al.*, "Acoustic filters based on thin single crystal LiNbO3 films: Status and prospects," in *IEEE International Ultrasonics Symposium, IUS*, 2014, pp. 773–781.

[59] Y. Yang, R. Lu, L. Gao, and S. Gong, "4.5 GHz Lithium Niobate MEMS Filters with 10% Fractional Bandwidth for 5G Front-Ends," *J. Microelectromechanical Syst.*, vol. 28, no. 4, pp. 575–577, Aug. 2019.

[60] V. P. Plessky, J. Koskela, and S. Yandrapalli, "Crystalline Y-cut Lithium Niobate Layers for the Bulk Acoustic Wave Resonator (YBAR)," in *2020 IEEE International Ultrasonics Symposium (IUS)*, 2020, pp. 1–4.

[61] Y. Yang, R. Lu, and S. Gong, "A 1.65 GHz Lithium Niobate A1 Resonator with Electromechanical Coupling of 14% and Q of 3112," in *Proceedings of the IEEE International Conference on Micro Electro Mechanical Systems (MEMS)*, 2019, vol. 2019–January, pp. 875–878.

[62] Y. Yang, R. Lu, T. Manzaneque, and S. Gong, "1.7 GHz Y-Cut Lithium Niobate MEMS Resonators with FoM of 336 and f.Q of 9.15×10^12," in *IEEE MTT-S International Microwave Symposium Digest*, 2018, vol. 2018–June, pp. 563–566.

[63] M. Kadota and T. Ogami, "5.4 GHz Lamb Wave Resonator on LiNbO3 Thin Crystal Plate and Its Application," *Japanese J. Appl. Phys. To*, vol. 50, pp. 7–11, 2011.

[64] M. Kadota and S. Tanaka, "Ultra-wideband ladder filter using SH0 plate wave in thin LiNbO3 plate and its application to tunable filter," *IEEE Trans. Ultrason. Ferroelectr. Freq. Control*, vol. 62, no. 5, pp. 939–946, 2015.

[65] M. Kadota, Y. Kuratani, T. Kimura, M. Esashi, and S. Tanaka, "Ultra-wideband and high frequency resonators using shear horizontal type plate wave in LiNbO3 thin plate," *Jpn. J. Appl. Phys.*, vol. 53, no. 7 SPEC. ISSUE, pp. 3–7, 2014.

[66] Y. H. Song and S. Gong, "Spurious mode suppression in SH0 Lithium Niobate laterally vibrating MEMS resonators," *Tech. Dig. - Int. Electron Devices Meet. IEDM*, vol. 2016–Febru, p. 18.5.1-18.5.4, 2015.

28

[67]   Y. H. Song, R. Lu, and S. Gong, "Analysis and removal of spurious response in SH0 lithium niobate MEMS resonators," *IEEE Trans. Electron Devices*, vol. 63, no. 5, pp. 2066–2073, 2016.

[68]   Y. Song and S. Gong, "Wideband Spurious-Free Lithium Niobate RF-MEMS Filters," *J. Microelectromechanical Syst.*, vol. 26, no. 4, pp. 820–828, 2017.

[69]   R. Wang, S. A. Bhave, and K. Bhattacharjee, "Thin-film Lithium Niobate Contour-mode Resonators," in *IEEE International Ultrasonics Symposium Proceedings*, 2012, pp. 3–6.

[70]   S. Gong and G. Piazza, "Laterally vibrating lithium niobate MEMS resonators with high electromechanical coupling and Quality factor," in *IEEE International Ultrasonics Symposium, IUS*, 2012, pp. 1051–1054.

[71]   S. Gong and G. Piazza, "Design and analysis of lithium-niobate-based high electromechanical coupling RF-MEMS resonators for wideband filtering," *IEEE Trans. Microw. Theory Tech.*, vol. 61, no. 1, pp. 403–414, 2013.

[72]   S. Gong and G. Piazza, "Weighted electrode configuration for electromechanical coupling enhancement in a new class of micromachined Lithium Niobate laterally vibrating resonators," *Tech. Dig. - Int. Electron Devices Meet. IEDM*, pp. 367–370, 2012.

[73]   F. V. Pop, A. S. Kochhar, G. Vidal-Álvarez, and G. Piazza, "Laterally vibrating lithium niobate MEMS resonators with 30% electromechanical coupling coefficient," in *Proceedings of the IEEE International Conference on Micro Electro Mechanical Systems (MEMS)*, 2017, pp. 966–969.

[74]   L. Colombo, A. Kochhar, G. Vidal-Álvarez, and G. Piazza, "Investigations on the Quality Factor of Lithium Niobate Laterally Vibrating Resonators with Figure of Merit Greater than 1,500," in *IEEE International Ultrasonics Symposium, IUS*, 2018, vol. 2018–Octob, pp. 2–5.

2 Development of Lithium Niobate Lamb Wave Resonators

Overall, this chapter is based on three manuscripts (two published and one under review) on the development and performance enhancement of lithium niobate resonators. Each manuscript is accompanied by a supplementary information section that discusses in detail different fabrication challenges and the solutions implemented to overcome those challenges for the successful development of lithium niobate resonators.

The first manuscript deals with the design, fabrication and characterization of lithium niobate based S0 and SH0 mode resonators. We demonstrate devices with the highest reported k_t^2 of 31% and 40% for S0 and SH0 modes with Q of 720 and 590, respectively, in X-cut LN. We also investigate the effect of electrodes' material and coverage (duty factor) on k_t^2 and Q of the resonators.

In the second manuscript, we develop a novel process flow for the fabrication of lithium niobate resonators that gives full control on the shape and size of the released region (undercut) near the anchors necessary for stabilizing Q across the wafer. We also study the impact of different inactive regions such as undercut, anchor, bus and gap on Q of the resonator. Through design optimization and improved process flow, we successfully manage to enhance Q from previously published Q of 590 to 1900 for SH0 mode resonator in X-cut LN.

The third manuscript deals with the fabrication of A1 mode resonators in Z-cut LN that addresses the need for high performance RF filters for 5G compatible handsets. Devices are fabricated with a yield of 70% and exhibit high k_t^2 and Q upto 28% and 300, respectively, for frequencies around 5 GHz.

2.1 Frequency-Scalable Fabrication Process Flow for Lithium Niobate Based Lamb Wave Resonators

2.1.1 Manuscript

Authors: Muhammad Faizan and Luis Guillermo Villanueva

Advanced NEMS Laboratory, EPFL, Lausanne, Switzerland

Authors' contribution: MF was responsible for the design, FEM simulations, fabrication and characterization of the devices. MF also made the figures and wrote the manuscript. LGV supervised the work.

Abstract

In this paper, we demonstrate the fabrication and characterization of lithium niobate (LN) based Lamb wave mode (S0 and SH0) resonators that address the stringent requirements of RF filtering for modern communication systems. The devices consist of a 400nm-thick X-cut LN membrane anchored from two ends with interdigitated transducer (IDT) on the top. We present a frequency-scalable process flow using e-beam lithography for the fabrication of ultra-high frequency (10^8 to 10^9 Hz) devices. Our fabricated devices yield the highest reported electromechanical coupling (k_t^2) of 31% and 40% for S0 and SH0 modes, respectively, in X-cut LN. We also investigate the influence of IDT material and coverage on k_t^2 and quality factor (Q) by fabricating identical devices with aluminum and platinum electrodes with electrode coverages ranging from 20 to 70%.

Introduction

For the next generation of communication systems, MEMS based RF-fronts involving MEMS switches, filters and oscillators are gathering much attention due to small form factor, low power consumption and CMOS compatibility [1][2]. Piezoelectric resonators, in particular Surface Acoustic Waves (SAW) and Bulk Acoustic Wave (BAW) resonators, are nowadays the leading technology for RF filters in mobile handsets and ultra-low power transceivers [3]. To achieve high performance wide band filters, MEMS resonators must feature a high electromechanical coupling (k_t^2) and quality factor (Q) which determine the fractional bandwidth, low insertion loss and high skirt steepness for RF filters [4]. Although SAW and BAW meet existing requirements for 4G, they are limited in terms of scalability and efficiency, in particular multiple frequencies per chips (in the case of BAW) and limited k_t^2 (in the case of SAW).

SAW resonators excite acoustic waves on the surface of piezoelectric (PZE) material using interdigitated transducers (IDT) where the resonance frequency and the behaviour of the acoustic waves into the bulk material are dependent on the separation between the IDT fingers. SAW devices allow to have multi-frequency filters on a single substrate but they have limited scalability to higher frequencies (>2GHz) [5]. Furthermore, SAW devices offer moderate k_t^2 and Q thus making them ineligible for wide band filters.

BAW resonators consist of PZE layer sandwiched between two metal layers that generate acoustic waves that remain in the vertical acoustic cavity. The resonance frequency is inversely proportional to the thickness of the PZE layer, which enables BAW devices to be easily scalable to high frequencies by depositing an ultra-thin PZE layer [6]. However, it is challenging to implement multiple frequencies on a single substrate, as it is limited by the thickness of PZE layer.

Addressing the requirements for wide band filters, lithium niobate (LN) based laterally vibrating resonators (LVR) enjoy the benefits of both the above-mentioned mature technologies [7]. IDT is used to transduce Lamb wave modes on a suspended thin film LN, so the frequency is lithographically controlled that allows to have multi-frequency resonators on the same substrate. Furthermore, LN based LVRs have been demonstrated with a very high figure of merit ($FoM = k_t^2 \cdot Q$) making them promising candidates for ultra-wide band filters [8].

In this paper, we present the fabrication and characterization of LN based LVR. E-beam lithography is chosen over optical lithography in order to have a frequency scalable process flow that allows the fabrication of devices with a wide frequency range from 10^8 to 10^9 Hz, especially for devices in GHz range

where the critical dimension falls below 300 nm. We also investigate the effect of electrode coverage (EC) and material on k_t^2 and Q by varying the EC from 20 to 70% for aluminum (Al) and platinum (Pt) electrodes.

$$EC\ (\%) = \frac{2 \times width\ of\ electrode}{\lambda} \times 100 \qquad (2.1)$$

Device Overview

Our device consists of a mechanically suspended LN membrane anchored from two ends with IDT on top as shown in Figure 2.1a. There is no metal under the LN membrane, rendering 1-port devices where the fingers of the IDT are alternatively connected to the signal and ground. When AC potential is applied to the fingers, the electric field generates lateral compressions and expansions in the LN that leads to the excitation of Lamb wave modes such as Symmetrical (S), Shear Horizontal (SH) and Asymmetrical (A) modes. The highly anisotropic nature of LN requires the selection of appropriate crystal cut and specific in-plane device orientation, in order to predominantly excite the required mode with large k_t^2 while suppressing all the other unwanted modes.

This work focuses on the study of two zeroth-order Symmetrical (S0) and Shear Horizontal (SH0) modes that yields the highest intrinsic coupling as compared to other acoustic modes, which is one of the requirements for a wide-band filter. According to [9], S0 and SH0 modes are predominantly excited in X-cut LN (i.e. LN cut with an Euler angle rotation of (90°, 90°, ɣ°) with in-plane device orientations of 30° and 170° from y-axis, respectively. The insets (ii) of Fig. 2.5 illustrate the X-cut LN wafer with the x-axis perpendicular to the yz planes. The devices are oriented in such a way that the direction of vibration of electrodes is along the required angle with respect to the primary flat (y-axis) of the wafer. The sound velocity and other material properties such as stiffness, piezoelectric and dielectric coefficients change with the direction and type of the acoustic wave [10].
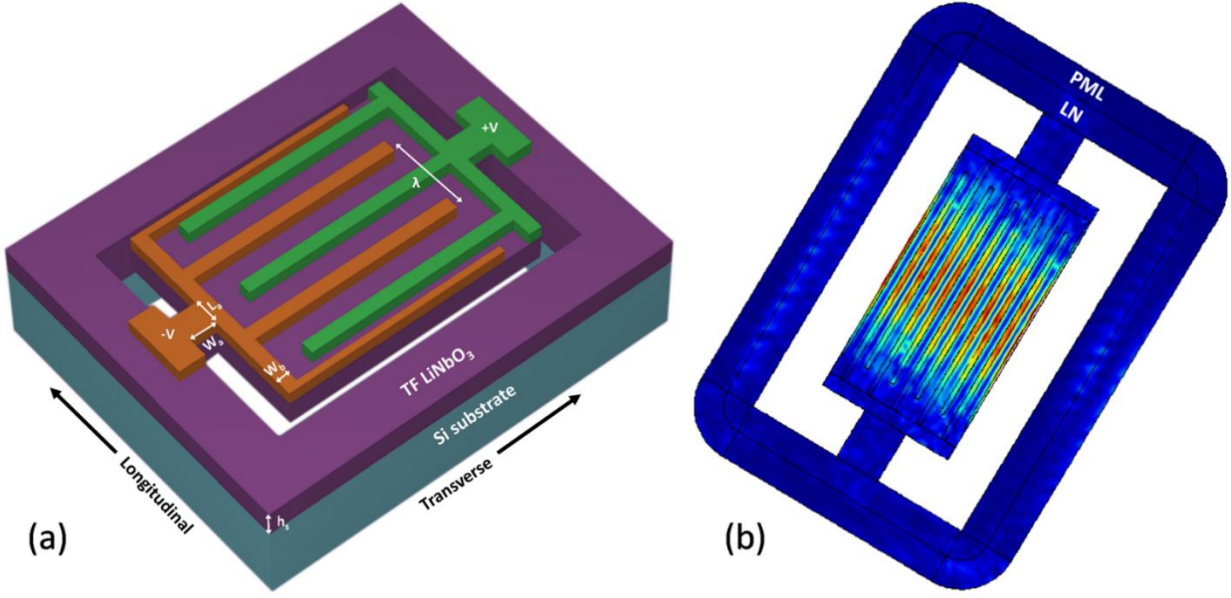
Parameter	Description	Value (µm)	Parameter	Description	Value (µm)
λ	wavelength	12	L_a	Anchor length	22.5
$L_{resonator}$	Resonator length	120	W_a	Anchor width	19.5
$W_{resonator}$	Resonator width	60	W_b	Bus width	6

Figure 2.1: (a) Design illustration of a Lamb wave resonator with IDT on top a suspended thin film LN. Fingers are located every $\lambda/2$, thus determining the resonance frequency of the device. (b) FEM simulation showing the stress distribution in 5-electrode pair model that represents the confinement of strain between the electrode fingers. Bottom - Table shows the geometrical parameters affecting the device performance. Mentioned values are used to model and fabricate resonators with electrode coverages from 20 to 70%.

The resonance frequency depends on the geometry of the device and the acoustic velocity (v) of the intended mode expressed as [11]:

$$f_{ij} = \frac{v}{2} \sqrt{\left(\frac{i}{W_p}\right)^2 + \left(\frac{j}{L_{res}}\right)^2} \qquad (2.2)$$

where f_{ij} is the resonance frequency of ith order longitudinal and j^{th} order transverse mode. W_p is the distance between the electrode fingers known as the pitch and L_{res} is the length of the resonator. For longitudinal modes, i and j are equal to 1 as the fundamental mode exists in lateral direction only and $L_{res} \gg W_p$, the resonance frequency for S0 and SH0 modes can be approximated as:

$$f \approx \frac{v}{2} \frac{1}{W_p} \tag{2.3}$$

The initial design of the device is taken from the literature that already has shown a very high performance [12] and FEM simulations are carried out in order to further optimize k_t^2 and minimize spurious in the admittance response of the device. Weighted electrode configuration is used where the electrodes at the free ends of resonator are designed to act as λ/4 reflectors to concentrate mechanical energy in the fundamental mode [13]. Figure 2.1b shows the stress distribution profile of the modeled design consisting of 5-electrode pairs on top of 400 nm X-cut LN membrane. The electric field and stress is mainly present in the regions between the electrode fingers for lateral (S0 and SH0) modes. The metal electrodes are 100 nm thick and 2 μm wide with a pitch of 6 μm. Figure 2.1 also shows the important parameters used to design the device.

Fabrication

We present the fabrication of LN based resonators with a device yield of 98%. Fabrication starts from a commercial substrate from NanoLN [14], consisting of a 3-inch Si carrier wafer, a 1 μm thick thermal SiO$_2$ buffer layer and a 400 nm-thick layer of X-cut LN on top. After placing accurate alignment marks, the wafer is diced into 13 x 10 mm^2 chips and the fabrication is done on chip level.

A systematic process flow is shown in Figure 2.2 that starts with the patterning of IDT on top of LN thin film using e-beam lithography. Two positive tone resists, PMMA and MMA, are used for the liftoff. MMA develops faster than PPMA and provides an undercut that is necessary for a better liftoff process.
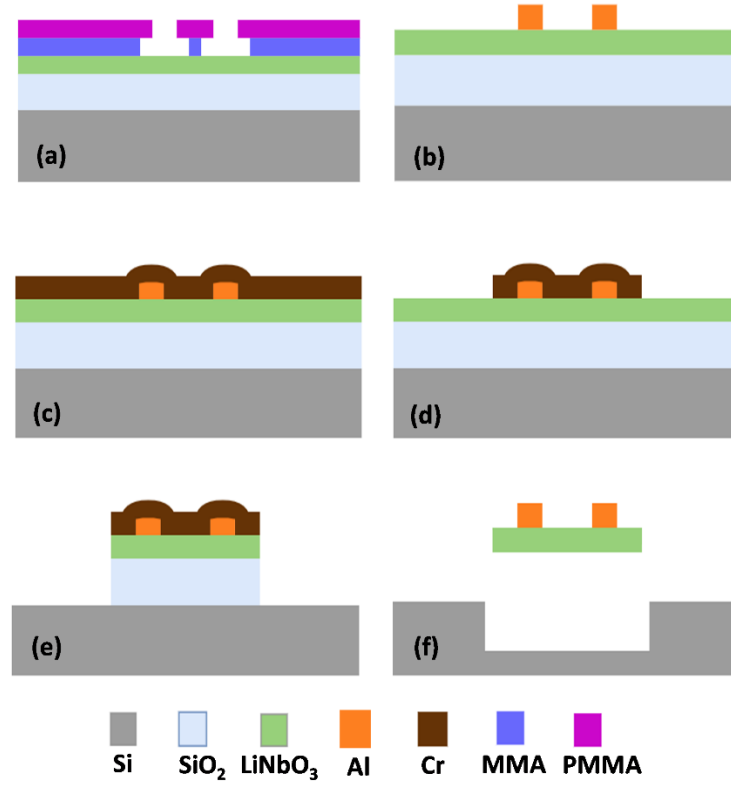
Figure 2.2: The fabrication process flow that involves patterning of narrow electrodes via E-beam lithography (a) followed by evaporation of metal for electrode liftoff (b). 150 nm thick chromium (Cr) is deposited as a hard mask for etching 400 nm thick LN (c). E-beam lithography is used to pattern hard mask and accurately align both the mask layers. Cr is etched in Ion Beam Etcher (IBE) (d) followed by etching of LN and SiO_2 in plasma etcher (SPTS) (e). Final step of the process flow consists of isotropic dry etching of Si in SPTS and wet etching of SiO_2 using BHF solution (f).

Electrical grounding of the chip during the E-beam writing phase is essential in order to avoid melting of resist due to high-energy electrons coming from the electron gun [15]. Charges are grounded by coating a 40nm thick layer of a conductive polymer (Electra 92 from ALLRESIST GmbH) on top of the resists while a copper tape is used to provide electrical connection between the holder and the top surface of the chip. Electra 92 is a hydro-soluble polymer that can easily be removed after exposure by washing the chip with water for 1 min. Subsequently, resists are developed for 1 min in MiBK:IPA 1:3 solution followed by rinsing with IPA. Metal is evaporated and liftoff is successfully finished by leaving the chip in acetone overnight. In this work, we have fabricated identical devices with two different materials for electrodes such as 100

nm-thick Al (Figure 2.3a) and 50 nm-thick Pt whereas 5 nm-thick Cr is used as an adhesive layer with both the metals.
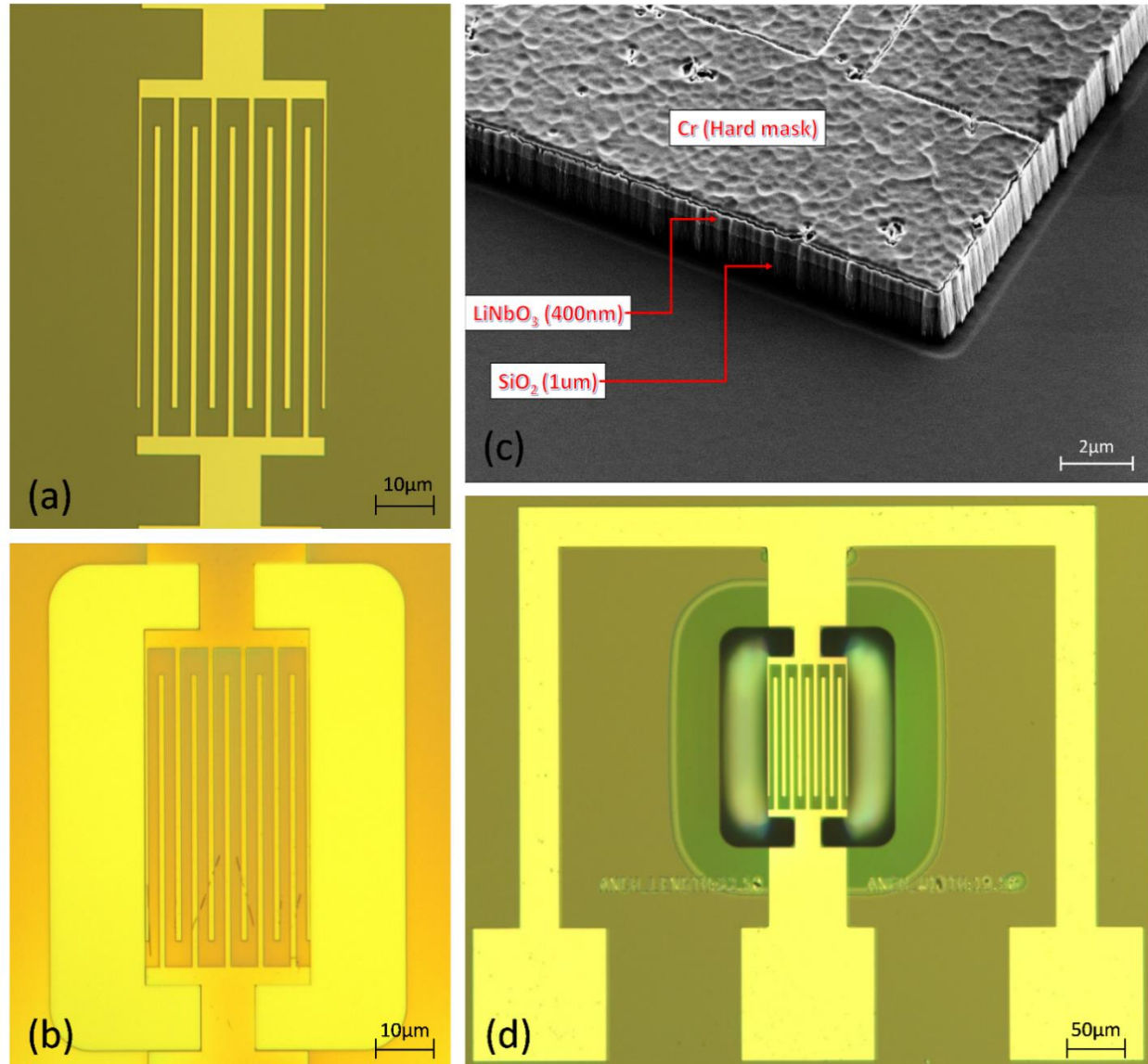
Figure 2.3: (a) Optical image of a 100nm thick Al based 5-pair electrode IDT after liftoff. (b) Optical image showing perfect alignment between the IDT and the second mask layer necessary for maximizing k_t^2. (c) SEM image showing the sidewall profile of the resonator after etching all the way down to the Si substrate. Obtained sidewall angle is close to 90°. (d) Optical image of a fully released 1-port device with EC of 35%.

The next step of the process flow involves the etching of LN in order to release the device, which we do using a hard mask. A 150 nm-thick layer of chromium (Cr) is evaporated to be used as a hard mask. Patterning of Cr is done via e-beam lithography. Automatic alignment of e-beam (VISTEC EBPG 5000) is used to accurately align the λ/4 reflectors to the edges of the resonator with an accuracy better than 50 nm (Figure 2.3b). A positive tone resist ZEP is spin coated at 1000 rpm to achieve the thickness of 225 nm and hard baked at 180 °C for 1 min. After exposure, ZEP is developed in amyl acetate for 1 min. Ion beam etching (VEECO IBE-350) is used to etch the Cr, which is later used to pattern LN by reactive ion etching (SPTS APS).

Fluorine chemistry is used to etch LN and the recipe is optimized in order to achieve vertical sidewalls without any re-deposition of etched material. The etching process involves a combination of physical and chemical etching by using Ar/CHF_3 (100/50 sccm) gases with 6mTorr pressure and 500W and 300W coil and platten powers respectively. Typical results can be seen in Figure 2.3c. A 1 µm-thick layer of SiO_2 is dry etched in SPTS by using C_4F_8/He (15/175 sccm) gases all the way down to the substrate.

The last step of the process flow involves the release of devices by first dry etching of Si in SPTS using SF_6 (300 sccm) gas to make a deep cavity below the devices followed by wet etching of buried SiO_2 using BHF solution. Figure 2.3d shows a fully released device with EC of 35% connected to Ground-Signal-Ground (GSG) pads.

Experimental Results

Fabricated devices are measured in 1-port configuration with a GSG probe connected to a RF network analyzer (HP8719). First, the measurement setup is calibrated with open, short and load standards in order to shift the measurements reference plane to the probe's tip plane. After calibration, scattering (S_{11}) parameters of the device under test (DUT) are extracted and converted to admittance (Y_{11}). Furthermore, the admittance response of the DUT is de-embedded by removing parasitic capacitance introduced by the pads [16]. The resultant admittance is fitted to a modified Butterworth–Van Dyke (mBVD) electrical model (Figure 2.4) for the extraction of k_t^2 and Q [17]. The important circuit parameters are expressed as:

- R_m, L_m and C_m represent the motional branch of the resonator responsible for inducing mechanical motion.

- R_o and C_o represent the dielectric loss and static capacitance in the resonator that are extracted by the real and imaginary part of the off-resonance admittance (background), respectively. In case of S0 and SH0 modes, the static capacitance of the resonator is expressed as [18]:

$$C_o = \frac{2\varepsilon_o \varepsilon_r L_e t}{\lambda(1 - EC)} \times (N_p + 1) \tag{2.4}$$

where $\varepsilon_0 \varepsilon_r$ is the LN permittivity, t is the thickness of the LN substrate, L_e is the effective length of electrode fingers , N_p is the number of electrode pairs and EC is the electrode coverage.

- C_p represents the parasitic capacitance introduced by the pads and is measured from a test structure without metalized fingers. Its admittance is subtracted from the admittance of the DUT for de-embedding [19].

- R_s represents the resistance of the pads and electrodes that is measured from the test structure having shorted fingers in order to extract unloaded (mechanical) quality factor. At this stage, we are not de-embedding R_s so the extracted Q is Q_L (loaded quality factor).

The commonly used formulas for calculating k_t^2 and Q are expressed as:

$$k_t^2 = \frac{\pi^2}{8} \frac{C_m}{C_o} \tag{2.5}$$

$$Q = \frac{f_s}{\Delta f_{3dB}} \tag{2.6}$$
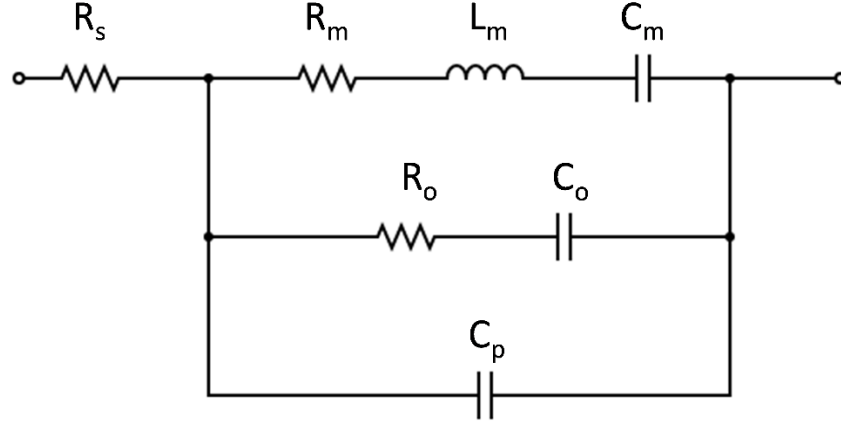
Figure 2.4: Equivalent circuit for mBVD model. R_m, L_m and C_m represents the motional parameters of the resonator whereas R_o and C_o represents the dielectric loss and static capacitance of the resonator respectively. Parasitic capacitance due to pads and overall electrical losses are represented by C_p and R_s respectively.

Single resonance mBVD fitting method is reliable for extracting circuit parameters in case of spurious-free or low coupling resonators where only the resonance (f_s) and anti-resonance (f_p) frequency peaks are fitted. For high coupling devices with spurious modes near the main mode, this technique does not yield accurate circuit parameters as it leads to incorrect extraction of C_o, resulting in an over or under estimation of k_t^2 depending on the position of spurious modes. For such devices, it is important to implement a multi-resonance recursive fitting technique that involves not only fitting f_s and f_p but also the spurious peaks present around them [20]. k_t^2 extracted from the recursive fitting technique closely resembles the k_t^2 calculated from $\pi^2/4 \cdot (1 - f_s/f_p)$.
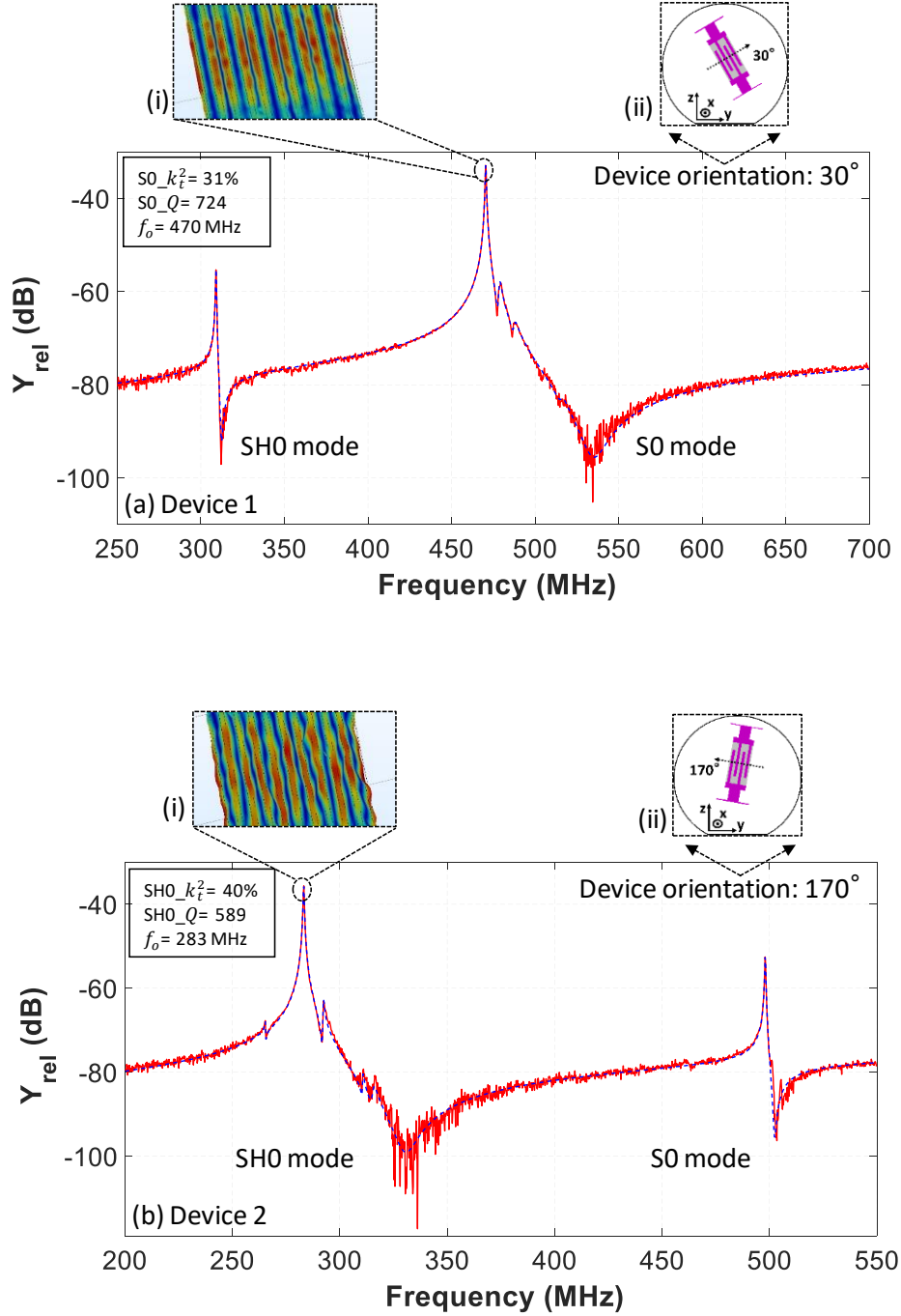
Figure 2.5: 1-port admittance response relative to 1S of two identical devices (EC 30%) with different in-plane orientations. (a) S0 mode is predominantly excited with the orientation of 30°, resulting in high k_t^2 and Q_L of 31% and 724, respectively. (b) Whereas 170° device orientation generates a large SH0 mode resulting in high k_t^2 and Q_L of 40% and 589, respectively. Insets (i) show the mode shapes of S0 and SH0 in 5-electrode pair resonator and insets (ii) illustrate the device orientation at specific angles with respect to wafer's flat (y-axis) in order to maximize k_t^2 for the intended mode.

Figure 2.5 shows the de-embedded admittance response of two identical devices (EC 30%) with different in-plane orientations. C_p of 25 fF is measured from an open test structure, which is later removed from the C_o of DUT. Device 1 and device 2 are oriented at 30° and 170°, respectively, with SH0 mode at ~300 MHz and S0 mode at ~500 MHz. S0 mode is predominantly excited in device 1 with a high k_t^2 of 31% and Q_L of 724 yielding FoM of 225 while SH0 mode shows low k_t^2 of 3.9%. By just changing the in-plane orientation, device 2 exhibits a high k_t^2 of 40% for SH0 mode and Q_L of 589 resulting in FoM of 236 while S0 mode shows low coupling ($k_t^2 \approx 1.8\%$). The insets (i) illustrate the shape of vibrating modes at resonance.

Effect of electrode coverage on k_t^2 and Q_L

We study the dependence of k_t^2 and Q_L on EC for different metals by fabricating identical devices on two separate chips, one with Al electrodes and the other with Pt electrodes. Each chip consists of two sets of devices with the same design parameters as listed in Fig. 1 and EC ranging from 20 to 70% in steps of 5%. The devices are oriented at 30° for S0 mode and k_t^2 and Q_L are extracted by the techniques mentioned above.

Figure 2.6a shows the relationship between the measured k_t^2 and EC for Al and Pt electrodes. Each data point is the average k_t^2 of two identical devices. For Al electrodes, k_t^2 remains at 30% with a standard deviation of 0.6% for EC from 20 to 40% and significantly goes down for higher electrode coverages. In the case of Pt electrodes, k_t^2 oscillates around 30% with a standard deviation of 1.4% for 20 to 40% EC and shows the same trend as of Al electrodes for higher electrode coverages. FEM simulations of devices identical to the ones measured experimentally confirm the same trend as shown by the measurements (Figure 2.6b). A 35% reduction in k_t^2 is observed when EC changes from 20% to 70%. The reason for this reduction in k_t^2 is mainly due to the non-linear increase in C_o (see Eq.4). The increase in EC causes the reduction in the spacing between the adjacent electrodes. This leads to C_o growing as $(\frac{1}{1-EC})$. At the same time, C_m increases linearly with EC, due to a linear increase in the electrode area and with no apparent negative effect of the increase of metal mass. Interestingly, we observe that, contrary to what we have seen for S0 modes in AlN resonators with bottom floating electrode, the C_m takes a value different from zero when the electrode width approaches to zero. As a consequence, since $k_t^2 \propto \frac{C_m}{C_o}$, it is natural to observe a constant value for small EC and a reduction of k_t^2 at higher electrode coverages (>40%).

From these measurements, we can conclude that k_t^2 does not depend on the material of the electrodes but it is mainly affected by the EC. To maximize k_t^2, it is safe to choose any EC between 20% and 40% but for our devices, the highest k_t^2 of 31% is achieved for 30% EC with Al electrodes and a k_t^2 of 31.6% is realized for 40% EC with Pt electrodes.
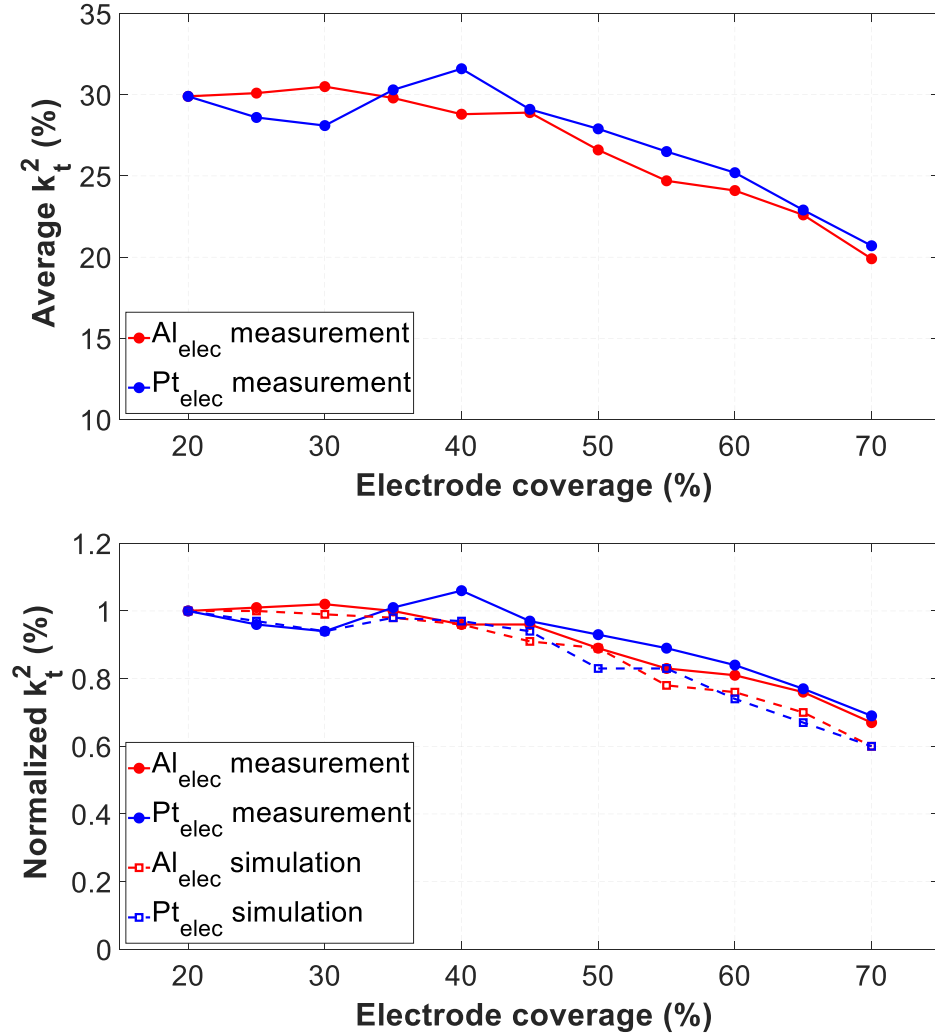
Figure 2.6: Effect of electrode coverages on k_t^2 for Al and Pt electrodes. (a) Measured k_t^2 shows a similar behavior for both Al and Pt electrodes where it almost remains constant up to 40% EC and then starts reducing for higher electrode coverages. Each data point is the average of two identical devices. (b) Simulated k_t^2 of the identical devices with different electrode coverages confirms the same down trend as seen by the measurements. k_t^2 is normalized by the highest value where it reduces by ~35% going from 20 to 70% EC.

Q_L of a Lamb wave resonator depends on many dissipation mechanisms such as acoustic losses due to anchors [21], material losses of PZE and metal electrodes, air damping and electrical loading due to electrodes' resistance [22]. Figure 2.7 shows the effect of EC on Q_L where Q_L almost remains the same from 30 to 60% EC for both Al and Pt electrodes. Whereas the devices with Al electrodes demonstrates $2 \times$ improvement in Q_L than Pt electrode devices. This shows that unlike k_t^2, Q_L is independent of EC and is mainly affected by the resistance of electrodes (R_s). We have also de-convoluted the effect of R_s from Q_L to yield unloaded quality factor (Q_{mech}). We report that Q_{mech} does not depend significantly neither on the EC nor on the thickness and type of electrode material. This is due to the strain confinement between the electrode fingers (Figure 2.1b). Average Q_{mech} for Al and Pt electrodes is 1100 ±250 and 900 ±250 respectively.
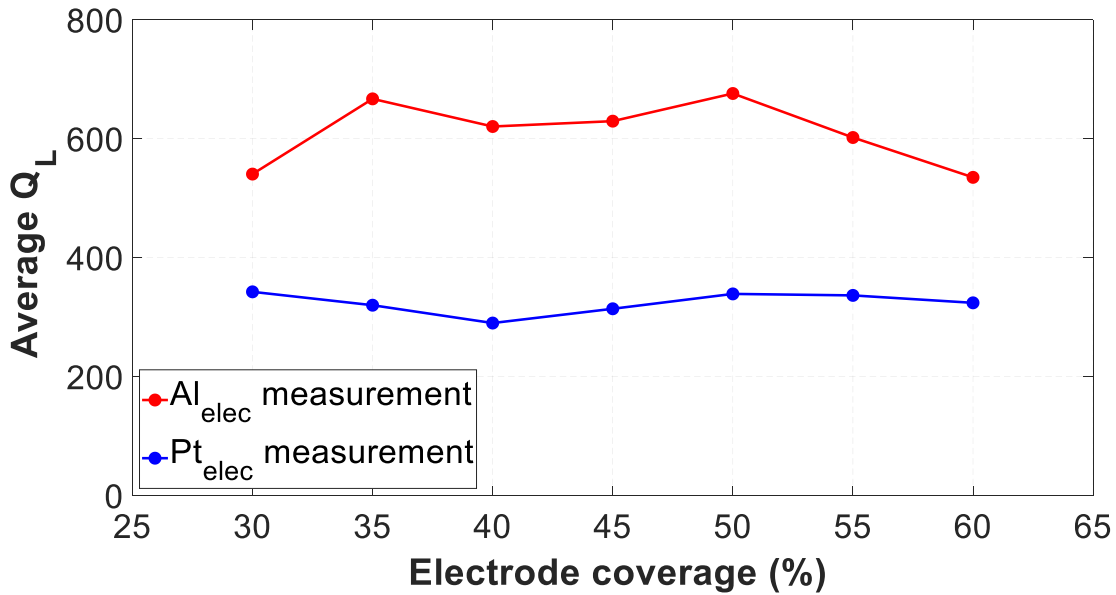
Figure 2.7: Effect of electrode coverages on Q_L for Al and Pt electrodes. Significant improvement in Q_L for Al electrodes can be seen compared to Pt electrodes, as Q_L is independent of EC and depends on resistance of the electrodes. Each data point is the average of two identical devices.

Conclusion

This work illustrates the fabrication and characterization of LN based Lamb wave resonators that are readily suitable to be used in RF filters for the next generation of communication systems. We have presented a frequency scalable process flow using E-beam lithography for the fabrication of ultra-high

frequency (10^8 to 10^9 Hz) devices. The fabricated devices consist of a 400 nm-thick suspended X-cut LN membrane with interdigitated metal electrodes on top. With the right in-plane orientation, the devices are excited with the highest reported k_t^2 of 31% and 40% for S0 and SH0 modes, respectively.

Our experimental results show that low electrode coverages (20 to 40%) do not have significant effect on k_t^2 but due to increasing fringing effect and mass loading k_t^2 reduces by ~35% for higher electrode coverages (>40%). We also conclude that the material of the IDT does not influence k_t^2 as a similar trend is observed from the devices with Al and Pt electrodes, whereas Q_L is affected by the IDT material losses as Q_L shows $2 \times$ improvement for devices with Al electrodes as compared to Pt electrodes.

References

[1] C. T.-C. Nguyen, "MEMS Technologies and Devices for Single-Chip RF Front-Ends," *J. Microelectron. Electron. Packag.*, vol. 3, no. 4, pp. 160–168, Oct. 2006.

[2] H. Okazaki, A. Fukuda, K. Kawai, T. Furuta, and S. Narahashi, "MEMS-based Reconfigurable RF Front-end Architecture for Future Band-free Mobile Terminals," in *2007 European Conference on Wireless Technologies*, 2007, pp. 300–303.

[3] R. Aigner, "SAW and BAW technologies for RF filter applications: A review of the relative strengths and weaknesses," in *2008 IEEE Ultrasonics Symposium*, 2008, pp. 582–589.

[4] G. Piazza, P. J. Stephanou, and A. P. Pisano, "Single-Chip Multiple-Frequency ALN MEMS Filters Based on Contour-Mode Piezoelectric Resonators," *J. Microelectromechanical Syst.*, vol. 16, no. 2, pp. 319–328, Apr. 2007.

[5] S. Härmä and V. P. Plessky, Surface Acoustic Wave RFID Tags, in Development and Implementation of RFID Technology, 2009. DOI: 10.5772/6522.

[6] C. C. W. Ruppel, "Acoustic Wave Filter Technology–A Review," *IEEE Trans. Ultrason. Ferroelectr. Freq. Control*, vol. 64, no. 9, pp. 1390–1400, Sep. 2017.

[7] S. Gong and G. Piazza, "Design and analysis of lithium-niobate-based high electromechanical coupling RF-MEMS resonators for wideband filtering," *IEEE Trans. Microw. Theory Tech.*, vol. 61, no. 1, pp. 403–414, 2013.

[8] F. V. Pop, A. S. Kochhar, G. Vidal-Alvarez, and G. Piazza, "Investigation of Electromechanical Coupling and Quality Factor of X-Cut Lithium Niobate Laterally Vibrating Resonators Operating Around 400 MHz," *J. Microelectromechanical Syst.*, vol. 27, no. 3, pp. 407–413, 2018.

[9] I. E. Kuznetsova, B. D. Zaitsev, S. G. Joshi, and I. A. Borodina, "Investigation of acoustic waves in thin plates of lithium niobate and lithium tantalate," *IEEE Trans. Ultrason. Ferroelectr. Freq. Control*, vol. 48, no. 1, pp. 322–328, Jan. 2001.

[10] K. Mizutaui and K. Toda, "Analysis of Lamb Wave Propagation Characteristics in Rotated," *Electron. Commun. Japan*, vol. 69, no. 4, 1986.

[11] Y. Song, and S. Gong, "Wideband Spurious-Free Lithium Niobate," *J. Microelectromechanical Syst.*, vol. 26, no. 4, pp. 820–828, 2017.

[12] F. V. Pop, A. S. Kochhar, G. Vidal-Álvarez, and G. Piazza, "Laterally vibrating lithium niobate MEMS resonators with 30% electromechanical coupling coefficient," *Proc. IEEE Int. Conf. Micro Electro Mech. Syst.*, pp. 966–969, 2017.

[13] S. Gong and G. Piazza, "Figure-of-merit enhancement for laterally vibrating lithium niobate mems resonators," *IEEE Trans. Electron Devices*, vol. 60, no. 11, pp. 3888–3894, 2013.

[14] NANOLN, "LN thin film on insulator." [Online]. Available: https://www.nanoln.com/PRODUCTS_128978.html.

[15] G. ALLRESIST GmbH – Strausberg, "Resist-Wiki: Conductive films." [Online]. Available: https://www.allresist.com/photorestist-other-resists-conductive-films/. [Accessed: 09-Aug-2019].

[16] M. C. A. M. Koolen, J. A. M. Geelen, and M. P. J. G. Versleijen, "An improved de-embedding technique for on-wafer high-frequency characterization," in *Proceedings of the 1991 Bipolar Circuits and Technology Meeting*, pp. 188–191.

[17] J. D. Larson, P. D. Bradley, S. Wartenberg, and R. C. Ruby, "Modified Butterworth-Van Dyke circuit for FBAR resonators and automated measurement system," in *2000 IEEE Ultrasonics Symposium. Proceedings. An International Symposium (Cat. No.00CH37121)*, vol. 1, pp. 863–868.

[18] L. Colombo, A. Kochhar, G. Vidal-Alvarez, and G. Piazza, "X-Cut Lithium Niobate Laterally Vibrating MEMS Resonator with Figure of Merit of 1560," *J. Microelectromechanical Syst.*, vol. 27, no. 4, pp. 602–604, Aug. 2018.

[19] A. Lozzi, A. De Pastina, L. G. Villanueva, and E. T.-T. Yen, "Release area confinement in Contour mode resonators," in *2017 IEEE International Ultrasonics Symposium (IUS)*, 2017, pp. 1–4.

[20] R. Lu, M. H. Li, Y. Yang, T. Manzaneque, and S. Gong, "Accurate extraction of large electromechanical coupling in piezoelectric MEMS resonators," *J. Microelectromechanical Syst.*, vol. 28, no. 2, pp. 209–218, 2019.

[21] A. Lozzi, A. De Pastina, E. T.-T. Yen and L. G. Villanueva, "Engineered acoustic mismatch for anchor loss control in contour mode resonators," *Appl. Phys. Lett.*, vol. 114, March 2019.

[22] G. Piazza, P. J. Stephanou, and A. P. Pisano, "Piezoelectric Aluminum Nitride Vibrating Contour-Mode MEMS Resonators," *J. Microelectromechanical Syst.*, vol. 15, no. 6, pp. 1406–1418, Dec. 2006.

2.1.2 Supplementary material

Fab issues

Fabrication of devices consisting of thin film lithium niobate is a challenging task especially when E-beam lithography is used as a writing tool. The path towards the successful fabrication of devices has always been paved by many unsuccessful attempts that require constant optimization of the steps involved in the process flow. The process flow mentioned in the publication 'Frequency-Scalable Fabrication Process Flow for Lithium Niobate based Lamb Wave Resonators' has been thoroughly optimized to be efficient and reproducible. This section highlights some of the fabrication challenges and the solutions implemented for the optimization of the process flow.

The first step of the process flow requires the writing of electrodes on LN using E-beam lithography. The melting of the resist due to the high-energy charges coming from the E-beam gun is a major problem (Figure 2.8) and requires a proper grounding of charges for achieving the required pattern. The second step of the process flow involves the etching of LN for the patterning of devices with the straight sidewall profile. It is observed that the improper conversion of layout layer in the E-beam software can cause ripples to appear on the sidewalls of the structures as shown in Figure 2.9. The third step of the process flow requires the release of the devices by either removing the sacrificial layer (SiO_2) or etching a deep cavity underneath the devices in the Si substrate. Figure 2.10 shows the release of test structures by just removing the sacrificial layer (SiO_2) using BHF solution and vapour HF etcher. Vapour HF is unable to completely etch PEVCD SiO_2 and leaves residues whereas BHF solution cause stiction upon release due to the bending in the suspending structures. However, Critical Point Drying (CPD) technique helps to avoid stiction for the smaller structures but fails to release the larger structures. The release of devices by etching a cavity in the substrate is essential for large devices that are bending down due to stress Figure 2.11 shows the collapse of the released devices from the corner point of the anchor due to the high stress. It is observed that introducing curvature at the sharp corners of the device helps improve the structural integrity and avoid breakage of the devices from the anchors. After device release, the final step is to remove buried SiO_2 while protecting Al electrodes. Etching SiO_2 with Al electrodes is a challenging task as both can be etched by the same chemistry. The electrodes need to be protected while HF or BHF solution is used to remove the buried SiO_2. Figure 2.12 shows the unwanted removal of Al electrode during SiO_2 removal step as the masking layer is not providing sufficient protection to the electrodes. However, the successful release of devices followed by removal of buried SiO_2 is achieved by using photoresist as a protecting layer for the Al electrodes as shown in Figure 2.13.

48
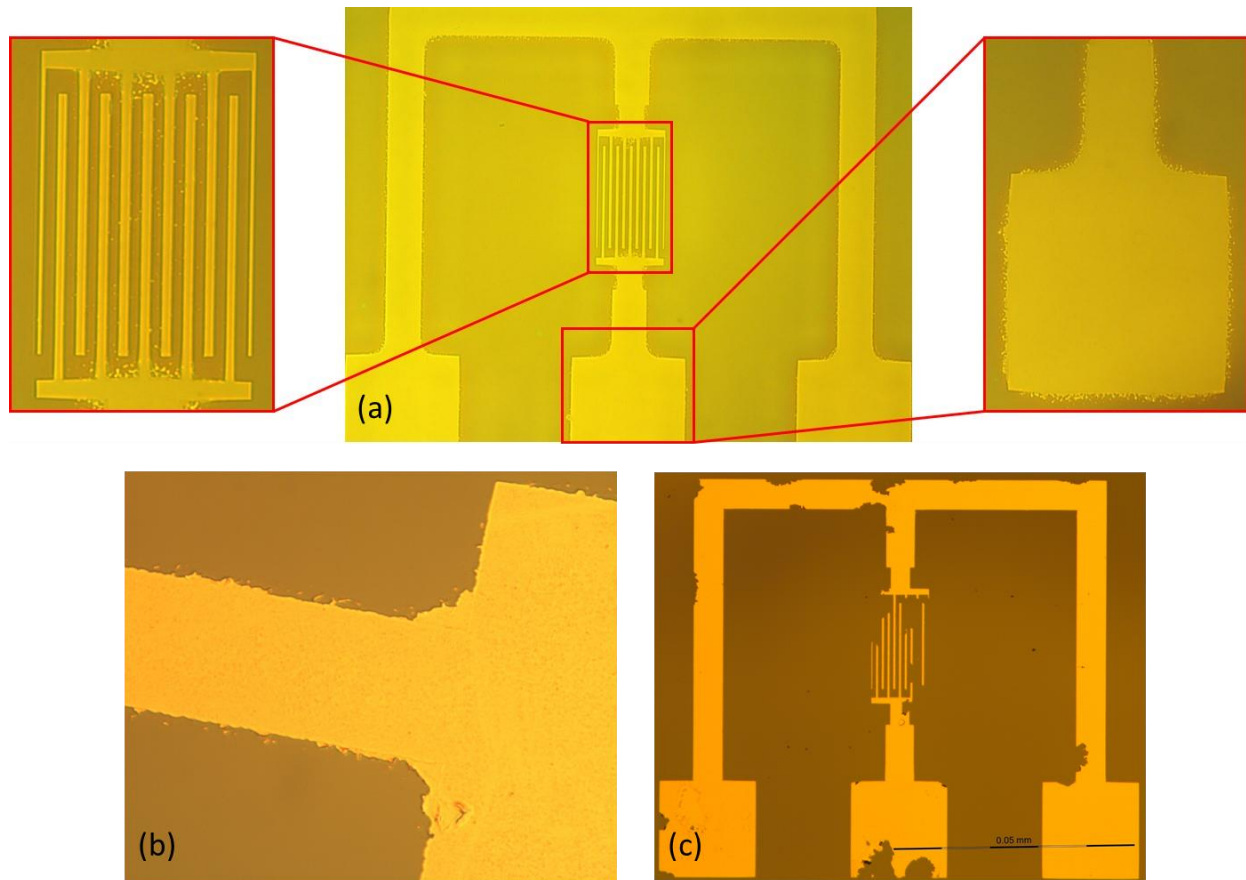
Figure 2.8: (a) Optical image after development phase shows the melting of resist due to the grounding effects of E-beam lithography. Grounding of the chip during the ebeam writing phase is essential to get the required patterns otherwise the resist can easily be melted due to the heat generated by the high-energy electrons. When Si is used as a substrate, some charges are grounded through the substrate while the rest can be neutralized by coating a thin layer of conductive polymer such as Electra 92 on top of the resists with the copper tape connecting to the ground. On the other hand, while doing E-beam lithography on a high insulating substrate such as bulk LN or glass, the grounding of charges through the substrate is impossible. In order to solve this problem, a thick layer of metal such as Cr or Al can be evaporated on top of the resists before ebeam exposure and the same metal layer is removed by wet etching after the exposure but before development of the resists. Copper tape is again used to provide the electrical connection for the grounding of metal layer. The energy of the electrons is enough to pass through the metal layer and expose the resist before being grounded. (b)-(c) Optical images of the unsuccessful liftoff due to the melted sidewalls of the patterns.
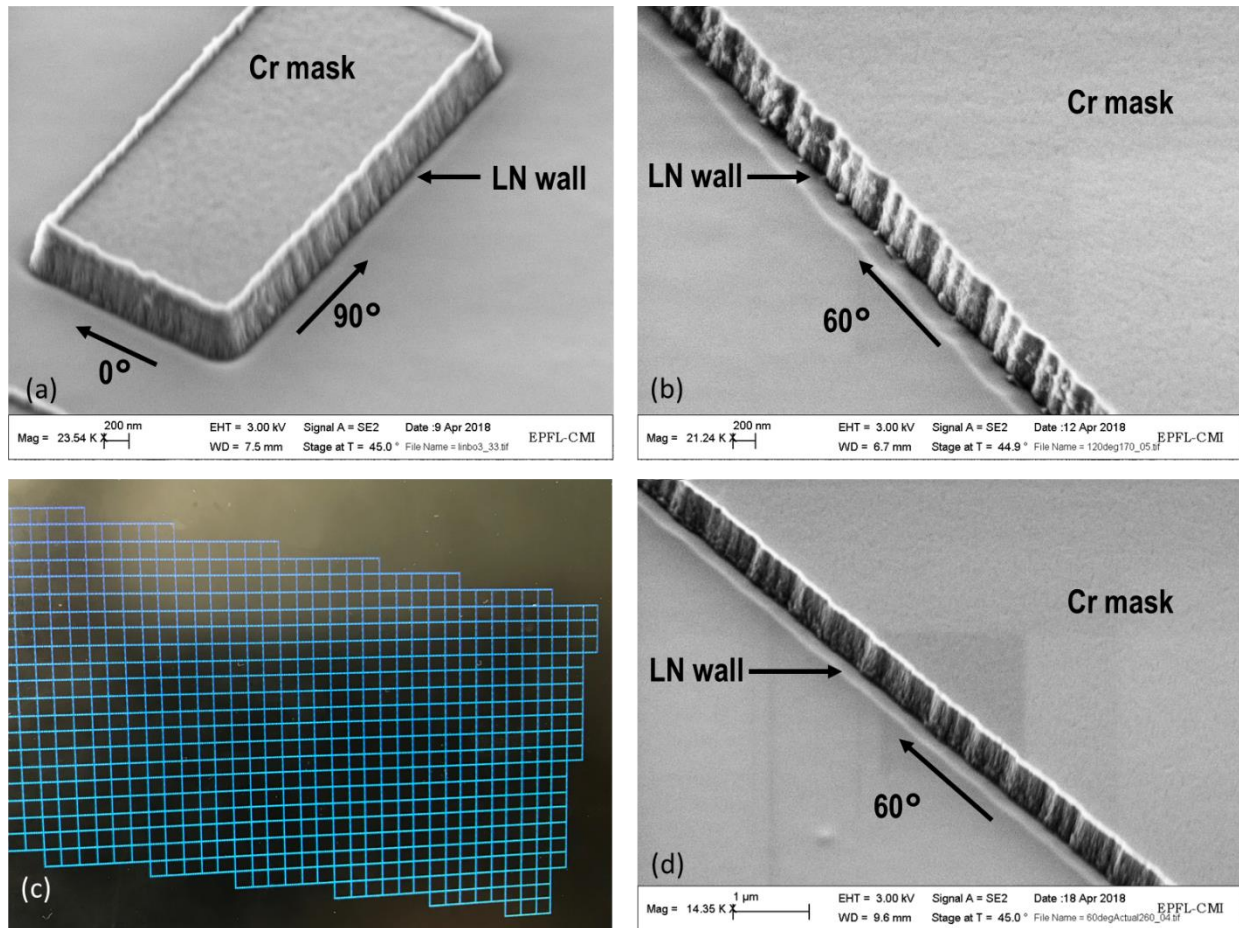
Figure 2.9: The performance of acoustic resonators is highly sensitive to the side wall profile of the devices. Straight side walls act as acoustic reflectors and help to confine the acoustic energy within the resonator cavity, whereas sloppy side walls excite different spurious modes and reduce the Q of the resonator. SEM images showing a side wall profile of LN, etched down using Cr as a hard mask in the Reactive Ion Etcher (RIE). The etching recipe developed at CMi using Ar/CHF$_3$ (100/50 sccm) gases with 6mTorr pressure and 500W and 300W coil and platten powers, respectively, is optimized in order to achieve the straight side walls of LN without redeposition of etched material. (a) SEM image showing a side wall profile of a test structure of LN with perfectly straight and clean side walls aligned at 0° and 90°. (b) SEM image showing ripples in the side wall of the LN structure aligned at 60° on the same substrate. Our experiments suggest that the difference in the side wall profile of structures aligned at different angles is not material or process dependent but is due to the way ebeam software fractures the mask layout. (c) The layout is converted into small square pixels where each pixel is exposed by the circular beam spot. The same sizes of pixel and spot lead to the ripples on features aligned at some angle. (d) SEM image showing ripple free side wall profile of a LN structure aligned at 60° after appropriate selection of ebeam pixel and spot sizes.
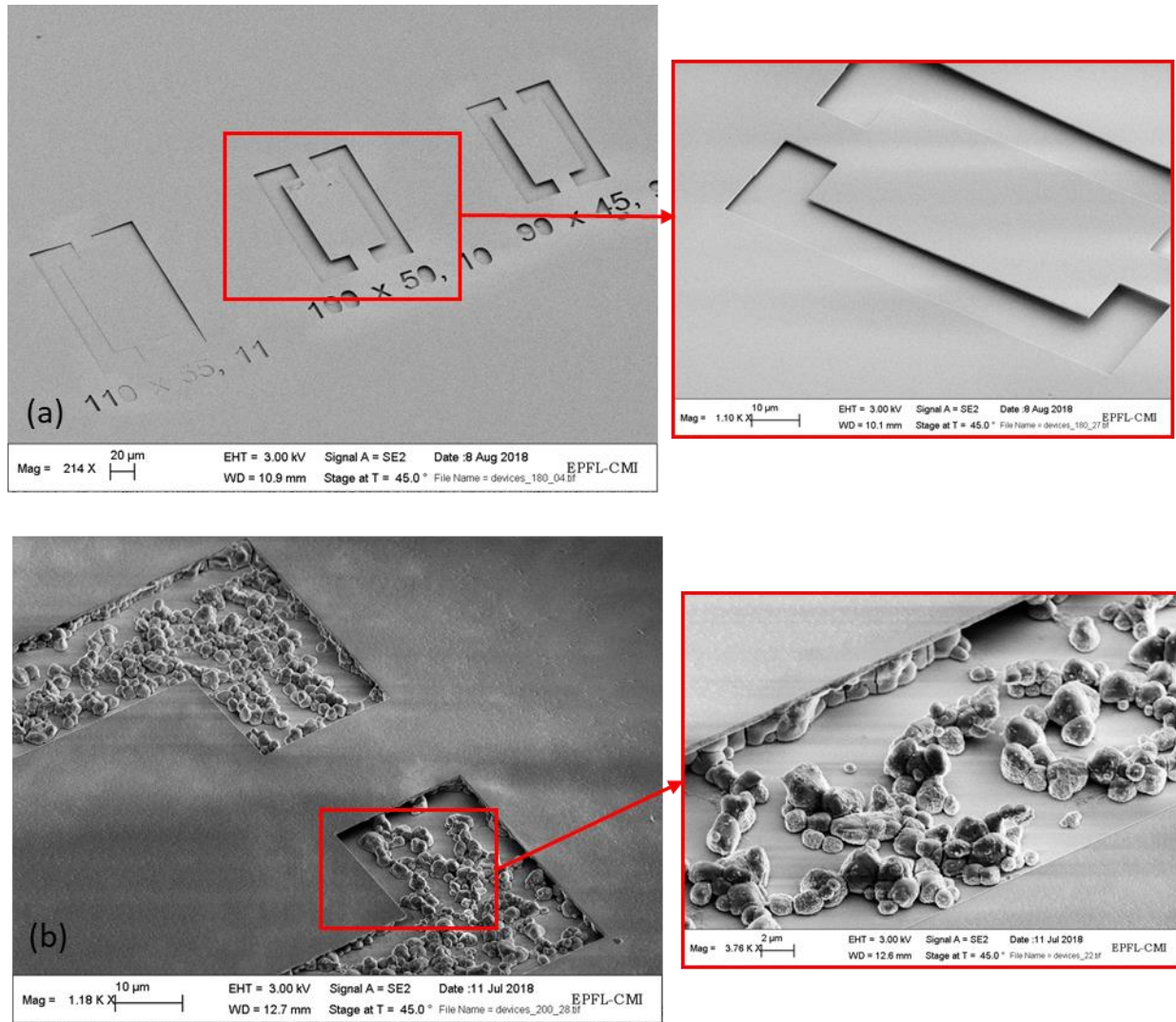
Figure 2.10: Device collapse on release due to stress or stiction is a very common phenomenon in microfabrication. (a) SEM image showing suspended test structure with one larger collapsed structure. The test structures are released by wet etching of SiO_2 in HF solution followed by rinsing in IPA solution. Critical Point Drying (CPD) is used to avoid stiction. After SiO_2 etching, the chip is carefully transferred into ethanol solution for CPD. It is important to note that during the transfer of the chip from one solution to another, the top surface of the chip must be submerged in liquid and should not be exposed to the air. The smaller structures are successfully suspended after CPD but larger structures collapsed due to bending. (b) SEM image of a test structure released with vapor HF machine to avoid stiction. Residues of SiO_2 are visible since the machine is unable to etch PECVD oxide.
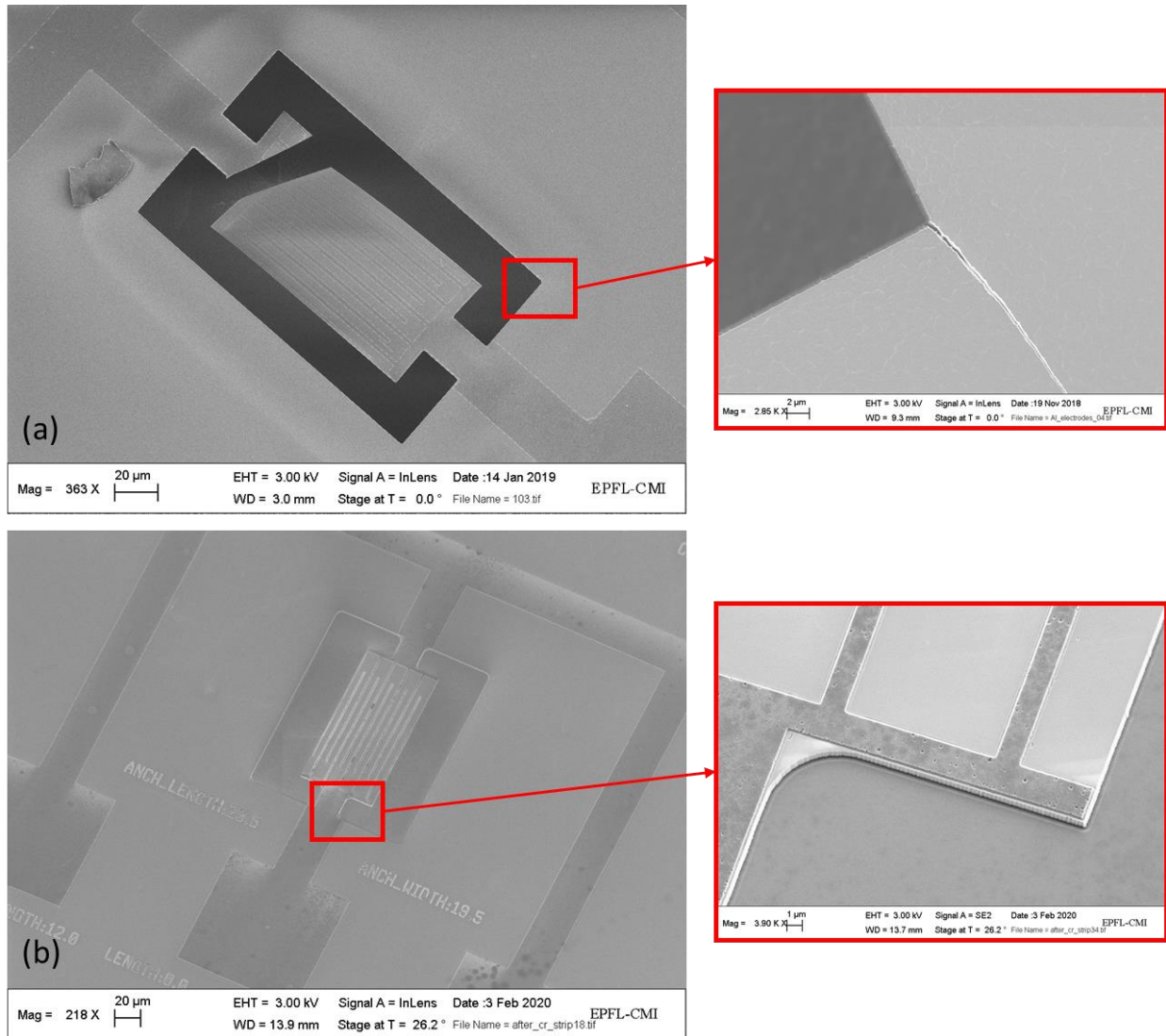
Figure 2.11: (a) SEM image showing the breakage of device from the corner of the anchor upon release due to high stress. Cracks appeared mostly at the concave shaped corners and resulted in device collapse. (b) SEM image showing the rounding of concave shaped anchors close to the anchor and around the release area. It is observed that by modifying the design of the corners and introducing a curvature bigger than 2 μm helps to reduce structural stress and achieve a successful release of the devices.
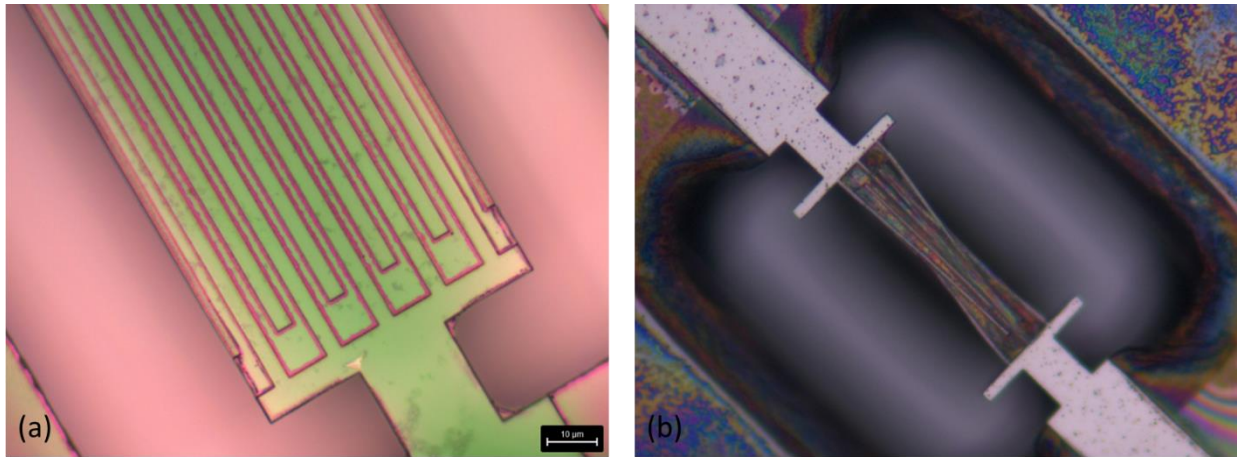
Figure 2.12: The last step of the process flow involves suspending the devices by etching a deep cavity underneath followed by removal of buried SiO_2 using BHF solution. The electrodes need to be covered by a mask layer in order to protect the Al electrodes from being etched away by BHF solution. (a) Optical image showing the unwanted removal of Al electrodes during the SiO_2 removal phase due to the insufficient protection provided by Cr as a masking layer. (b) Vapor HF etching to remove SiO_2 while providing selectivity to Al is a well know technique. However, long exposure to vapor HF etching affects the surface of LN and results in damaging of the device.
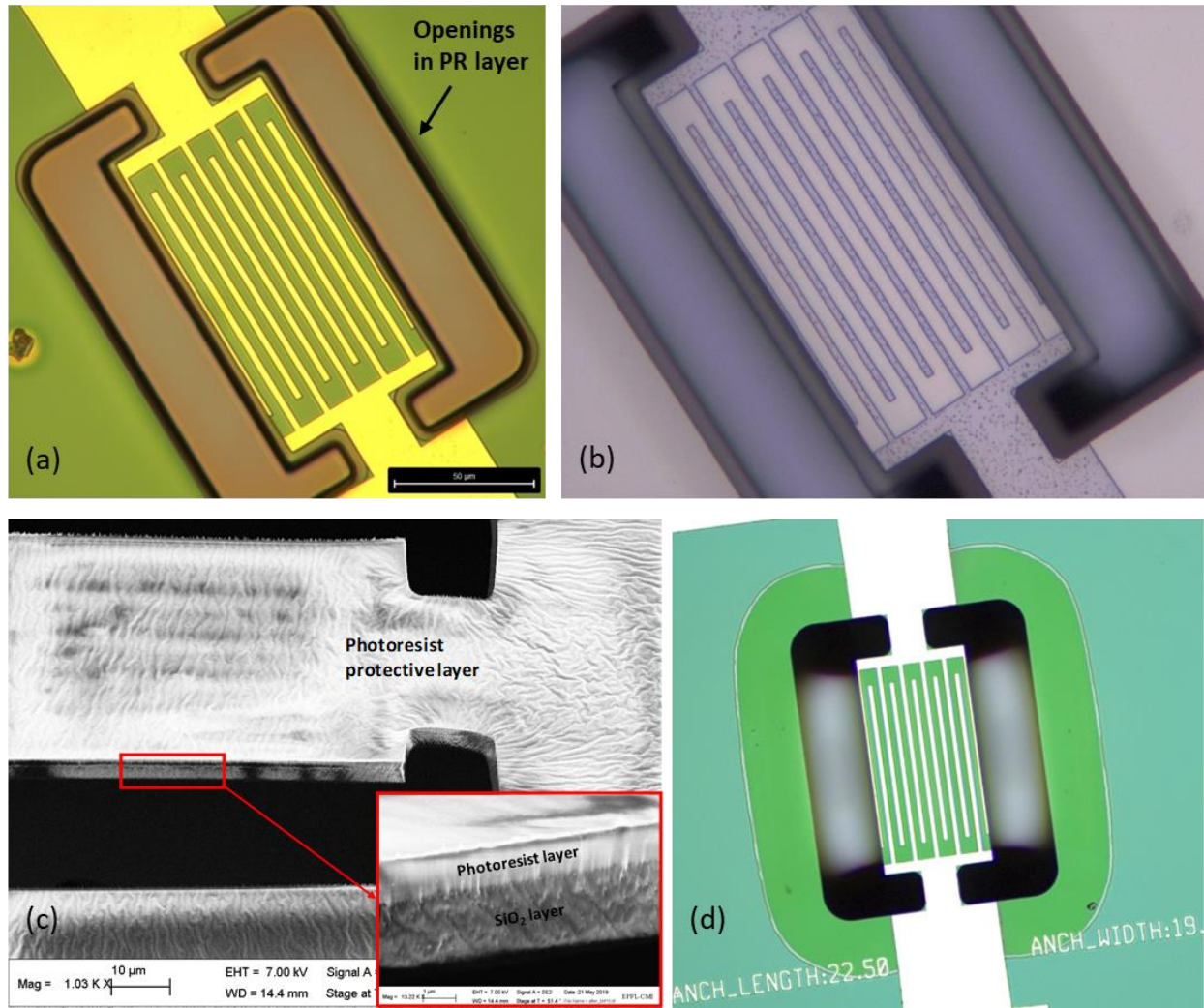
Figure 2.13: (a) Optical image showing the patterning of photoresist (PR) with the openings at the resonator release area while completely covering the electrodes. Cr as a hard mask is used to pattern LN followed by a 5 μm layer of photoresist for the etching of SiO_2 and Si cavity underneath. (b) Optical image showing the suspended resonator after all the dry etchings and with buried SiO_2. (c) SEM image of the resonator completely covered with photoresist layer even after all the dry etchings. The advantage of using photoresist as a protective layer is to remove buried SiO_2 via BHF solution while photoresist protecting Al electrodes from being etched away by BHF solution. (d) Optical image of the successful release of the devices after the removal of buried SiO_2 followed by stripping of photoresist layer.

54

Effect of electrode coverage on k_t^2

A significant reduction in k_t^2 is observed when EC changes from 20% to 70%. This is mainly due to the non-linear increase in C_o as it grows with the factor of ($\frac{1}{1-EC}$) whereas C_m increases linearly with EC, due to a linear increase in the electrode area.
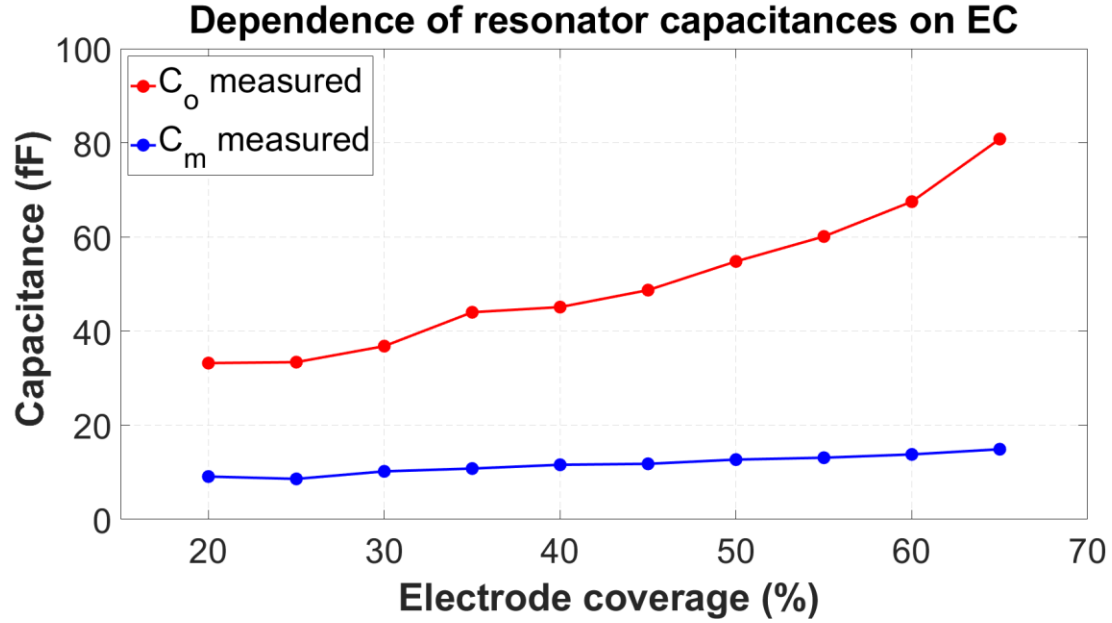
Figure 2.14: Dependence of motional and static capacitances on electrode coverages of the IDT. A significant reduction in k_t^2 is observed at higher EC (>50%) due to the non-linear increase in C_o as compared to C_m.

Comparison with SoA:

Table 2.1: Performance comparison of S0 mode resonators in X-cut LN

Paper	f (MHz)	k_t^2 (%)	Q	$FoM_1 = k_t^2 \times Q$	$FoM_2 = Q \times f$
[1]	50	30.7	5110	1568	2.55e11
[2]	395	30	1200	360	4.74e11
[3]	500	21.7	1300	282	6.5e11
[4]	427	30	737	221	3.14e11
[5]	500	10	500	50	2.5e11
[6]	520	11.5	352	40.5	1.83e11
This work	470	31	725	225	3.4e11

References:

[1] L. Colombo, A. Kochhar, G. Vidal-Alvarez, and G. Piazza, "X-Cut Lithium Niobate Laterally Vibrating MEMS Resonator with Figure of Merit of 1560," *J. Microelectromechanical Syst.*, vol. 27, no. 4, pp. 602–604, Aug. 2018

[2] F. V. Pop, A. S. Kochhar, G. Vidal-Alvarez, and G. Piazza, "Investigation of Electromechanical Coupling and Quality Factor of X-Cut Lithium Niobate Laterally Vibrating Resonators Operating Around 400 MHz," *J. Microelectromechanical Syst.*, vol. 27, no. 3, pp. 407–413, 2018.

[3] S. Gong and G. Piazza, "Figure-of-merit enhancement for laterally vibrating lithium niobate mems resonators," *IEEE Trans. Electron Devices*, vol. 60, no. 11, pp. 3888–3894, 2013.

[4] F. V. Pop, A. S. Kochhar, G. Vidal-Álvarez, and G. Piazza, "Laterally vibrating lithium niobate MEMS resonators with 30% electromechanical coupling coefficient," in *Proceedings of the IEEE International Conference on Micro Electro Mechanical Systems (MEMS)*, 2017, pp. 966–969.

[5] S. Gong and G. Piazza, "Multi-Frequency Wideband RF Filters using High Electromechanical Coupling Laterally Vibrating Lithium Niobate MEMS Resonators," pp. 785–788, 2013.

[6] S. Gong and G. Piazza, "Design and analysis of lithium-niobate-based high electromechanical coupling RF-MEMS resonators for wideband filtering," in *IEEE Transactions on Microwave Theory and Techniques*, 2013, vol. 61, no. 1, pp. 403–414.

56

2.2 Optimization of Inactive Regions of Lithium Niobate Shear Mode Resonator for Quality Factor Enhancement

2.2.1 Manuscript

Authors: Muhammad Faizan and Luis Guillermo Villanueva

Advanced NEMS Laboratory, EPFL, Lausanne, Switzerland

Authors' contribution: MF was responsible for the design, FEM simulations, fabrication and characterization of the devices. MF also made the figures and wrote the manuscript. LGV supervised the work.

Abstract

This work presents the development of a novel process flow for the fabrication of Lithium niobate Lamb wave resonator that allows full control of the shape and size of the released area (undercut) necessary for stabilizing quality factor. We then investigate the influence of the inactive regions of the resonator (i.e. undercut, anchor, bus and gap) on Q; and determine the optimum dimensions for those regions in order to limit the flow of energy escaping from the resonator's body resulting in overall improvement in Q. We report devices with electromechanical coupling (k_t^2) of 41% and quality factor (Q) of 1900 resulting in the highest-ever achieved Figure-of-Merit (FoM) of 780 for SH0 mode resonators in X-cut LN.

Introduction

The use of MEMS acoustic resonators to address the ever-growing demands of modern communications systems has been a topic of research for more than 20 years. Advances in microfabrication have presented many alternative solutions to overcome the limiting factors of size, cost, system integration and power consumption of traditional systems. Commercially, quartz-based resonators, surface-acoustic wave (SAW) and thin-film bulk acoustic (FBAR) resonators are widely used as time references and filters in mobile phones and ultra-low power radios. However, lithium niobate (LN)-based Lamb wave resonators are gaining much attention for many current and future applications as they combine the advantages of SAW and BAW devices by allowing the flexibility to determine the frequency by the electrodes' design and easier scalability to higher frequencies (>2GHz) [1]–[4].

A typical Figure of Merit (FoM) to evaluate the performance of lamb wave resonators is based on the product of electromechanical coupling (k_t^2) and quality factor (Q). The former is mainly determined by the piezoelectric material and the design of electrodes responsible for transducing motion; whereas the latter can be enhanced by the design optimization [5]–[8]. Up to now, resonators in UHF band and above have always faced a limitation in Q, which consequently affects the insertion loss [9] and out-of-band rejection for filters [10], and phase noise for oscillators [11][12].

Q is proportional to the ratio of energy stored in the resonator to energy lost per cycle. Energy dissipation mechanisms in the lamb wave resonators are broadly categorized in three groups: viscous friction to the environment (negligible in UHF and higher frequencies), material losses and acoustic radiation to the supporting substrate [13][14]. Material losses include dissipation associated to the motion, both in the piezoelectric material and in the electrodes; as well as resistive losses in the electrodes. Such losses are difficult to avoid but can be minimized by the material choice, and by using low resistive metals such as aluminum (Al), molybdenum (Mo) or Copper (Cu) for the electrodes [15][16]. Finally, the acoustic radiation to the supporting substrate mainly depends on the dimensions of the different geometrical features such as anchor, bus, and gap of the resonator [17][18]. Different optimization techniques have been reported in the past to confine the acoustic energy inside the resonator body. Proper design of the anchors or placement of acoustic reflectors at the outer ends of the anchor have shown to influence Q significantly [19]–[22]. Similarly, the aperture and gap effectively modify the stress profile in the resonator cavity, resulting in a better energy confinement [23]. Bus width can be chosen to behave as an acoustic $\lambda/4$ transformer in order to limit the flow of energy from the active region towards the anchors [24].

Among the different modes of Lamb wave resonator, zeroth order shear horizontal (SH0) mode drives its popularity for possessing the highest k_t^2. In this work, we explore the impact of various geometrical parameters such as anchors, bus and gap on the Q of SH0 mode resonator in X-cut LN and demonstrate devices with the highest achieved Q of 1900 resulting in FoM of 780. Furthermore, we develop a novel fabrication process flow and highlight the improvements made over the process flow presented earlier [25]. It allows us to model the shape and width of the undercut at the interface between the released area and the substrate that helps to minimize the variability in Q across the wafer.

Device Overview

Our device consists of an interdigitated transducer (IDT) on top of a mechanically suspended thin film of LN plate that is tethered to the substrate via two anchors. Electrodes are made of Al and have a pitch (p) of $\lambda/2$. When an AC potential is applied to the electrodes, the induced electric field generates lateral compressions and expansions in the LN cavity, exciting different Lamb wave modes. The anisotropic nature of LN requires a careful selection of a crystal cut and optimum in-plane device orientation in order to produce the desired mode with a large k_t^2. SH0 mode can be predominantly excited with the highest electromechanical coupling in X-cut LN with the device orientation of 170° from y-axis [26]. The resonance frequency of the device is set by the length (L) and width ($W = p \times N_p$) of the resonator:

$$f_{ij} = v \times \sqrt{\left(\frac{i}{2W}\right)^2 + \left(\frac{j}{2L}\right)^2} \tag{2.7}$$

where j and i are the orders of transverse and longitudinal modes, respectively. v is the acoustic phase velocity ($\approx 3800\ m/s$) and f_{ij} is the resonance frequency of the respective shear mode whereas $j = 1$ for SH0 mode and i is given by the number of electrode fingers (N_p) such as $i = N_p - 1$.
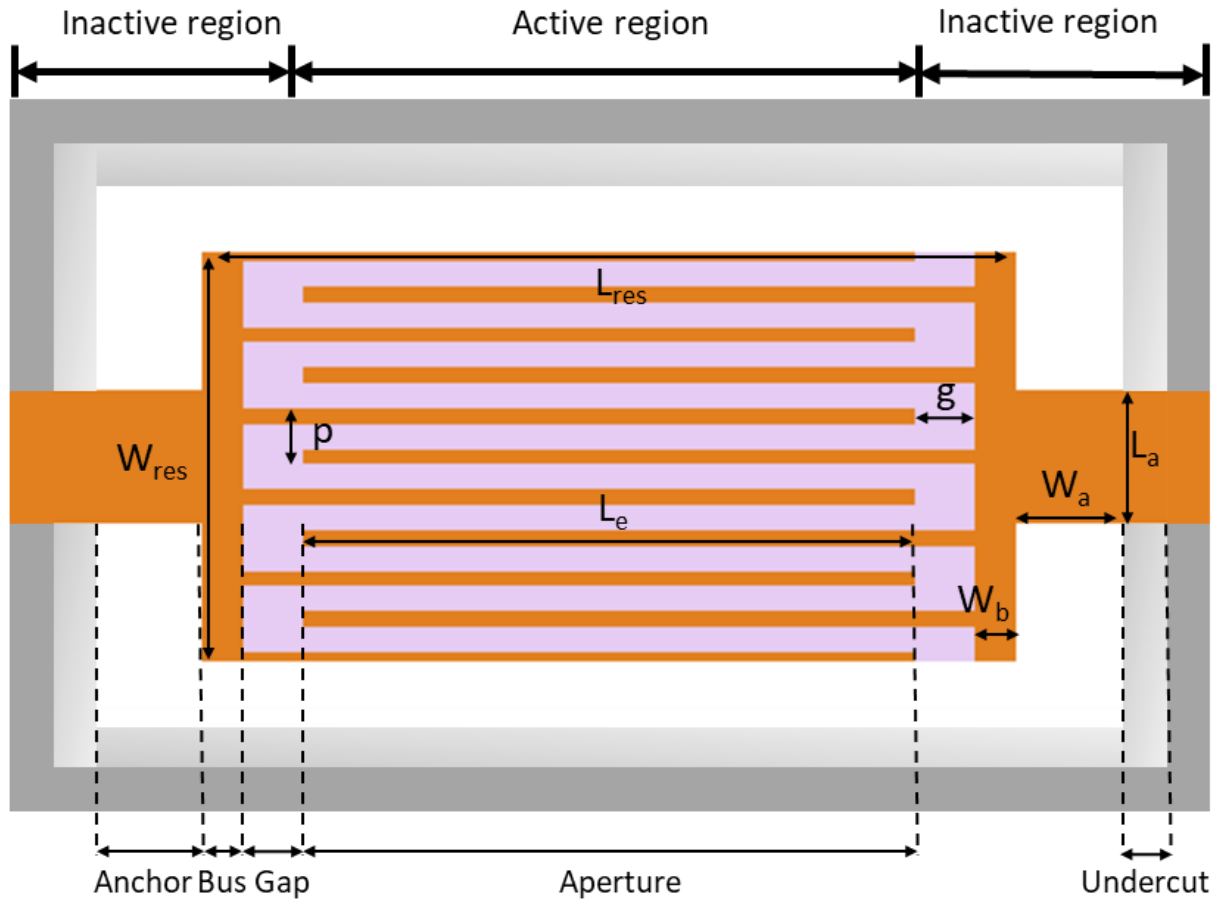
Parameter	Description	Value (μm)	Parameter	Description	Value (μm)
λ	wavelength	12	L_a	Anchor length	9, 6
L_{res}	Resonator length	120	W_a	Anchor width	9 (sweep= 3:3:12)
W_{res}	Resonator width	60	W_b	Bus width	6 (sweep= 2.4:9)
EC	Elec. coverage	1.8 (30%)	g	Gap	9 (sweep= 6:3:36)

Figure 2.15: Top view of a Lamb wave resonator's geometry. Five important regions including undercut, anchor, bus, finger-to-bus gap and aperture are illustrated. Geometrical parameters affecting resonator's performance are resonator length (L_{res}) and width (W_{res}), anchor length (L_a) and width (W_a), gap (g), electrode coverage (EC), pitch (p) and bus width (W_b). Bottom table shows the geometrical parameter values used to simulate and fabricate devices.

The geometry can be divided into active and inactive regions. The active region, also called aperture, contains IDT and is responsible for transducing motion in the resonator. The inactive region consists of undercut, anchor bus and gap that lays the path for the acoustic energy leaking into the substrate. Figure 2.15 shows the top view of the resonator geometry with the relevant design parameters. The IDT consists of a number of electrode pairs and the two half electrodes on the free edges of the resonator. These half electrodes act as reflectors to trap mechanical energy in the fundamental mode and suppress unwanted modes [27][28]. The other important design parameters are the electrode coverage (EC), which is the ratio of electrode's width over pitch; and the aperture, which is the overlap region of the electrodes. Anchor length (L_a) and width (W_a), gap (g), metal thickness (t) and bus width (W_b) determine the overall mechanical stiffness of the resonator, ultimately affecting its Q [29].

The loss of acoustic energy through the anchors into the substrate results in degrading the Q of the resonator, unless it can be returned back to the resonator cavity by placing acoustic mirrors at the outer edges of the resonator. The size and shape of the undercut has shown a significant dependence on the Q of the resonator. This phenomenon can be intuitively explained by the fact that the undercut creates an acoustic mismatch near the anchors causing the escaped energy to be reflected back towards the resonator. When the reflection is in-phase, the reflected wave adds constructively with the standing wave in the resonator's body resulting in a higher Q whereas an out-of-phase reflected wave causes destructive interference and reduces the original Q of the resonator [20]. Lozzi et al [30], demonstrated a periodic dependence of Q on the radius of circular shaped undercut with the peaks separated by a distance of $\lambda/4$ and showed 79% to 31% change in Q from peak to trough depending on the anchor width of AlN based contour mode resonators. Other studies have also shown the improvement in Q by etching a slot close to the anchors thereby creating an acoustic mismatch at the optimum distance from the anchors [20][22].

Fabrication

We present a novel process flow for the fabrication of SH0 mode resonators that allows better control on the overall release area around the device. The fabrication is done on a commercial substrate from NGK Insulators consisting of a thin film of 400 nm X-cut LN on top of a high resistive silicon (HR) wafer. The wafer is trimmed from the backside down to the thickness of 250 μm and diced into chips.
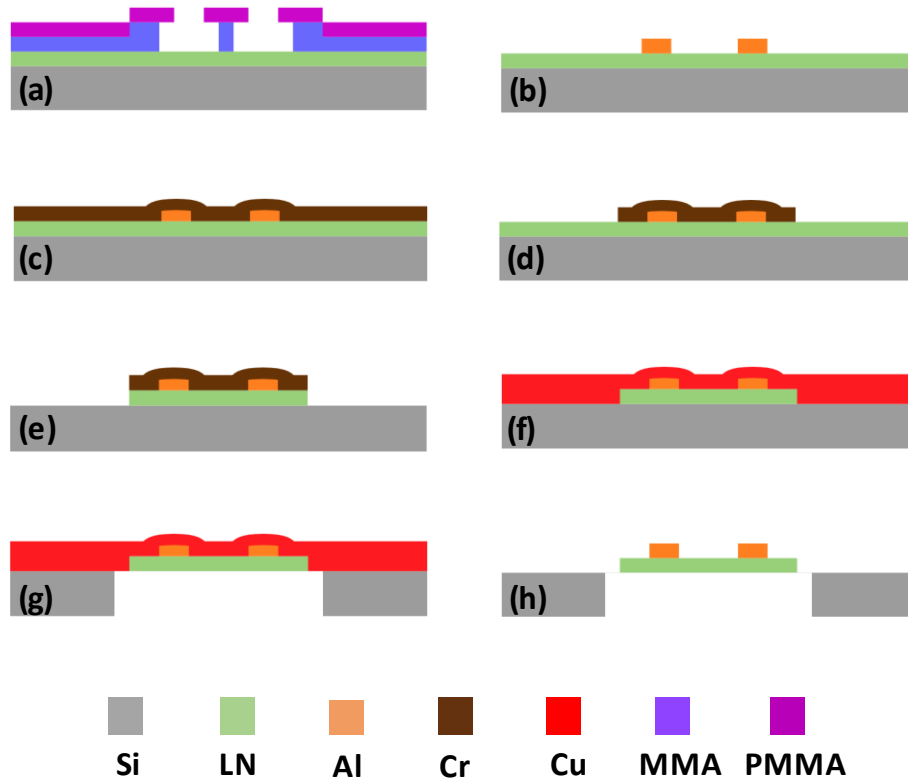
Figure 2.16: The process flow starts with the thin film of LN on top of an HR silicon substrate. The first step involves E-beam lithography of narrow electrodes using PMMA/MMA resists (a) followed by a 100 nm thick Al evaporation for metal liftoff (b). 95 nm thick Cr is evaporated and used as a hard mask for etching LN (c). Cr layer is patterned using E-beam lithography and etched in an Ion-beam etcher (IBE) (d). LN with Cr as a hard mask is etched in fluorine based Reactive Ion Etcher (RIE) until the Si underneath is exposed (e). The final step of the process flow consists of etching openings in the HR Si from the backside using Bosch process while Cu is used to protect the front side (g), and the removal of Cu once the devices are released (h).

Figure 2.16 illustrates the systematic process flow used in this work. First step of the process flow involves the liftoff of electrodes on top of LN using E-beam lithography. A 300 nm thick MMA and a 100 nm thick PMMA are used as two positive tone resists to pattern electrodes. MMA develops faster than PMMA, hence provides an undercut essential for a good liftoff process. The melting of resists during E-beam exposure is a common problem due to the accumulation of high-energy electrons coming from the electron gun [31]. These charges need to be grounded either through the substrate or by coating the chip with a layer of conductive polymer. For this purpose, a 40 nm thick layer of Electra 92 is coated on top of

the PMMA/MMA stack and a copper tape is used to provide electrical ground to the top surface of the chip. After exposure, the chip is washed with DI water to remove Electra 92 followed by resist development in MiBK:IPA 1:3 solution for 1 min. A 100 nm thick layer of Al is evaporated and the liftoff process is completed by leaving the chip in an acetone beaker overnight.
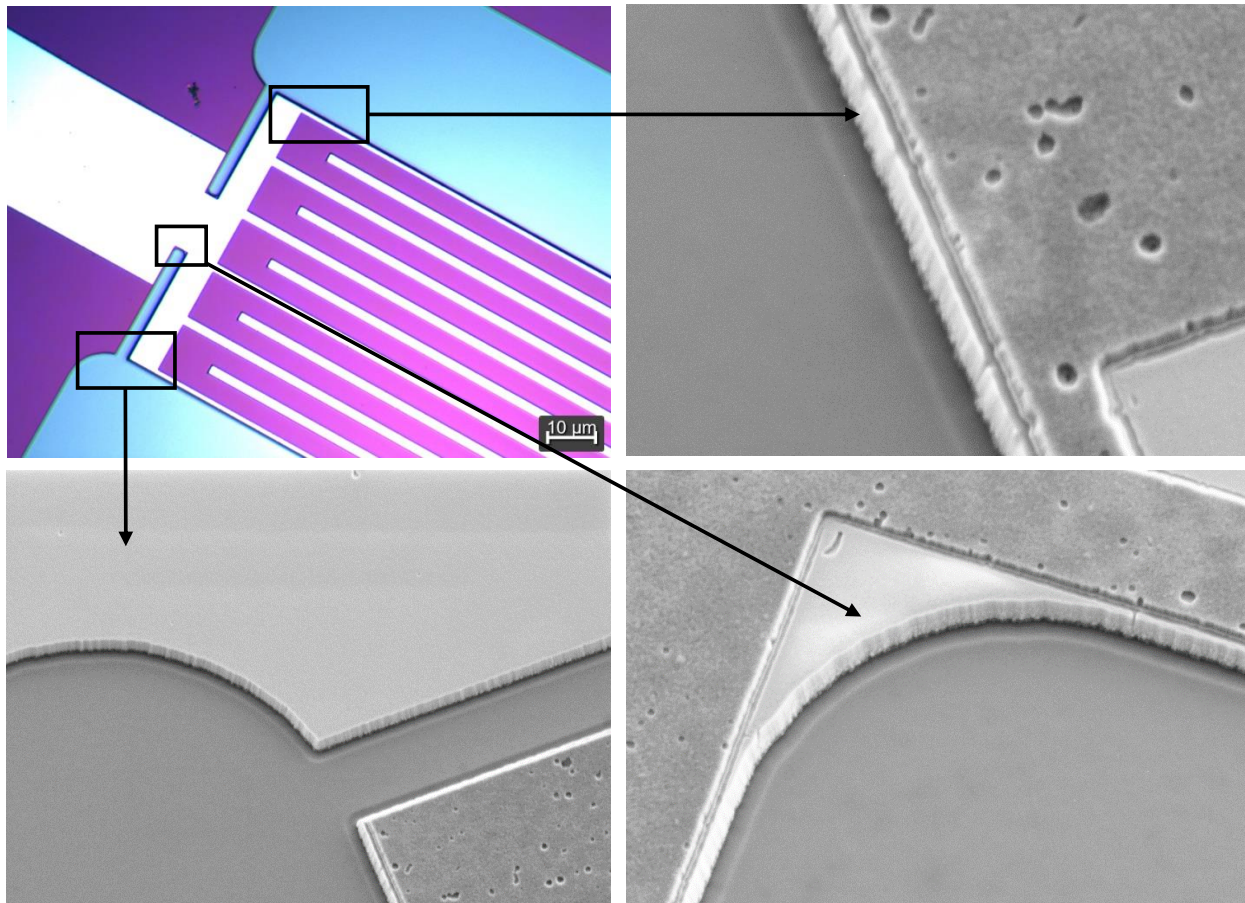
Figure 2.17: Optical image showing the frontside of the device with Al electrodes placed on etched LN (purple color) highlighting the body of the resonator. Electrodes are 100 nm thick and achieved using liftoff while LN is etched using CHF_3/Ar gases in a plasma etcher. SEM images showing different sidewall profiles of the resonator after etching all the way down to the Si substrate.

The next step involves the evaporation of a 95 nm thick layer of Cr to use as a hard mask for etching LN. Based on our experiments, Cr seems to be the best option for the hard mask as it is more resistant to dry etchings as compared with other metals and can be stripped away easily without affecting the Al

electrodes and LN surface. Again, E-beam lithography is used for the patterning of the hard mask and the reflectors are accurately aligned to the edges of the resonator body by using the automatic alignment feature of the E-beam tool. A 225 nm thick layer of a positive tone resist ZEP is used for patterning of Cr as it provides vertical sidewalls than PMMA. Cr layer is etched in Ion Beam Etcher (IBE) followed by etching of LN in a Reactive Ion Etcher (RIE) until Si is exposed. The LN etching recipe uses Ar/CHF$_3$ (100/50 sccm) gases with 6 mTorr pressure and 500 W and 300 W coil and platten powers, respectively. The recipe is fully optimized to achieve straight sidewalls with no redisposition of the etched material. Figure 2.17 shows the frontside of the device with electrodes and etched LN.
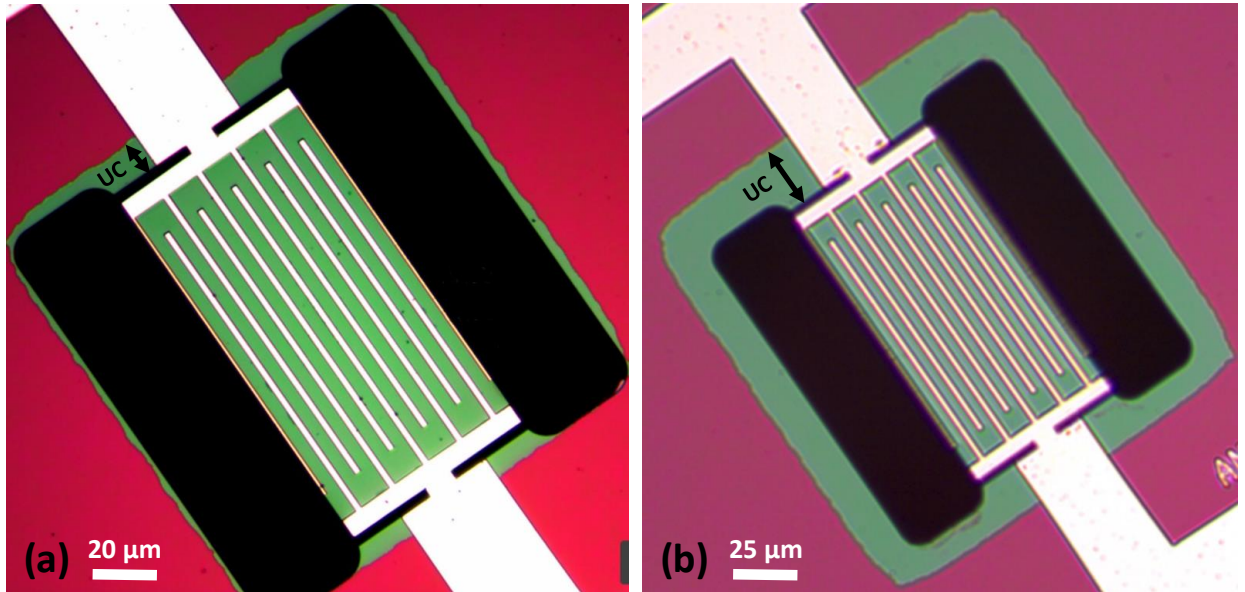
Figure 2.18: Optical images showing fully suspended devices with well-defined undercuts achieved using backside release process. (a) shows a narrow undercut of 6 µm, whereas (b) illustrates a wider undercut of 24 µm.

Suspending the devices is the final step of the process flow that requires etching Si below the devices to make deep cavities. The device release can be achieved either by etching the Si from the frontside or from the backside of the chip. If the devices are released from the frontside, the hard mask used to etch LN needs to be thick enough to sustain the long dry etching of Si using SF$_6$ (300 sccm) gas. However, Cr is a high stressed material and it has been observed that the deposition of Cr layer thicker than 150 nm on

top of Al electrodes results in peeling of the electrodes. Secondly, due to the non-conformal deposition of Cr around the electrodes (contour) the Cr is etched relatively faster and results in damaging of LN surface near the electrodes. Furthermore, frontside device release makes it difficult to have a reproducible undercut as it is very sensitive to the slight variations in etch time or size of release windows.

Backside etching of Si solves the above-mentioned fabrication problems and provides better control of the overall release area surrounding the devices. First, a thick layer of 1 µm copper (Cu) is evaporated on the frontside of the chip to avoid the breaking of devices during the release process. The chip is then flipped and placed on a wafer using Quick-Stick. At this stage, a standard optical lithography is done to pattern the openings in Si using a dual front-back alignment technique. It also allows modelling of the desired shape and width of the undercut at the device anchors. 250 µm thick Si is etched for 1 hour using Bosch process in Deep Reactive ion Etcher (DRIE) with periodic short pulses of SF_6 (300 sccm) and C_4F_8 (200 sccm) gases and with the pulse duration of 5 sec and 2 sec, respectively. After Bosch process, the chip is detached from the wafer and the Cu is removed from the frontside using wet etching. Figure 2.18 shows the optical images of fully suspended devices from the frontside with the well-defined rectangular undercuts.

Experimental Results

The devices are fabricated with Ground-Signal-Ground (GSG) pads and are measured in 1-port configuration using a Vector network Analyzer (VNA) at room temperature. The scattering parameters (S_{11}) are measured and converted to admittance parameters (Y_{11}). The admittance response is fitted to mBVD model for the extraction of important device parameters. A multi-resonance recursive fitting technique is used to fit the resonance and anti-resonance peaks along with the spurious peaks present around them [32]. Figure 2.19 shows a typical admittance response of a device together with its fitting to an mBVD model. This particular device is fabricated with the design parameters shown in Figure 2.15. The inset in Figure 2.19 shows the motional branch parameters, such as motional resistance (R_m), capacitance (C_m) and inductance (L_m); as well as the parasitic branch parameters, such as static capacitance (C_o) and substrate losses (R_0). Capacitance due to the pads (C_p) is also measured and its effect is de-embedded from the final response of the device. The performance of the device is evaluated using k_t^2 and Q calculated as follows:

$$k_t^2 = \frac{\pi^2}{8} \times \frac{C_m}{C_o} \tag{2.8}$$

$$Q = \frac{1}{R_m} \times \sqrt{\frac{L_m}{C_m}} \tag{2.9}$$

In our previous work [25], we report that the k_t^2 is mainly dependent on the electrode coverage (EC) of the device as it directly influences C_o and C_m. The increase in EC represents a reduction in the spacing between the electrodes that causes C_o to grow non-linearly as $C_o \propto \frac{1}{1-EC}$. At the same time, due to the increase in electrode area, C_m increases linearly with EC. Consequently, the k_t^2 peaks and almost remains constant for low electrode coverages from 20% to 40% whereas a significant reduction in k_t^2 is observed for higher electrode coverages (>50%). On the other hand, the Q depends on different dissipation mechanisms, including the resistive losses of the electrodes. Metals with low resistance offer a higher Q than high resistive metals. Unlike Q, for this particular mode (SH0), the mechanical quality factor ($Q_m = Q\frac{R_m}{R_m-R_s}$) is not influenced by the electrodes' material and mainly depends on the geometrical parameters of the inactive region such as gap, bus and anchors responsible for energy leakage from the resonator body.
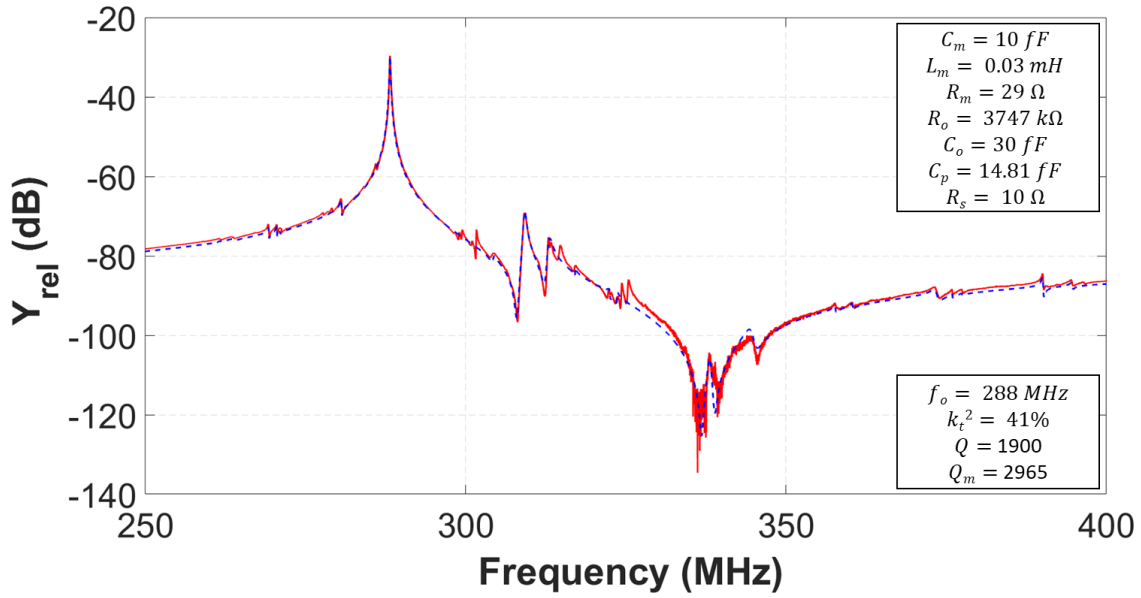
Figure 2.19: 1-port admittance response of the device with fitted mBVD model parameters. SH0 mode is predominantly produced with the in-plane device orientation of 170°, resulting in high k_t^2 and Q of 41% and 1900 respectively. Insets show the relevant mBVD model parameters.

Impact of inactive region elements on Q

To study the influence of anchor, gap and bus on Q of the resonator, the undercut needs to be controlled very well, otherwise the effect of different inactive region elements on Q will be convoluted by the variation in the shape and width of the undercut. Instead of using arbitrary undercut due to the isotropic device release, our novel fabrication flow allows us to control the shape and width of the undercut accurately (Figure 2.18). We fabricate devices with the rectangular undercut having various widths in order to determine the stability of Q due to the changing widths of the undercut. We concur that the Q of SH0 mode resonator with the rectangular undercut does not drastically affects Q and we achieve the average Q of 1200 for different widths of the undercut with the standard deviation of 13%, as shown in Figure 2.20.
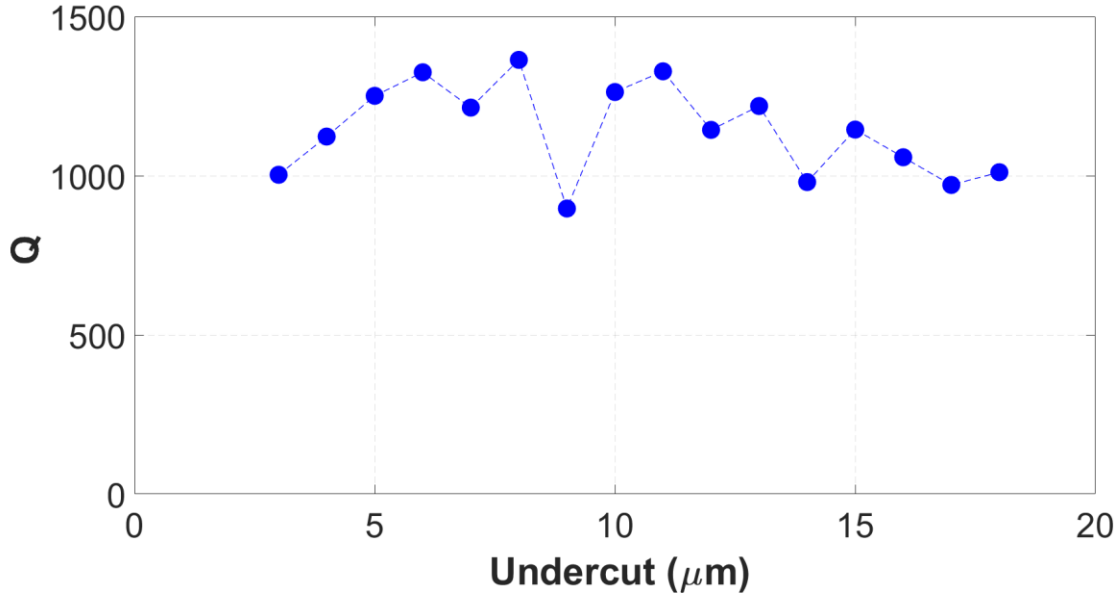
Figure 2.20: Q as a function of width of the rectangular undercuts at the anchors with the fixed device parameters of $g = \lambda$, $W_b = \lambda/2$, $W_a = 3\lambda/4$ and $L_a = 3\lambda/4$. Each data point is the average of two identical devices.

We investigate the impact of anchors, gap and bus on Q of the resonator by fixing the undercut to 6 µm and fabricate devices with the varying dimensions of inactive region elements to find the sweet spot that yields the highest Q. For this purpose, we implement the following strategy:

Anchor effect:

We fabricate two sets of devices by sweeping W_a from $\lambda/4$ to λ (in steps of $\lambda/4$) with L_a equal to $\lambda/2$ and $3\lambda/4$. Our measurements suggest that, for SH0 devices, square anchors better limit the flow of outward energy and yield the highest Q. Figure 2.21 shows the highest Q of around 1400 for two set of measurements when W_a and L_a are equal.
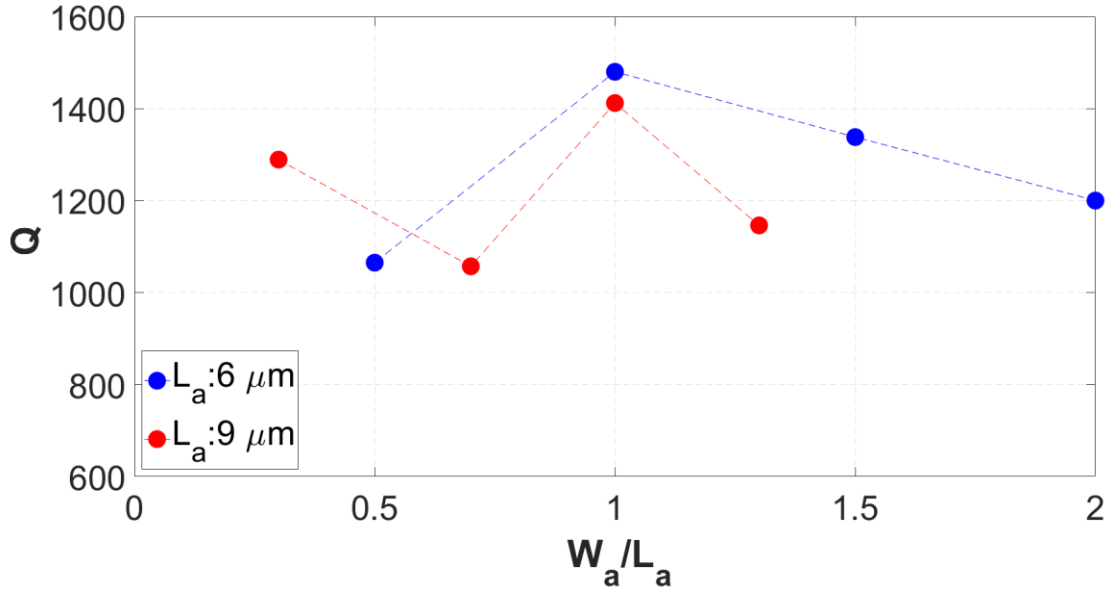
Figure 2.21: Effect of anchor dimensions (W_a and L_a) on Q of the resonator. Anchors with same equal W_a and L_a yields highest Q of around 1400 with the fixed device parameters of $W_b = \lambda/2$ and $g = \lambda$.

Bus and gap effect:

We study the combined effect of bus and gap on Q as both parameters effectively change the aperture of the device having a fixed plate length (L_{res}) [33]. We fabricate devices with $W_b = 0.3\lambda$, 0.5λ and 0.75λ with the g swept from 0.5λ to 3λ in the steps of 0.25λ. The Q increases with the increase in g and peaks at 1900 for $g = 2\lambda$. Further increase in g results in reduction of Q as the active region of the resonator, responsible for mode transduction, shrinks significantly. The dependence of Q on g almost remains the same for different values of W_b as shown in Figure 2.22.
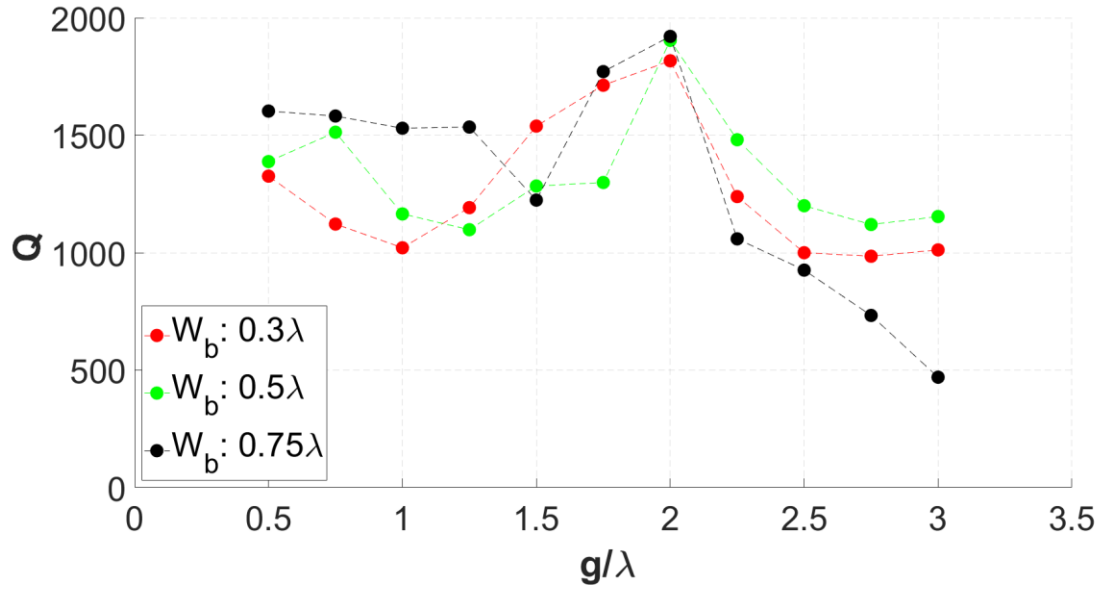
Figure 2.22: Effect of finger to bus gap (g) on Q of the resonator. For different values of W_b, Q shows similar trend with a maxima around 1900 at $g = 2\lambda$ with the fixed device parameters of $W_a = 3\lambda/4$ and $L_a = 3\lambda/4$. Each data point is the average of two identical devices.
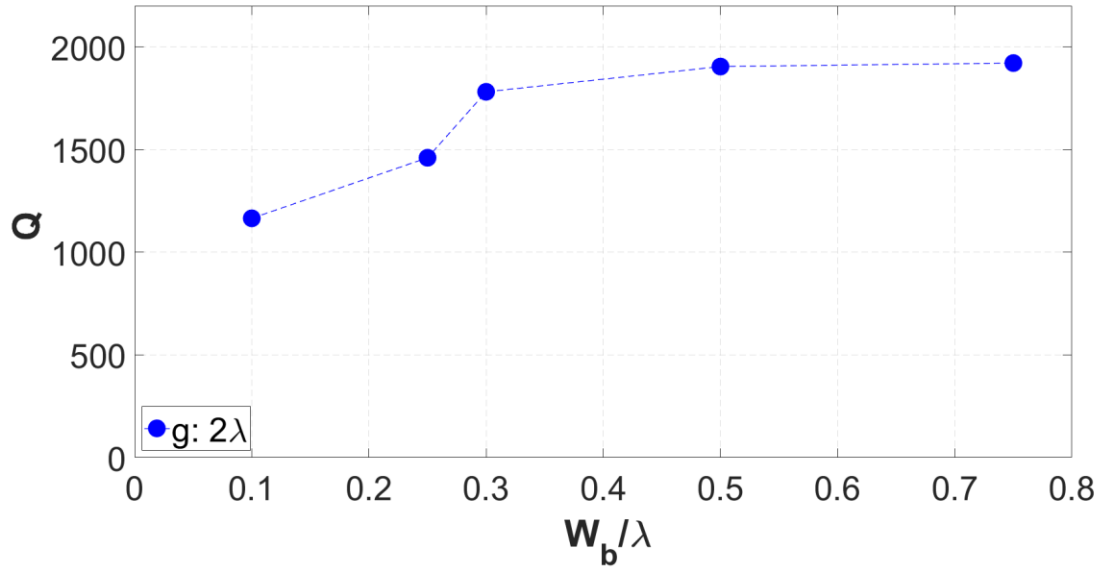
Figure 2.23: Effect of bus width (W_b) on Q of the resonator. Q saturates and almost remains constant for $W_b > 0.3\lambda$. Highest Q of 1900 is achieved for the W_b of 0.75λ with the fixed device parameters of $W_a = 3\lambda/4$, $L_a = 3\lambda/4$ and $g = 2\lambda$. Each data point is the average of two identical devices.

Similarly, another set of devices is fabricated with W_b ranging from 0.1λ to 0.75λ with the fixed $W_a = 3\lambda/4$ and $L_a = 3\lambda/4$. Variation in Q for $W_b > 0.3\lambda$ drops significantly and almost remains constant with the maxima of 1900 at $W_b = 0.75\lambda$, as shown in Figure 2.23.

Conclusion

This work demonstrates a novel process flow for the fabrication of LN based SH0 mode resonators that allows full control of the width and shape of the release area. Usually, the devices are released by an isotropic etching of Si that not only suspends the device but also the region outside the anchors. According to previous studies, a small variation in the width of the release region drastically affects Q that leads to a non-predictable response of the resonator. In this work, we use DRIE of Si using Bosch process to release the devices from the backside, achieving well-defined undercuts in order to realize a stable and reproducible Q.

We also investigate the dependence of Q on various geometrical parameters such as anchor, gap, bus and width of the undercut. Our measurements suggest that longer inactive region seems to improve Q of the resonator. Each inactive region element such as anchor, bus and gap plays an very important role in containing energy within the resonator and enhancing the Q. The highest Q of 1900 is achieved for the design parameters of $g = 2\lambda$, $W_b = 3\lambda/4$, $W_a = 3\lambda/4$ and $L_a = 3\lambda/4$ resulting in the highest-ever achieved Figure-of-Merit (FoM) of 780 for SH0 mode resonators in X-cut LN.

References

[1]   S. Gong, "Lithium Niobate for M/NEMS Resonators," in *Piezoelectric MEMS Resonators*, H. Bhugra and G. Piazza, Eds. Springer International Publishing Switzerland 2017, 2017, pp. 99–129.

[2]   V. Yantchev and I. Katardjiev, "Thin film Lamb wave resonators in frequency control and sensing applications: A review," *J. Micromechanics Microengineering*, vol. 23, no. 4, 2013.

[3]   J. Zou *et al.*, "Ultra-Large-Coupling and Spurious-Free SH0 Plate Acoustic Wave Resonators Based on Thin LiNbO3," *IEEE Trans. Ultrason. Ferroelectr. Freq. Control*, vol. 67, no. 2, pp. 374–386, 2020.

[4]   G. Piazza, V. Felmetsger, P. Muralt, R. H. Olsson, and R. Ruby, "PIEZOELECTRIC ALUMINUM

NITRIDE THIN FILMS FOR MICROELECTROMECHANICAL SYSTEMS," *MRS Bull.*, 2012.

[5] Z. A. Schaffer, L. Colombo, A. S. Kochhar, G. Piazza, S. Mishin, and Y. Oshmyansky, "Experimental investigation of damping factors in 20% scandium-doped aluminum nitride laterally vibrating resonators," in *Proceedings of the IEEE International Conference on Micro Electro Mechanical Systems (MEMS)*, 2018, vol. 2018–January, pp. 787–790.

[6] A. Lozzi, E. Ting-Ta Yen, P. Muralt, and L. G. Villanueva, "Al0.83Sc0.17N Contour-Mode Resonators with Electromechanical Coupling in Excess of 4.5%," *IEEE Trans. Ultrason. Ferroelectr. Freq. Control*, vol. 66, no. 1, pp. 146–153, Jan. 2019.

[7] J. Zou *et al.*, "Design of Ultra-Large-Coupling SH0 Plate Wave Resonators on LiNbO3 with Clean Spectrum," *IFCS/EFTF 2019 - Jt. Conf. IEEE Int. Freq. Control Symp. Eur. Freq. Time Forum, Proc.*, no. July, 2019.

[8] Y. H. Song and S. Gong, "Elimination of spurious modes in SH0 Lithium Niobate laterally vibrating resonators," *IEEE Electron Devices Lett.*, vol. 36, no. 11, pp. 1198–1201, 2015.

[9] M. Rinaldi, C. Zuniga, C. Zuo, and G. Piazza, "Ultra-thin super high frequency two-port AlN contour-mode resonators and filters," in *TRANSDUCERS 2009 - 15th International Conference on Solid-State Sensors, Actuators and Microsystems*, 2009, pp. 577–580.

[10] M. Kadota and S. Tanaka, "Ultra-wideband ladder filter using SH0 plate wave in thin LiNbO3 plate and its application to tunable filter," *IEEE Trans. Ultrason. Ferroelectr. Freq. Control*, vol. 62, no. 5, pp. 939–946, 2015.

[11] A. Lozzi, M. Liffredo, E. T. T. Yen, J. Segovia-Fernandez, and L. G. Villanueva, "Evidence of Smaller 1/F Noise in AlScN-Based Oscillators Compared to AlN-Based Oscillators," *J. Microelectromechanical Syst.*, 2020.

[12] A. Kourani *et al.*, "A 150 MHz voltage controlled oscillator using lithium niobate RF-MEMS resonator," in *IEEE MTT-S International Microwave Symposium Digest*, 2017, pp. 1307–1310.

[13] R. N. Candler *et al.*, "Investigation of energy loss mechanisms in micromechanical resonators," in *TRANSDUCERS 2003 - 12th International Conference on Solid-State Sensors, Actuators and Microsystems, Digest of Technical Papers*, 2003, vol. 1, pp. 332–335.

[14] J. Segovia-Fernandez, M. Cremonesi, C. Cassella, A. Frangi, and G. Piazza, "Experimental study on

the impact of anchor losses on the quality factor of contour mode AlN resonators," in *2013 Transducers and Eurosensors XXVII: The 17th International Conference on Solid-State Sensors, Actuators and Microsystems, TRANSDUCERS and EUROSENSORS 2013*, 2013, pp. 2473–2476.

[15]   H. J. Kim, S. I. Jung, J. Segovia-Fernandez, and G. Piazza, "The impact of electrode materials on 1/f noise in piezoelectric AlN contour mode resonators," *AIP Adv.*, vol. 8, no. 5, 2018.

[16]   T. Zhang, H. Zhang, Z. Wang, and S. Zhang, "Effects of electrodes on performance figures of thin film bulk acoustic resonators," *J. Acoust. Soc. Am.*, vol. 122, no. 3, pp. 1646–1651, 2007.

[17]   L. Colombo, A. Kochhar, G. Vidal-Álvarez, and G. Piazza, "Investigations on the Quality Factor of Lithium Niobate Laterally Vibrating Resonators with Figure of Merit Greater than 1,500," *IEEE Int. Ultrason. Symp. IUS*, vol. 2018–Octob, pp. 2–5, 2018.

[18]   J. Segovia-Fernandez, M. Cremonesi, C. Cassella, A. Frangi, and G. Piazza, "Anchor losses in AlN contour mode resonators," *J. Microelectromechanical Syst.*, vol. 24, no. 2, pp. 265–275, Apr. 2015.

[19]   C. M. Lin, J. C. Hsu, D. G. Senesky, and A. P. Pisano, "Anchor loss reduction in ALN Lamb wave resonators using phononic crystal strip tethers," *IFCS 2014 - 2014 IEEE Int. Freq. Control Symp. Proc.*, 2014.

[20]   B. Gibson, K. Qalandar, C. Cassella, G. Piazza, and K. L. Foster, "A Study on the Effects of Release Area on the Quality Factor of Contour-Mode Resonators by Laser Doppler Vibrometry," *IEEE Trans. Ultrason. Ferroelectr. Freq. Control*, vol. 64, no. 5, pp. 898–904, 2017.

[21]   A. Lozzi, L. G. Villanueva, and E. T. T. Yen, "Anchor loss dependence on electrode materials in contour mode resonators," in *2016 IEEE International Frequency Control Symposium, IFCS 2016 - Proceedings*, 2016.

[22]   B. P. Harrington and R. Abdolvand, "In-plane acoustic reflectors for reducing effective anchor loss in lateral-extensional MEMS resonators," *J. Micromechanics Microengineering*, vol. 21, no. 8, 2011.

[23]   Y. H. Song and S. Gong, "Spurious mode suppression in SH0 Lithium Niobate laterally vibrating MEMS resonators," in *Technical Digest - International Electron Devices Meeting, IEDM*, 2015, vol. 2016–February, p. 18.5.1-18.5.4.

[24] C. Cassella, N. Singh, B. W. Soon, and G. Piazza, "Quality Factor Dependence on the Inactive Regions in AlN Contour-Mode Resonators," *J. Microelectromechanical Syst.*, vol. 24, no. 5, pp. 1575–1582, 2015.

[25] M. Faizan and L. G. Villanueva, "Frequency - Scalable Fabrication Process Flow for Lithium Niobate Based Lamb Wave Resonators," *J. Micromech. Microeng.*, vol. 30, pp. 2–7, 2020.

[26] I. E. Kuznetsova, B. D. Zaitsev, S. G. Joshi, and I. A. Borodina, "Investigation of acoustic waves in thin plates of lithium niobate and lithium tantalate," *IEEE Trans. Ultrason. Ferroelectr. Freq. Control*, vol. 48, no. 1, pp. 322–328, Jan. 2001.

[27] S. Gong and G. Piazza, "Figure-of-merit enhancement for laterally vibrating lithium niobate mems resonators," *IEEE Trans. Electron Devices*, vol. 60, no. 11, pp. 3888–3894, 2013.

[28] S. Gong and G. Piazza, "Multi-Frequency Wideband RF Filters using High Electromechanical Coupling Laterally Vibrating Lithium Niobate MEMS Resonators," pp. 785–788, 2013.

[29] F. V. Pop, A. S. Kochhar, G. Vidal-Alvarez, and G. Piazza, "Investigation of Electromechanical Coupling and Quality Factor of X-Cut Lithium Niobate Laterally Vibrating Resonators Operating Around 400 MHz," *J. Microelectromechanical Syst.*, vol. 27, no. 3, pp. 407–413, 2018.

[30] A. Lozzi, A. De Pastina, E. T. T. Yen, and L. G. Villanueva, "Engineered acoustic mismatch for anchor loss control in contour mode resonators," *Appl. Phys. Lett.*, vol. 114, no. 10, 2019.

[31] M. Faizan *et al.*, "Fabrication of Lithium Niobate Bulk Acoustic Resonator for 5G Filters," in *2019 20th International Conference on Solid-State Sensors, Actuators and Microsystems and Eurosensors XXXIII, TRANSDUCERS 2019 and EUROSENSORS XXXIII*, 2019, pp. 1752–1755.

[32] R. Lu, M. H. Li, Y. Yang, T. Manzaneque, and S. Gong, "Accurate extraction of large electromechanical coupling in piezoelectric MEMS resonators," *J. Microelectromechanical Syst.*, vol. 28, no. 2, pp. 209–218, 2019.

[33] Y. H. Song, R. Lu, and S. Gong, "Analysis and removal of spurious response in SH0 lithium niobate MEMS resonators," *IEEE Trans. Electron Devices*, vol. 63, no. 5, pp. 2066–2073, 2016.

2.2.2 Supplementary information

Fab issues

Releasing the devices from the frontside requires a thick layer of hard mask which is needed to etch a deep cavity in Si substrate while providing protection to the electrode. Among different metals, Cr is the best available choice for the hard mask as it can sustain long duration of dry etching and can be stripped away without affecting LN surface and Al electrodes. However, Cr is a high stressed material and it has been observed that a layer of Cr thicker than 150 nm peels off the underneath electrodes. Furthermore, long duration of dry etchings from the top side damages the surface of LN around the electrodes due to the non-conformal deposition of Cr as compared with the rest of the resonator surface as shown in Figure 2.24.

Releasing the device from the backside requires opening release windows from the backside of the chip by first patterning via optical lithography followed by Bosch process to etch deep cavities in the Si substrate all the way to the LN layer. However, for the successful release of devices, it is essential that backside layout layer be accurately aligned to the frontside device layer, as shown in Figure 2.25. For the devices with a SiO_2 layer buried in between LN layer and Si substrate, the release process includes one more step of etching SiO_2 using HF or BHF solution. It is observed that an opening is created from the backside of the chip to the front side due to the bending in the membrane. HF or BHF solution can seep through the opening and damage the Al electrodes on the front side, as shown in Figure 2.26. Keeping in view the fabrication challenges that arise due to the presence of buried SiO_2, the work mentioned in the publication 'Optimization of Inactive Regions of Lithium Niobate Shear Mode Resonator for Quality Factor Enhancement' has been done on thin film LN on top of HR Si wafer.

Backside release process gives full control on the size and shape of the undercut necessary for stabilizing Q. Figure 2.27 shows the SEM images of the backside of the resonators with rectangular and semi-circular undercuts. Figure 2.28 shows the successful fabrication of LN lamb wave resonator with Al electrodes using the backside release process.
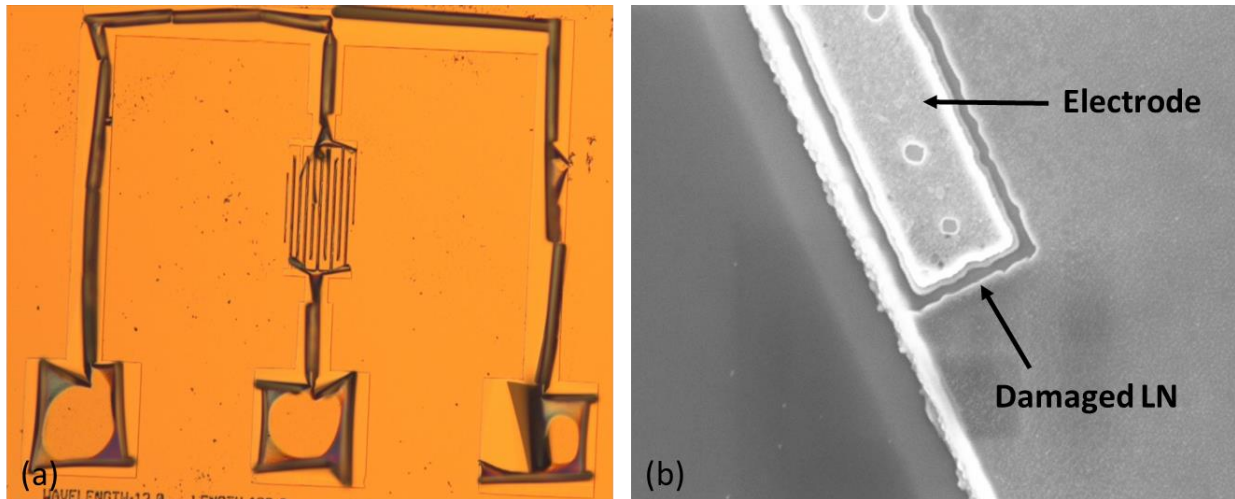
Figure 2.24: Device images highlighting some of the problems in the front side device release process which requires Cr to be thick enough to sustain the long dry etching of LN as well as Si, while protecting the front side of the device. (a) Optical image showing peeling of Al electrodes after the deposition of 150 nm thick Cr due to the high stress of Cr layer. (b) SEM image illustrating the damaging of LN around the electrodes due to the non-conformal deposition of Cr. Thicker Cr layer as a hard mask can avoid damaging of LN but results in peeling of electrodes.
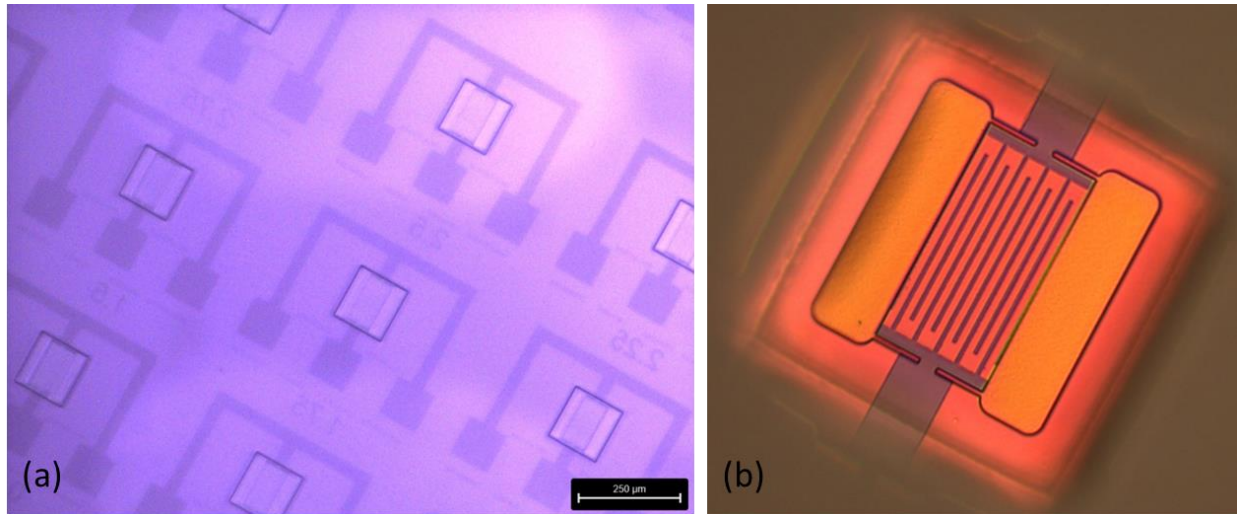
Figure 2.25: Suspending the devices from the backside requires an accurate alignment of release windows on the backside of the chip to the devices on the frontside. The size and shape of the release windows is selected based on the modelling of the undercut close to the anchors. Any misalignment between the front and backside layers can lead to the unsuccessful release of devices. (a) Optical image from IR microscope shows the patterning of release windows achieved via optical lithography, perfectly aligning with the devices on the frontside of the chip. (b) Optical image showing the device from the backside after etching a deep cavity via Bosch process in the backside of the chip all the way to the frontside.
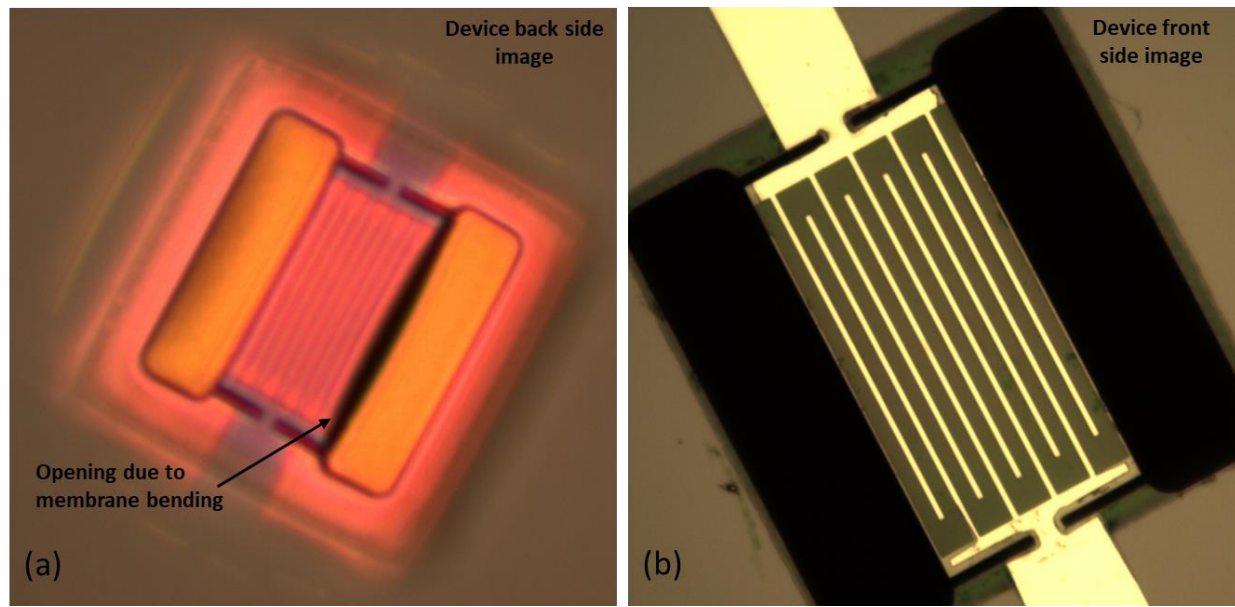
Figure 2.26: Optical image with the out of plane focus showing the bending of membrane due to stress and creating an opening from the back of the chip to the frontside. It can be problematic for device release when buried SiO_2 is used between LN layer and Si substrate as HF or BHF solution can seep through the opening and damage the electrodes during the SiO_2 removal step. (b) Optical image of the completely released device where buried SiO_2 is removed using HF solution after etching a cavity in Si from the backside of the chip. Due to the opening, HF solution etched the reflectors of the IDT and also removed metal from the edges of the bus and anchors.
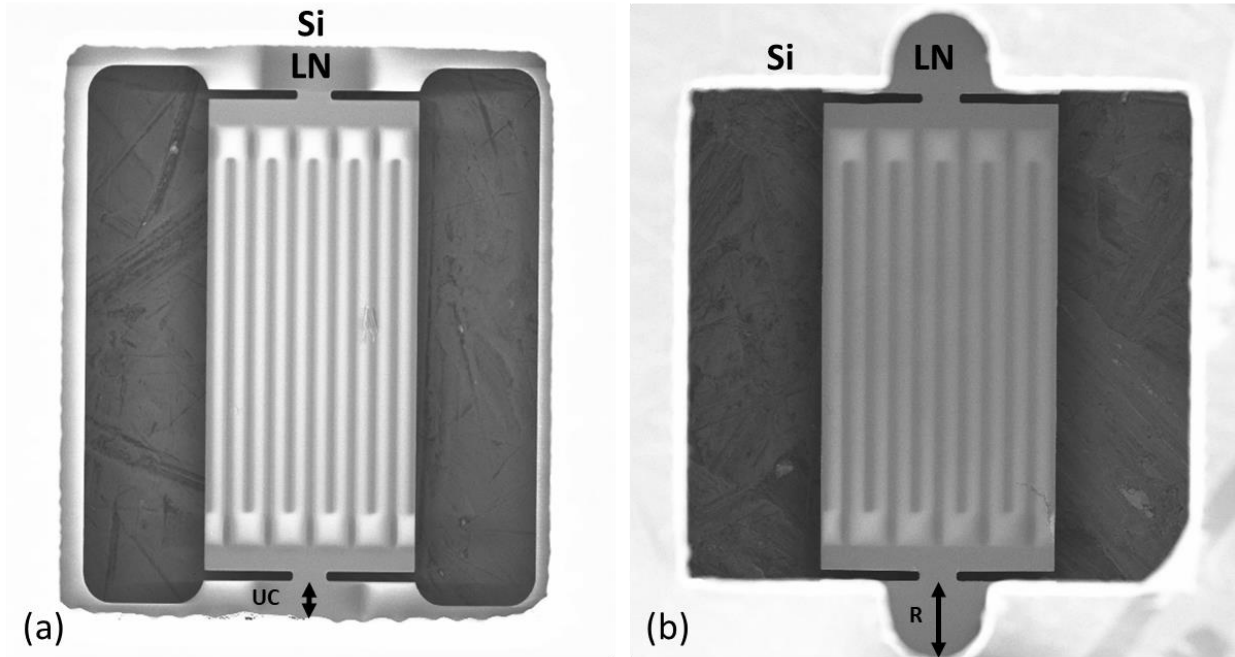
Figure 2.27: SEM images of the backside of the resonator after etching Si using Bosch process. Desired shape and width of an undercut at the interface between the released area and the substrate close to the anchors is achieved using standard optical lithography. A carefully chosen shape such as (a) rectangular or (b) circular undercut with appropriate width effectively modifies acoustic boundary conditions at the anchors in order to reflect the escaped energy in-phase back to the resonator, resulting in an improved quality factor.
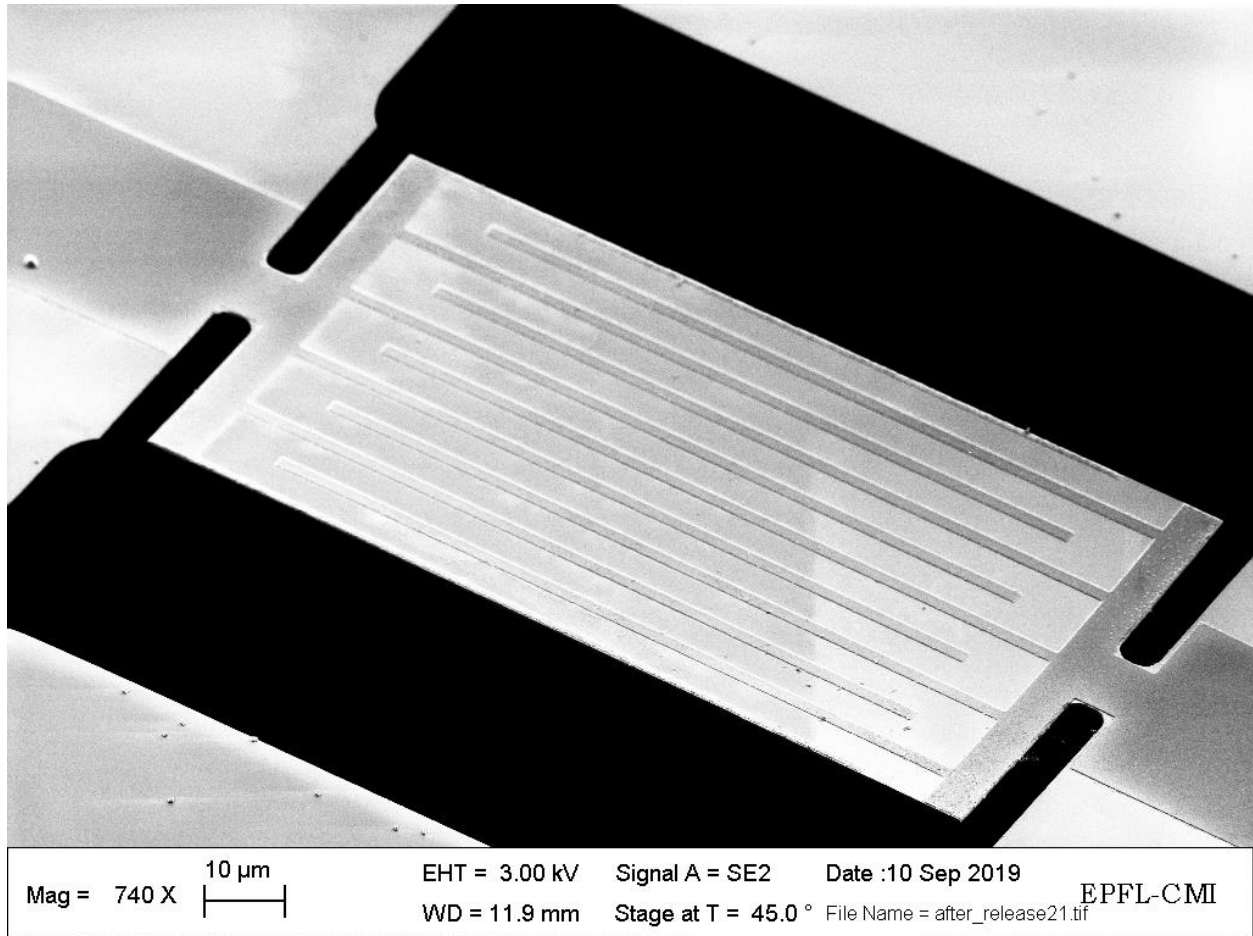
Figure 2.28: SEM image of the fully released LN based Lamb wave resonator with Al electrodes

Comparison with SoA:

Table 2.2: Performance comparison of SH0 mode resonators in X-cut LN

Paper	f (MHz)	k_t^2 (%)	Q	$FoM_1 = k_t^2 \times Q$	$FoM_2 = Q \times f$
[1]	150	20	1150	231	1.72e11
[2]	150	20.6	1064	219	1.59e11
[3]	135	17.8	920	163	1.24e11
[4]	95	14.1	1093	154	1.03e11
[5]	101	12.4	1300	161	1.31e11
This work	290	41	1900	779	5.51e11

References:

[1] Y. H. Song, R. Lu, and S. Gong, "Analysis and removal of spurious response in SH0 lithium niobate MEMS resonators," *IEEE Trans. Electron Devices*, vol. 63, no. 5, pp. 2066–2073, 2016.

[2] Y. H. Song and S. Gong, "Spurious mode suppression in SH0 Lithium Niobate laterally vibrating MEMS resonators," *Tech. Dig. - Int. Electron Devices Meet. IEDM*, vol. 2016–Febru, p. 18.5.1-18.5.4, 2015.

[3] Y. H. Song and S. Gong, "Elimination of spurious modes in SH0 Lithium Niobate laterally vibrating resonators," *IEEE Electron Devices Lett.*, vol. 36, no. 11, pp. 1198–1201, 2015.

[4] Y.-H. Song and S. Gong, "Arraying SH0 Lithium Niobate laterally vibrating resonators for mitigation of higher order spurious modes," in *MEMS*, 2016, vol. 7, no. January, pp. 111–114.

[5] R. H. Olsson *et al.*, "A high electromechanical coupling coefficient SH0 Lamb wave lithium niobate micromechanical resonator and a method for fabrication," *Sensors Actuators, A Phys.*, vol. 209, pp. 183–190, Mar. 2014.

2.3 Fabrication of Lithium Niobate Bulk Acoustic Resonator for 5G Filters

2.3.1 Manuscript

Authors: Muhammad Faizan[1], Annalisa De Pastina[1], Soumya Yandrapalli[1,2,3], Patrick J. Turner[3], Robert B. Hammond[3], Victor Plessky[2,3] and Luis Guillermo Villanueva[1]

[1] Advanced NEMS Laboratory, EPFL, Lausanne, Switzerland
[2] GVR Trade SA, Georgier, Neuchatel, Switzerland and
[3] Resonant Inc., Santa Barbara, CA, USA

Authors' contribution: MF[1] and ADP[1] were responsible for the complete fabrication of the devices. SY[1,2,3] simulated the FEM model as well as characterized the devices. MF[1] and ADP[1] also made the figures and wrote the manuscript. PJT[3,] RBH[3], VP[2,3] and LGV[1] participated in the discussions regarding the results interpretation and reviewed the paper. LGV[1] supervised the project.

Abstract

This work presents the fabrication of a MEMS resonant device which addresses the need for high quality and miniaturized RF filters in the 3–6 GHz range for 5th generation (5G) mobile networks. The 4-mask fabrication process is based on the definition of interdigitated Aluminum (Al) electrodes on a suspended membrane of 400 nm-thick Z-cut lithium niobate (LiNbO$_3$). Devices are fabricated with a yield of 70% and exhibit high electromechanical coupling (k_t^2) and quality factor (Q) up to 28% and 300, respectively, for frequencies around 5 GHz.

Introduction

Over the past decades, wireless communication networks have been aggressively developing to adapt to the increasing customer needs. In particular, the access to the third and fourth generation (3G/4G) networks has accelerated the smartphone trend, enabling high quality video download and upload, and resulting in peak data rates. Hence, the 3G and 4G bands are currently congested with broadcasting and communication applications.

Microelectromechanical systems (MEMS), in particular surface acoustic waves (SAW) and film bulk acoustic resonators (FBAR) are nowadays the leading technologies in the market for RF front-end filters up to 2.5 GHz [1].

The SAW technology dominates the low-band frequency applications (<1 GHz). SAW devices generate and detect acoustic waves using interdigital transducers (IDT) on the surface of a piezoelectric (PZE) crystal substrate. The resonance frequency and the exponential decay of the acoustic wave are strongly dependent on the electrode dimension and pitch. This makes it difficult to reach higher frequencies as this would require nm-range precision in the electrodes patterning, thus increasing the costs within the fabrication process [2, 3].

Mid and high band frequencies up to 2.5 GHz are dominated by FBAR resonators, which exhibit efficient power handling and relative insensitivity to electrostatic discharge [1]. They consist of a thin film PZE material sandwiched between two thin film electrodes, and acoustically isolated from the surrounding medium. The resonance frequency of the FBARs is determined by the thickness of the PZE layer: this easily enables high frequency ranges. However, frequency tunability is rather difficult, as it is limited by the thickness control in thin film deposition processes. In fact, differently from SAW devices, where a high quality PZE crystal is used, FBARs typically use polycrystalline PZE layers, deposited via chemical vapor deposition (CVD) or sputtering. This increases the mechanical losses in the material [1].

To attain high performance and wide bandwidth, MEMS resonators must feature a high figure of merit ($FoM = k_t^2 \cdot Q$): high electromechanical coupling (k_t^2) and quality factor (Q) are simultaneously needed. Current technologies in the 4G frequency bands struggle to keep up with the demanding 4G and upcoming 5G standards at high frequencies [1].

In this paper, we present the fabrication process developed for a novel piezoacoustic resonator, designed for high quality and miniaturized RF filters in the 3–6 GHz range, for 5G mobile networks.

Device Design

Our novel device is a bulk-acoustic resonator which consists of a 400 nm-thick suspended $LiNbO_3$ membrane with periodic pairs of interdigital metal electrodes on top, for the excitation of anti-symmetrical shear modes [4]. It combines the advantages of current RF-filter leading technologies, as (i) it is made of crystalline PZE material, (ii) the PZE thickness-defined frequency enables high frequency bands, whereas the electrodes' pitch provides up to 2.5% frequency tunability, (iii) the electrodes barely participate to the device vibration, further limiting mechanical losses.
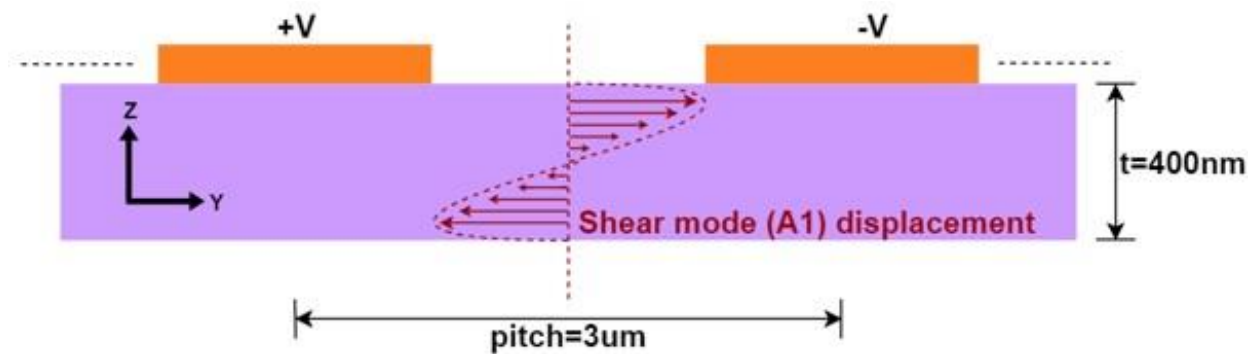
Figure 2.29: Schematic diagram of our device with z-axis perpendicular to the $LiNbO_3$ surface. Due to alternate polarity of electrodes, the electric field is distributed along the y-axis. The anti-symmetrical shear mode (A1) is confined between the electrodes, which do not take part to the vibration of the device.

The design consists of 25 to 50 pairs of IDTs fabricated on top of 60 to 80 µm -wide $LiNbO_3$ membranes with fixed edges. Al is used for the electrodes since Al offers low acoustic loss and ease of fabrication. The electrodes are 100 nm thick and 500 nm wide with a pitch (p) of 3-5 µm.

$LiNbO_3$ is a highly anisotropic material which requires the resonator to be oriented in a specific direction along the chip in order to excite a particular mode with high efficiency [5, 6]. For this work, Z-cut $LiNbO_3$ is used with the device orientation of 0 degrees with respect to the y-axis. Strong PZE coefficient e_{24} of Z-cut $LiNbO_3$ is suitable for the excitation of shear horizontal (SH) modes with standing waves in Z-direction and electric field in Y-direction, as shown in Figure 2.29. The alternating polarity of the electrodes creates an electric field mainly in the Y-direction that generates lateral compressions and expansions in the

material. The main resonance is treated as shear bulk wave fundamental mode (A1) with thickness of the membrane being half the acoustic wavelength (t=λ/2).

Fabrication

The developed fabrication process consists of 4 masks and allows the fabrication of suspended $LiNbO_3$ membranes with periodic pairs of interdigital metal electrodes on top, with a yield of 70%.

The fabrication starts from a commercial substrate from NanoLN [7], consisting of a 3-inches Si carrier wafer coated with 2 µm PECVD SiO_2 and 400 nm layer of $LiNbO_3$. A 2 µm-thick Al layer is evaporated on top of $LiNbO_3$ in order to protect the PZE material during the following process steps. The wafer is thinned down to 250 µm and diced into 10x13 mm chips. The chip-level fabrication is schematically represented in Figure 2.30.
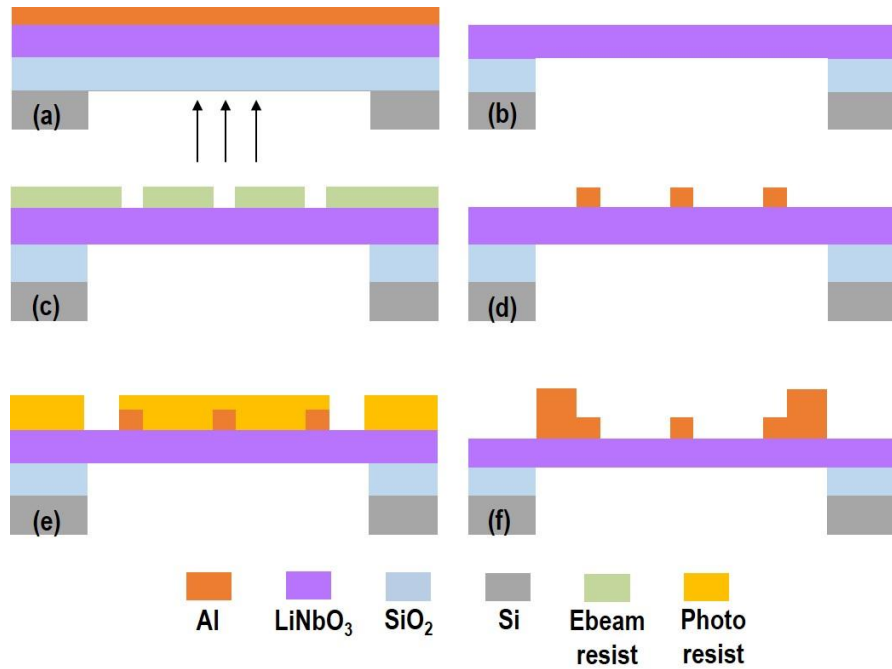
Figure 2.30: Fabrication process flow for our device that first includes backside release of $LiNbO_3$ membrane by (a) dry etching of Si using SF_6 and (b) wet etching of SiO_2 using 49% HF solution followed by wet Al strip. The following front-side fabrication requires (c) patterning of interdigitated electrodes via E-beam lithography and (d) Al evaporation for electrodes liftoff. Electrical pads are defined via liftoff through optical lithography (e) and Al evaporation (f).

Lithium niobate membranes:

LiNbO$_3$ membranes are defined from the backside of the substrate. The chip is glued on a carrier silicon wafer using temporary mounting wax (QuickStickTM 135). The PZE layer is oriented towards the wafer surface and is protected from damage by the Al layer. The silicon backside of the chip is patterned via photolithography, in order to define the geometry of lithium niobate membranes (60 to 80 µm wide, 170 to 520 µm long). The geometry is transferred through the chip thickness until reaching the SiO$_2$ layer, via Bosch® process dry etching. The etching parameters have been optimized to 7 sec SF$_6$ (300 sccm) and 2 sec C$_4$F$_8$ (200 sccm), which result into vertical walls through the 250 µm-deep Si chip, and fast etching rate (~5 µm/min). Subsequently, the residual photoresist is removed from the backside of the chip via O$_2$ plasma etching.

The chip is carefully removed from the carrier wafer by heating it at 135°C to melt the mounting wax, and gently sliding the chip on the surface of the wafer. Particular attention is needed in order to preserve the thin SiO$_2$/LiNbO$_3$/Al membranes during this operation. The surface of the chip is cleaned in acetone and isopropyl alcohol (IPA) in order to remove wax residues. The membranes are finally released via wet etching of SiO$_2$ in 50% HF solution, followed by wet etching of Al via commercial solution (MicroChemicals GmbH). Chips are rinsed in abundant deionized (DI) water, later immersed in IPA bath for few minutes and finally dried under air laminar flow.

LiNbO$_3$ is known to be slowly attacked by HF solution [8], which is the reason why the SiO$_2$ layer is removed from the backside of the membranes, while Al is still protecting the top side of the chip. However, the opacity of the metal layer prevents the monitoring of SiO$_2$ etching during the HF step. Hence, we choose to apply an etching time slightly longer (45 sec) than the estimated one, in order to make sure of complete SiO$_2$ removal. This result into 5 to 10 µm undercut, visible as a yellow frame around the released membranes, shown in Figure 2.31.

As will be discussed in the next section, full removal of SiO$_2$ from the membrane backside is crucial for optimal device performance.
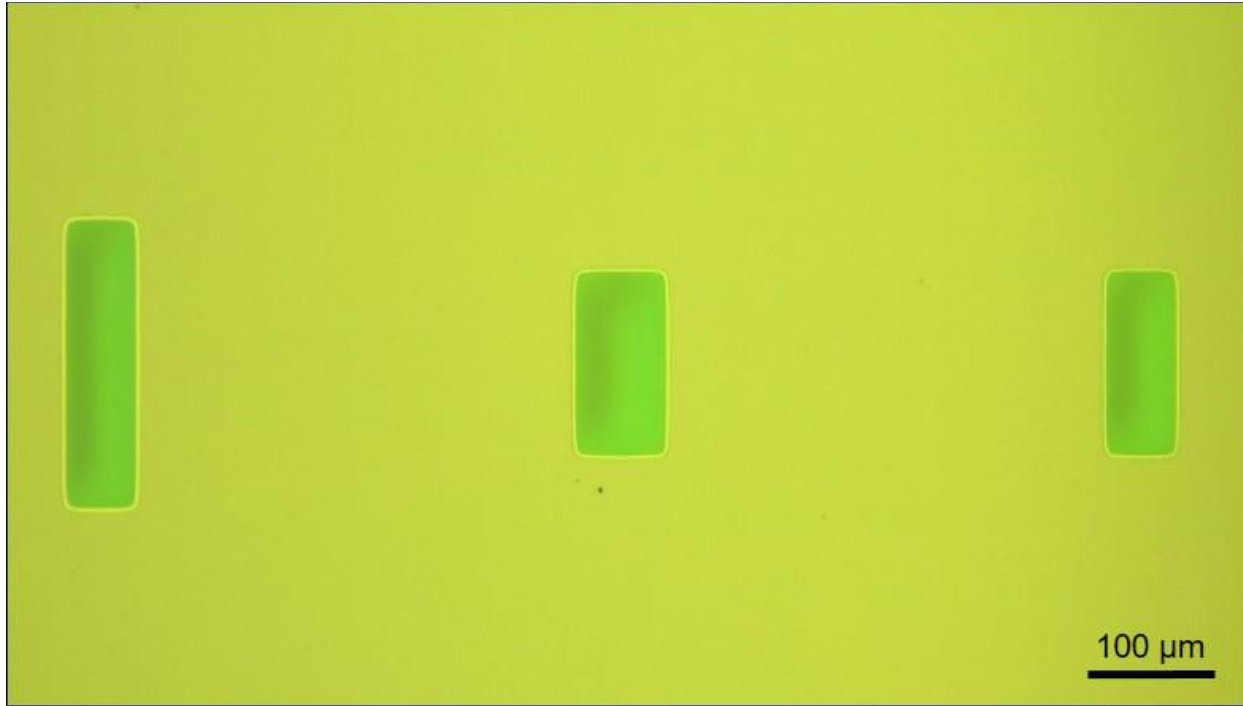
Figure 2.31: Optical image of fabricated LiNbO3 suspended membranes of three different dimensions.

Interdigitated Electrodes (IDT):

The second step of the process flow involves the liftoff of metal electrodes on top of LiNbO$_3$ membranes. Electron beam (E-beam) lithography is chosen over optical lithography due to the sub-micron dimensions of electrode fingers (500 nm wide). First, the chip is thoroughly cleaned with acetone and IPA followed by 5 min of thermalization at 180°C in order to evaporate any residual solvent. Two positive tone resists such as PMMA and MMA are used for the liftoff by first spin coating a 200 nm-thick layer of MMA and then a 100 nm-thick layer of PMMA. Each layer is hard baked at 180°C for 5 min. MMA develops faster than PMMA and hence it provides an undercut that is necessary for the successful liftoff process.
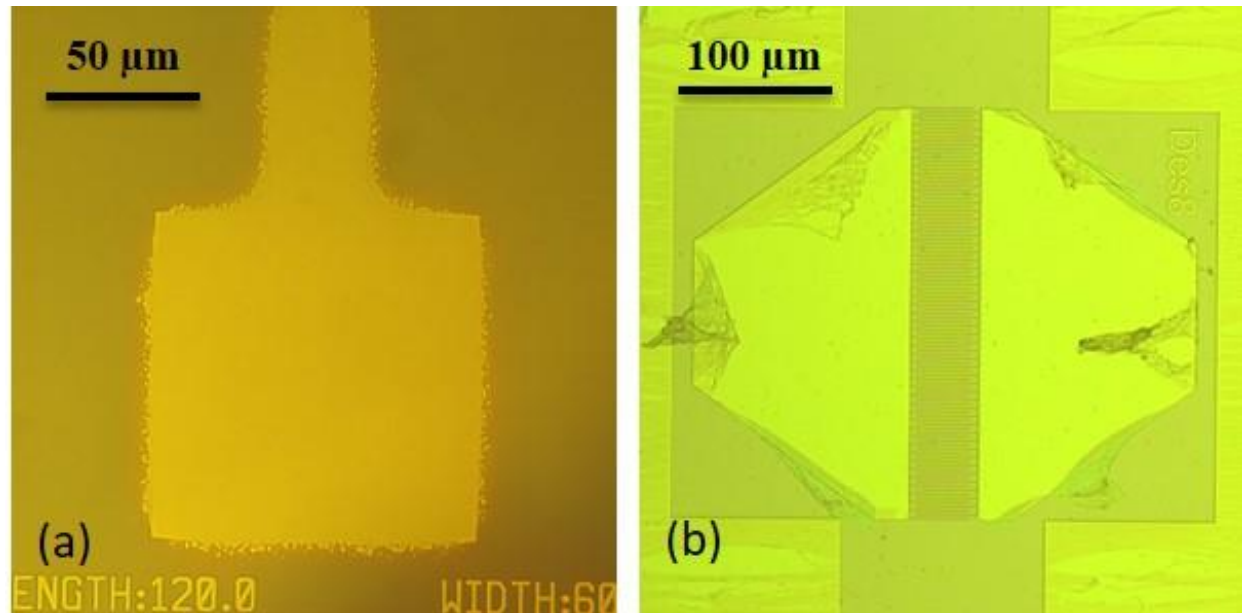
Figure 2.32: Optical image after development phase showing (a) the melting of E-beam resist due to grounding effect and (b) residues of Electra 92.

Electrical grounding of the chip during the E-beam writing phase is essential, in order to prevent the resist from melting due to the high energy electrons coming from the electron gun, as shown in Figure 2.32a. A 100keV electron gun is used to expose the resist and such high energy electrons can be grounded by providing an electrical connection either through the substrate or by coating a conductive polymer on top of the resist.
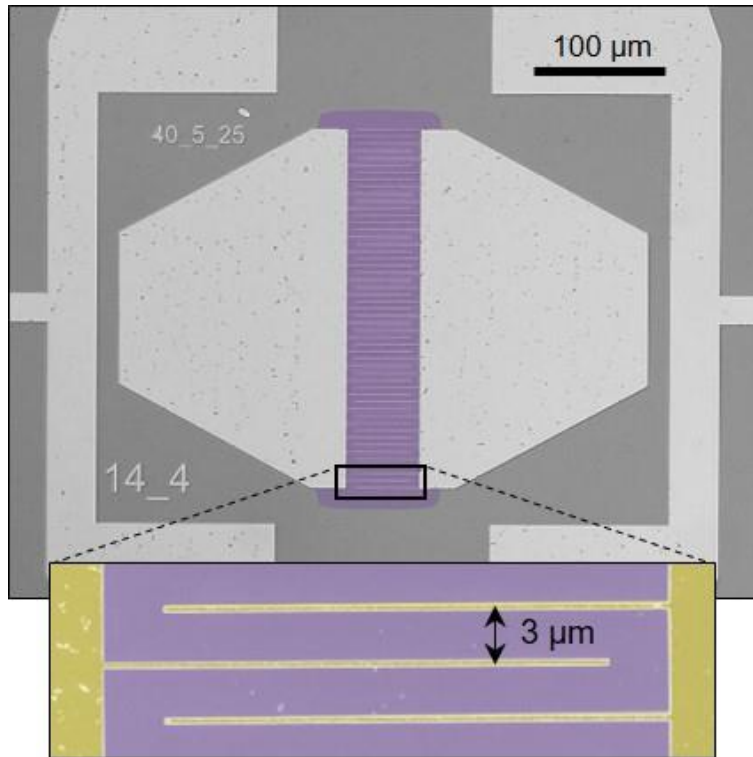
Figure 2.33: SEM image of an 80 x 270 μm LiNbO$_3$ membrane (purple color), with 25 pairs of Al electrodes. The inset shows a zoom-in on Al fingers, colored in yellow, 500 nm wide and with 3 μm pitch.

LiNbO$_3$ is a dielectric material that makes it difficult for the charges to be grounded via substrate. For this purpose, a 40 nm-thick layer of conductive polymer (Electra 92 from ALLRESIST GmbH) is spin-coated on top of both resists, while a copper tape is used to provide an electrical connection between the ground and the top surface of the chip. Electra 92 is a hydro-soluble polymer that can easily be removed after exposure by washing the chip for 1 min with DI water. However, residues of Electra 92 are observed when the substrate is exposed with insufficient dose, as shown in Figure 2.32b. An exposure dose test is carried out in order to find the best exposure parameters that yield accurate dimensions with no residues of Electra 92. Gun spot size of 50 nm is used to write fingers with exposure dose of 450 μC/cm^2 whereas pads are written with 100 nm spot size and exposure dose of 700 μC/cm^2.

Resists are developed for 1 min in MiBK:IPA 1:3 solution followed by rinsing with IPA. 100 nm of Al is evaporated and liftoff is successfully performed by leaving the chip in an acetone beaker for one day. Figure 2.33 shows a scanning electron microscope (SEM) image of the bulk acoustic resonator with 25 pairs of IDT on top of an 80 μm wide LiNbO$_3$ membrane.

Experimental Results

Fabricated devices are characterized to study their electromechanical performance, and compare them to finite element modeling (FEM) simulations. To do so, a Ground-Signal (GS) probe connected to a RF network analyzer (HP8719 from Keysight Technologies) is used to measure the devices in 1-port configuration. First, the measurement setup is calibrated with open, short and load standards. Then scattering (S_{11}) parameters of the devices are extracted and converted to admittance for assessing figures of microfabricated devices. The admittance data is fitted to the modified Butterworth-Van Dyke (mBVD) model in order to extract Q and k_t^2 [9, 10].
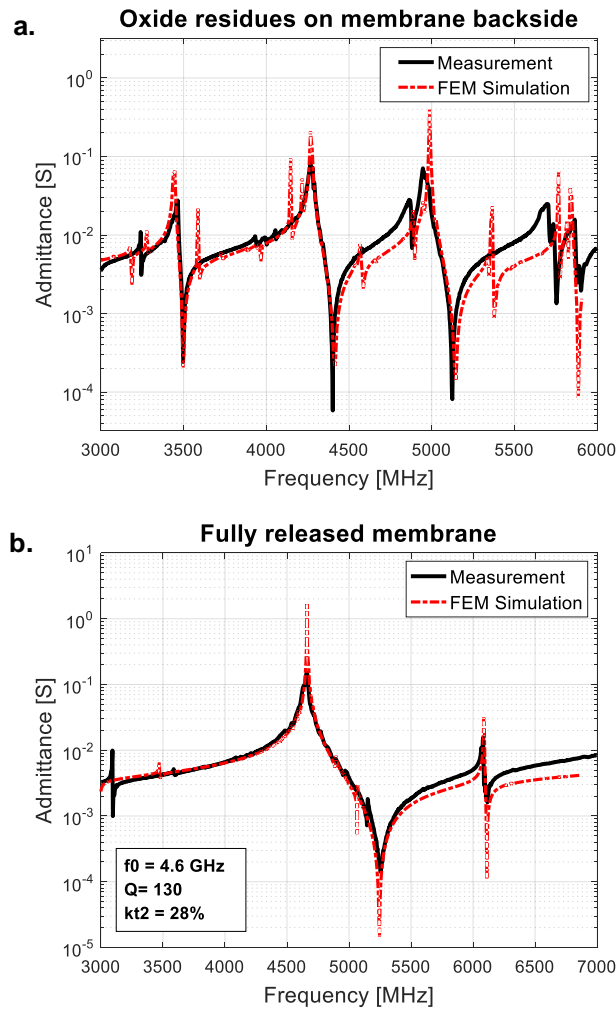
Figure 2.34: 1-port admittance curves of a 50 electrode pairs resonator before (a) and after (b) full removal of SiO_2 from the backside of $LiNbO_3$ membrane. As confirmed by FEM simulations, the complete removal of SiO_2 is a fundamental step of the fabrication process in order to avoid spurious modes around the resonance frequency of the device.

As shown in Figure 2.34, the complete removal of SiO$_2$ underneath LiNbO$_3$ membrane is critical. Oxide residues are the cause of unwanted spurious modes, as predicted by FEM simulations (Figure 2.34a). This prevents to recognize the actual device resonance frequency. Chips showing this kind of response need to undergo additional HF etching in order to fully clean the backside of the resonators membranes. However, as previously stated, HF also affects the PZE layer. Therefore, in this work we prefer to extend by few seconds the duration of the HF etching step, which results in fully released resonators membranes with 5 to 10 μm undercut. A clean admittance response is measured from a fully released resonator without residual oxide on the backside as shown in Figure 2.34b. k_t^2 of 28% and Q of 130 are measured at 4.6 GHz. The measured results are in agreement with FEM simulations, demonstrating successfully fabricated and functioning resonators.

Conclusion

This work illustrates the fabrication and characterization of LiNbO$_3$ bulk acoustic resonators that are readily suitable to be used as RF filters in 3-6 GHz range for 5G mobile networks. The fabricated device consists of a 400 nm-thick suspended Z-cut LiNbO$_3$ membrane with periodic pairs of interdigitated metal electrodes on top. Our experimental results show that complete removal of SiO$_2$ from the backside of membranes is essential in order to observe the true admittance response of the device. Fully released devices exhibit k_t^2 and Q up to 28% and 300, respectively, for frequencies around 5 GHz. This performance is in agreement with FEM simulations and is suitable for next generation RF-filter technology.

References

[1]   Ruppel, C.C.W., Acoustic Wave Filter Technology - A Review. IEEE Transactions on Ultrasonics, Ferroelectrics, and Frequency Control, 2017. 64(9): p. 1390-1400.

[2]   Takai, T., et al.: 'I.H.P. SAW technology and its application to microacoustic components (invited)'. IEEE Int. Ultrasonics Symp.(IUS), Washington, DC, September 2017, pp. 1–8.

[3]   S. Härmä and V. P. Plessky, Surface Acoustic Wave RFID Tags, in Development and Implementation of RFID Technology, 2009. DOI: 10.5772/6522.

[4]   Plessky, V., et al., 5 GHz laterally-excited bulk-wave resonators (XBARs) based on thin platelets of lithium niobate. Electronics Letters, 2018.

[5]   Weis, R. S., e T. K. Gaylord. «Lithium Niobate: Summary of Physical Properties and Crystal Structure». *Applied Physics A* 37, n. 4 (1985): 191–203. https://doi.org/10.1007/BF00614817.

[6]   Kuznetsova, I. E., B. D. Zaitsev, S. G. Joshi, e I. A. Borodina. «Investigation of acoustic waves in thin plates of lithium niobate and lithium tantalate». IEEE Transactions on Ultrasonics, Ferroelectrics, and Frequency Control 48, n. 1 (2001): 322–28. https://doi.org/10.1109/58.896145.

[7]   NanoLN: 'LN   thin   film   on   insulator'.   Available   at http://www.nanoln.com/en/pinfo.asp?ArticleID=32, accessed September 2018.

[8]   Sones, C.L., et al., Differential etch rates in z-cut LiNbO3 for variable HF/HNO3 concentrations. Journal of Materials Chemistry, 2002. 12(2): p. 295-298.

[9]   Schmid, S., L.G. Villanueva, and M.L. Roukes, Fundamentals of Nanomechanical Resonators. 2016: Springer International Publishing.

[10]   R.C. Ruby et al, Modified Butterworth-Van Dyke circuit for FBAR resonators and automated measurement system, IEEE Ultrasonics Symposium. Proceedings. An International Symposium, 2000. 1: p. 863-868.

2.3.2   Supplementary information

The process flow presented in the publication 'Fabrication of Lithium Niobate Bulk Acoustic Resonator for 5G Filters' involves the fabrication of membranes in LN layer by etching deep cavities in Si substrate from the backside of the chip using Bosch process followed by patterning of electrodes using E-beam lithography on top of the suspended membranes. Depending on the design of the devices and number of electrode pairs, membranes of different sizes are fabricated. Upon release, the bigger membranes are more fragile and prone to collapse than the smaller ones as the membranes are only 400 nm thick (Figure 2.35a). The membranes broken during the release process give rise to certain fabrication challenges for the patterning of electrodes. The broken membranes act as holes on the surface of the chip and cause E-beam resist to seep out during the coating of the resist. Secondly, a vacuum is created underneath which holds the chip on the chuck of the coater during spin coating of the resist and the broken membranes hinder in achieving the required pressure. It is also observed that some membranes can be broken by the pressure of the vacuum pump, which also accelerates the flow of the resist through the broken membranes. This leads to the uneven coating of resist on the areas around the broken membranes and results in the underexposure or overexposure of the electrodes (Figure 2.35b). Furthermore, the buckling of membranes after release can also obstruct in achieving good patterning of the electrodes, as shown in Figure 2.36.

In order to solve the above-mentioned fabrication challenges, a second generation of process flow is developed that first involves the patterning of electrodes and then making the membranes in LN layer, as it avoids the breakage and buckling of the membranes during the resist coating step. The release process includes etching small holes from the front side in the metal and LN layer around the electrodes followed by isotropic etching of Si using SF_6 gas to make a deep cavity underneath the device, as shown in Figure 2.37.
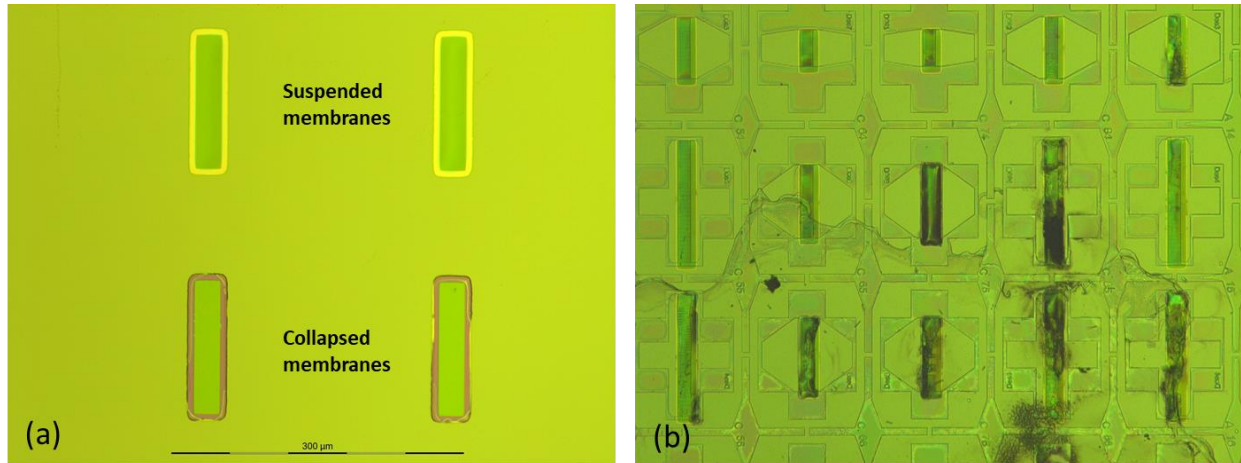
Figure 2.35: (a) Optical image showing 150 μm by 80 μm membranes in LN after the release process. Larger membranes are more vulnerable to collapse than the smaller membranes during release. As the membranes are 400 nm thick, a slight mishandling could lead to the membrane collapse. (b) Optical image after the pattering of electrodes on top of the suspended membranes. During the resist coating phase, the broken membranes act as holes on the surface of the chip and lead to the resist seeping through the holes due to the pressure created by the vacuum to hold the chip on the chuck of the coater. This results in an uneven coating of the resist on the areas around the broken membranes. E-beam writing is very sensitive to the variation in the resist thickness and results in the underexposure or overexposure of the electrodes.
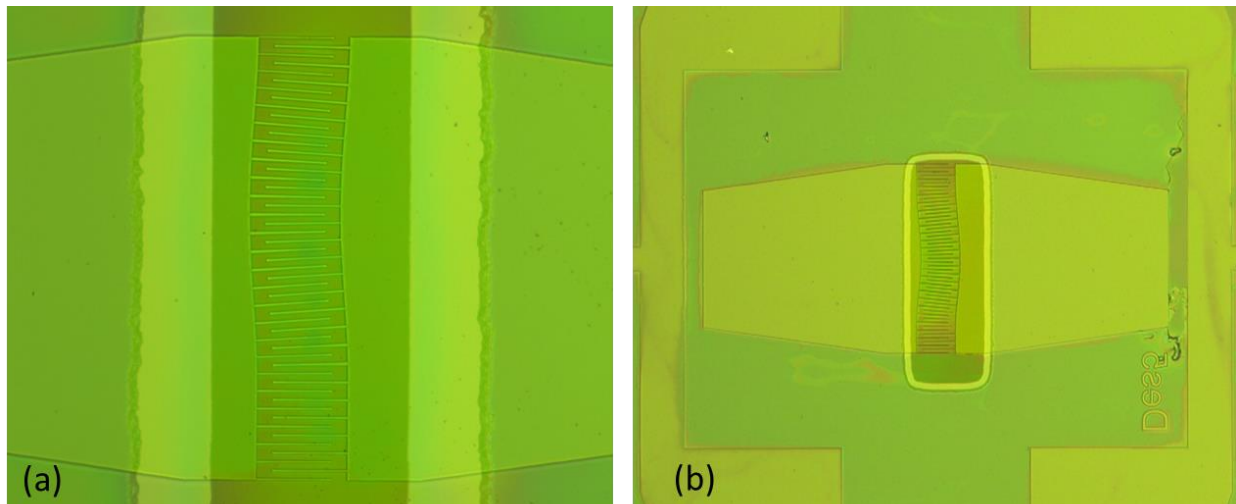
Figure 2.36: The fabrication process flow involves the making of membranes first followed by patterning of electrodes on top of the suspended membranes. It is observed that the electrodes are not well written on the membranes that are buckling, as shown in the optical images (a) - (b).

94
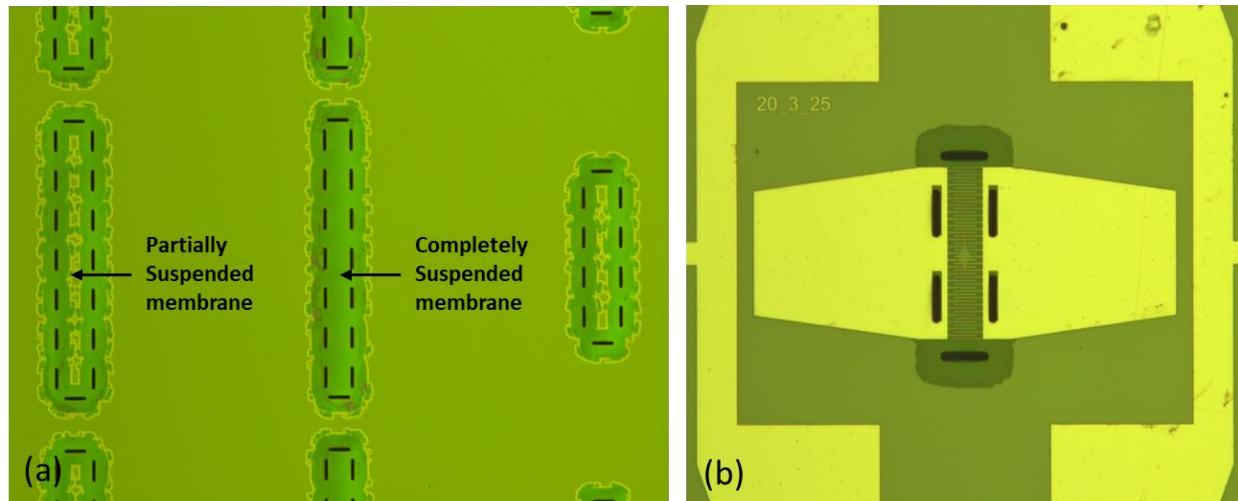
Figure 2.37: (a) Optical image showing the release of the test structures from the top side in order to solve the problems of membrane breakage and buckling during the electrode patterning stage. Instead of making the membranes first and then patterning the electrodes on top of the suspending membrane, the electrodes are patterned first and then the membranes are created by etching holes on the sides of the device and doing isotropic dry etching of Si using SF_6 gas in Reactive Ion Etcher (RIE). (b) Optical image shows the releasing of the device from the front side by etching holes in the metal and LN layer followed by isotropic etching of Si cavity underneath the device.

3 Low Phase Noise Oscillator Based on Lithium Niobate Shear Mode Resonator

3.1 Introduction

The hyper-connected world of 21st century requires billions of battery-powered devices communicating and transferring data at high speed for the smooth functioning of the society. The demand for a miniature, high performance and single-chip Radio Frequency Front End (RFFE) for next-generation wireless communication is rapidly growing. Therefore, the use of MEMS-based components for filtering and timing control with ultralow power consumption and smaller form factor can revolutionize the architecture of modern RFFE [1][2].

A stable and low noise frequency synthesizer is a key component of an RF transceiver that enables signal modulation and system synchronization. In order to achieve a precise frequency source, one must use a high Q resonator (typically mechanical) in a closed feedback loop of a self-sustained oscillator circuit. The natural frequency of the resonator determines the output frequency of the oscillator. The most common type of oscillator uses quartz crystal resonators due to their high Q and superior thermal stability [3][4]. However, quartz crystal resonators are hardly tunable, and their resonance frequency is limited to few tens of MHz, given the typical thickness of quartz substrates. Therefore, it cannot address the needs of present communication bands without requiring additional circuitry for frequency up-conversion [5]. To do this, the typical approach is based on using a Phase Locked Loop (PLL) coupled to a voltage controlled oscillator (VCO), a phase detector and a frequency divider. When PLL is used as a frequency synthesizer, the output frequency of the oscillator circuit is divided by the factor N and compared with the reference frequency of the quartz resonator (f_{ref}) using a feedback loop. Phase detector compares both the frequencies and adjusts the voltage of VCO circuit in order to lock the loop. Once the loop is locked, the VCO generates a frequency (f_o) which is N times higher than the reference frequency of quartz resonator ($f_o = N \times f_{ref}$) [6]. Although quartz based oscillator coupled with PLL is the gold standard for frequency synthesizers, the introduction of the PLL increases the overall footprint, cost and power consumption of the RFFE.

An oscillator employing a MEMS resonator for frequency synthesis and control is attractive for next generation of RFFE due to its small form factor, low power consumption and monolithic integration with the onboard circuitry [7][8]. MEMS resonators can easily operates in high frequency bands (< 3 GHz) thus

providing an alternative solution to the bulky quartz-based oscillator and removing the power hungry PLL for operation at high frequencies [9].

Among the different RF MEMS resonators, Surface Acoustic Wave resonators (SAW) and Bulk acoustic wave resonators (BAW) have stood the test of time for filtering and time referencing in RF frontends. However, Laterally Vibrating Resonators (LVR) are an emerging class of MEMS resonators combining the benefits of SAW and BAW resonators by enabling multi-frequency devices on the same wafer while offering high system integration and frequency scalability [10][11].

LVR based oscillators have been demonstrated with, but are not limited to, Aluminum Nitride (AlN), Aluminum Scandium Nitride (AlScN) and Lithium Niobate technology [12]–[16]. AlN resonators offer high quality factor (Q) but suffer from low electromechanical efficiency ($k_t^2 < 3\%$), whereas AlScN resonators demonstrate a relatively higher k_t^2 at the expense of a reduced Q [14][17]. On the other hand, LN resonators exhibit superior piezoelectric response as compared with AlN and AlScN resonators resulting in $k_t^2 \geq 40\%$ while maintaining a high Q [18]. This make LN resonators a suitable candidate for MEMS based oscillators as their large k_t^2 permits wide frequency tunability, and the high Q ensures low phase noise (PN) performance.

Some groups have demonstrated reconfigurable oscillators exploiting the high k_t^2 of LN resonators by either artificially shifting the resonance frequency of the resonator or using multiple overtones to lock the oscillation frequency [19]–[21]. Voltage controlled frequency synthesis using LN resonator has been done by using high Q varactor in series with the resonator in the oscillator loop providing frequency tunability of 1.4% for the resonance frequency of 180 MHz [19]. Similarly, multi-resonances of LN based lateral overtone bulk acoustic resonator (LOBAR) has been used to switch the oscillation frequency over the wide range of 300 MHz to 500 MHz while maintaining ultra-low power and PN performance [22].

This work demonstrates the development of a MEMS oscillator using a LN shear horizontal mode (SH0) resonator around 300 MHz. Our resonators are fabricated on 400 nm thick X-cut LN and exhibit k_t^2 up to 40% and Q up to 3000, surpassing the performance of state-of-the-art SH0 mode resonators. We use off-the-shelf, discrete components such as an amplifier, phase shifter and attenuator along with a resonator to build the oscillator circuit. We study the influence of the resonator's k_t^2 and Q on the PN of the oscillator and show the famous relation between PN and Q as estimated by Leeson's model. Furthermore, we also illustrate the impact of carrier power (amplifier supply power) on PN of the oscillator with the resonator operating in the nonlinear region.

3.2   Resonator overview

In this work, we fabricate 2-port resonators consisting of a suspended plate of X-cut LN with Interdigitated (IDT) aluminum (Al) electrodes on the top. The IDTs connected to the alternating potential generate E-field in the piezoelectric material. The transduction in the resonator's cavity gives rise to acoustic standing waves in the longitudinal and transverse direction, exciting different modes such as Symmetric (S), Shear Horizontal (SH), and Asymmetric (A). Depending on the LN cut and planar device orientation, some modes are excited with larger k_t^2 while some modes are suppressed. The SH0 mode is excited by orienting devices at 170° to +y-axis of the X-cut LN as it ensures the largest possible k_t^2 for the intended mode [23]. The resonance frequency (f_s) is set by the IDT pitch (W_p) and the length of the resonator (L) is given as:

$$f_s = v \times \sqrt{\left(\frac{1}{2W_p}\right)^2 + \left(\frac{1}{2L}\right)^2} \approx \frac{v}{2W_p} \tag{3.1}$$

where v is the acoustic phase velocity of the excited mode. The detailed description of the design, fabrication and characterization of LN based resonators (S0 and SH0) has been presented in our previous work [18][24].
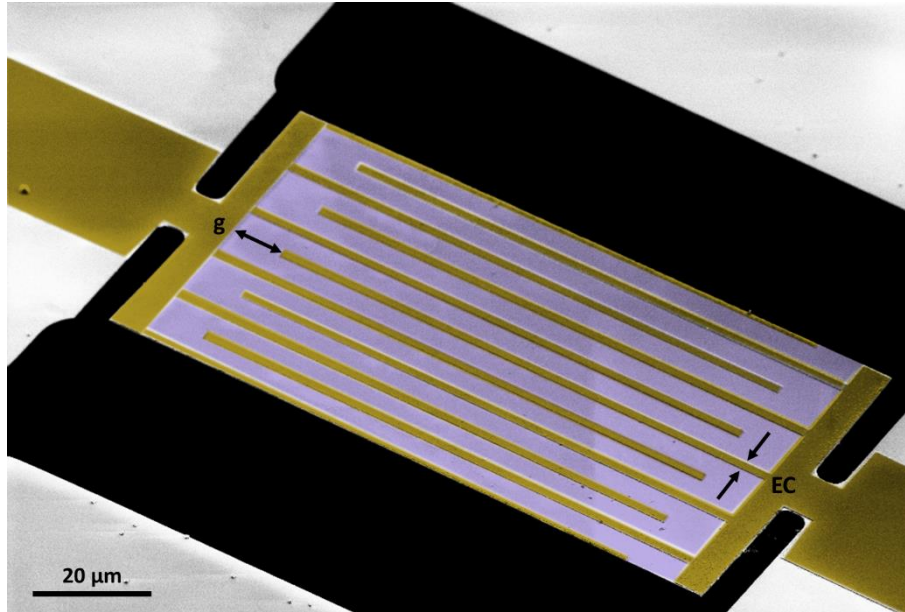
Figure 3.1: SEM image of the fully released 2-port LN based SH0 mode resonator with Al electrodes.

Figure 3.1 shows the SEM image of the fabricated LN based SH0 mode resonator achieved using a 3-mask process flow. The fabrication is done on 400 nm thick X-cut LN on top of the HR silicon (Si) substrate provided by NGK insulators. The first step of the process flow involves the liftoff of 100 nm thick Al electrodes on top of LN. The second step requires the etching of LN using chromium (Cr) as the hard mask since it helps to achieve straight side walls. LN is etched in Reactive Ion etcher (RIE) using CHF$_3$/Ar gases. E-beam lithography is used for writing both of the mask layers as it provides an excellent alignment accuracy between the layers. The last step of the process flow involves suspending the devices by etching deep cavities in Si substrate underneath the devices. It can be achieved by making openings on the sides of the resonators and etching Si isotopically in RIE using SF$_6$ gas.

The resonators are characterized in 2-port configuration using two ground-signal-ground (GSG) probes connected to a Vector Network Analyzer (HP8719D). The VNA is used to record S-parameters for calculating k_t^2 and Q as:

$$k_t^2 = \frac{\pi^2}{4} \times \frac{f_p - f_s}{f_p} \tag{3.2}$$

$$Q = \frac{f_s}{\Delta f_{3dB}} \tag{3.3}$$

where f_s is the resonance and f_p is the anti-resonance frequency of the resonator with Δf_{3dB} being the 3dB bandwidth at f_s.

To study the influence of k_t^2 and Q of the resonator on the performance of the oscillator, two geometrical parameters are swept: width of the electrodes and finger-to-bus gap. By changing these parameters, we achieve devices with a wide range of k_t^2 (30-40%) and Q (1000-3000). The electrode coverage (EC) or duty factor is the width of the electrode fingers relative to the pitch. Figure 3.2 shows the effect of variation in EC on k_t^2 and Q of the resonator. k_t^2 drops 25% in going from 20% to 70% EC with little influence on Q. Similarly, the change in gap (g) significantly affects Q while maintaining a steady value for k_t^2. Figure 3.3 illustrates the devices with a variety of Qs for different values of g with the maximum Q of 3200 at $g = \lambda$ and the constant k_t^2 for all the devices.
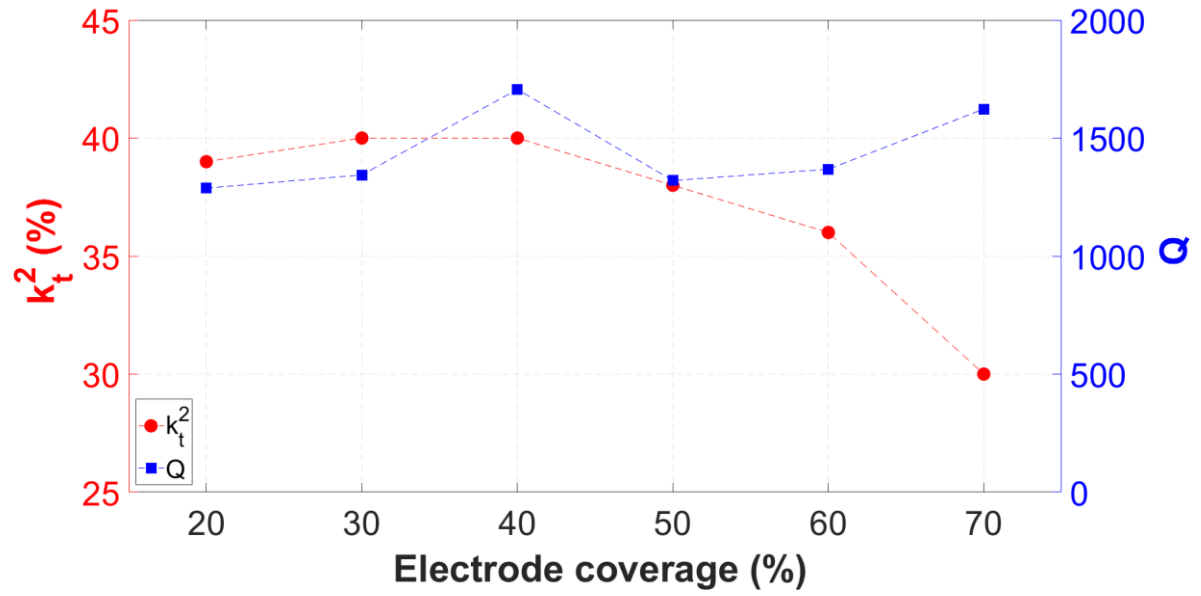
Figure 3.2: Effect of EC on k_t^2 and Q of the SH0 mode resonator. k_t^2 remains almost constant for the smaller electrode coverages (20% to 40%) whereas it starts to go down for higher electrode coverages with the drop of 25% for the EC of 70%. On the other hand, Q does not show a significant dependence on EC as it fluctuates around 1500 for different electrode coverages. Each data point is the average of three devices.
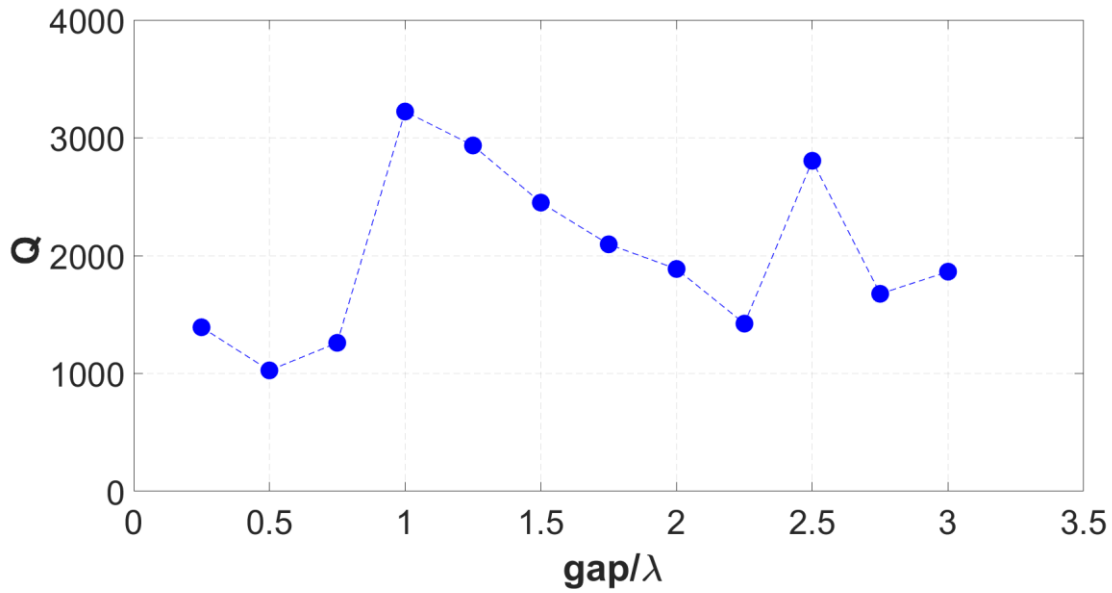
Figure 3.3: Effect of finger-to-bus gap (g) on Q of the resonator. For different values of g, wide range of Qs are achieved with the peak at 3200 for $g = \lambda$. Each data point is the average of three devices.

3.3 Experimental setup

For the oscillator, we used off-the-shelf amplifier (AU-1442, L3 Narda-Miteq), phase shift (SO-06-411, Pulsar), coupler and attenuator in a closed feedback loop with the fabricated 2-port SH0 mode resonator (Figure 3.4). The purpose of amplifier and phase shifter is to fulfill the Barkhausen conditions which state that for the sustained oscillations, the closed-loop gain should be equal to 1 and the closed-loop phase should be equal to 0 at the frequency of oscillation [25]. The amplifier provides the required gain to overcome the insertion loss of different components including the wire losses. As the amplitude approaches the desired level, it saturates and stabilizes the loop gain to 1. Phase shifter satisfies the second condition by setting the loop phase equal to 0 and subsequently, the oscillation frequency as close to the resonance frequency of the resonator. Attenuator is used to ensure the constant input power of -10 dBm to the resonator, guaranteeing operation in the linear region. SH0 mode resonator is used as the frequency setting element in the circuit. Instead of mounting the chip on the PCB and using wire bonding to connect the resonator with the rest of the circuit, we used two GSG RF probes to connect the resonator and close the loop. Wafer or chip level probing of resonators in the oscillator loop helps to reduce the time of measurement per device. A 20 dB coupler is used to couple the oscillation signal to the PN analyzer for determining the performance of the oscillator. This experimental setup is similar to one presented in our group's previous work for the AlN and AlScN oscillators [15].
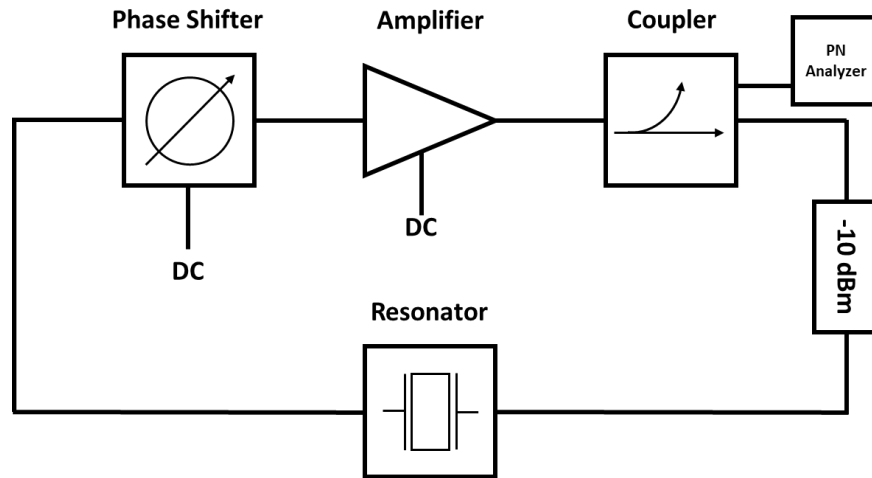
Figure 3.4: Block diagram of the oscillator circuit consisting of a phase shifter and an amplifier to sustain the oscillations along with the resonator for frequency control. An attenuator is used to avoid non-linear operation of the resonator. PN analyzer is connected to the loop via a 20 dB coupler to evaluate the performance of the oscillator.

3.4 Results

PN is the key parameter in characterizing the noise performance of the oscillator as it directly corresponds to its frequency stability. PN is measured in dBc/Hz (decibel relative to the carrier level per hertz) and can be described by the Leeson's equation as [26]:

$$L(f_m) = 10\log\left[\frac{1}{2}\left(\left(\frac{f_o}{2Qf_m}\right)^2 + 1\right)\left(\frac{f_c}{f_m} + 1\right)\left(\frac{Fk_bT}{P_S}\right)\right]$$

(3.4)

where f_o is the carrier frequency, f_m is the offset frequency, f_c is the corner frequency, F is the noise factor of the amplifier, k_b is the Boltzmann constant, T is absolute temperature in Kelvin and P_s is the power at the input of the amplifier.

We used an E5052A Signal Source Analyzer (SSA) to measure the PN for 60 oscillators using different SH0 mode resonators at the offset frequency of 1 kHz, 10 kHz and 1 MHz from the carrier frequency. When the Barkhausen conditions are met, the SSA automatically locks at the carrier frequency of the oscillator loop which may not be the resonance frequency of the resonator. However, we have noticed that the lowest PN is achieved when the carrier frequency matches with the resonance frequency due to the minimum insertion loss offered by the resonator resulting in the increase in carrier power. We use phase shifter to tune the phase in the loop and shift the carrier frequency as close as possible to the resonance frequency of the resonator, as shown in Figure 3.5. By tuning the carrier frequency, we gained 20 dB improvement in PN over the tuning range of 1 MHz.
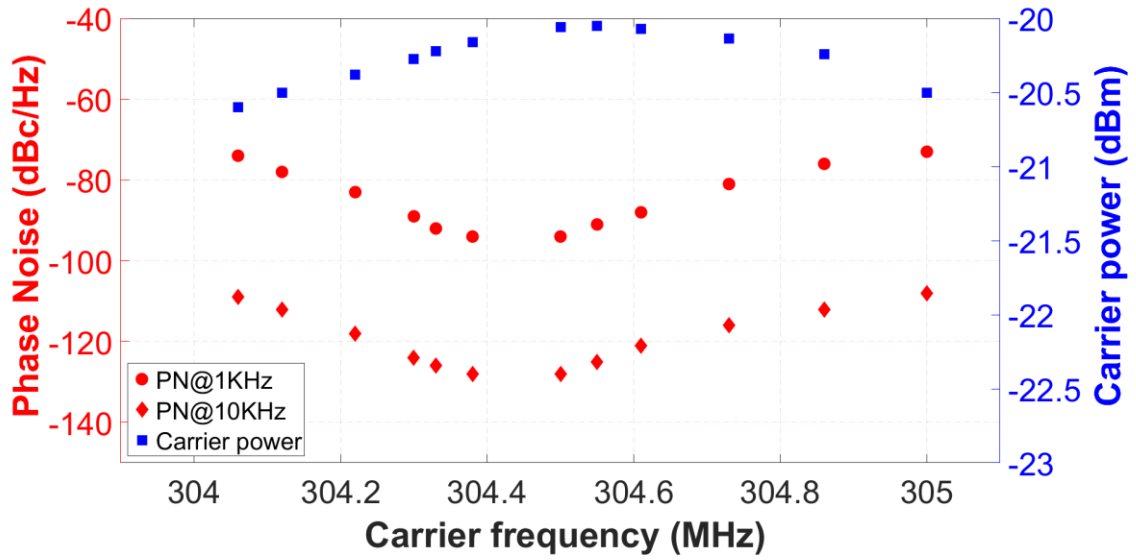
Figure 3.5: Tuning of carrier frequency using phase shifter to get the lowest PN. At the point of lowest PN, the carrier power gets maximized to indicate the matching of oscillation and resonance frequencies. Red circle and diamond points represent PN at an offset of 1 kHz and 10 kHz, respectively.
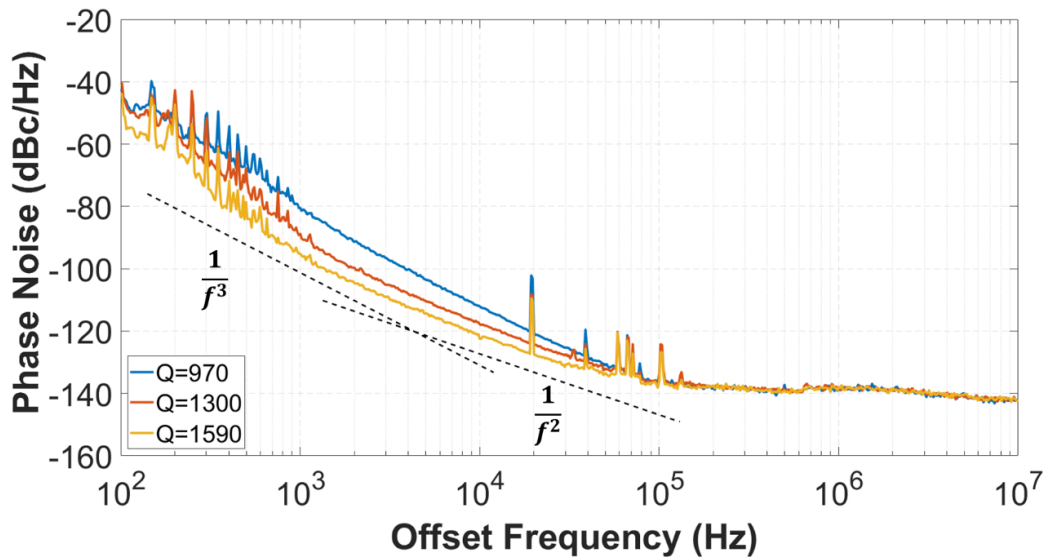
Figure 3.6: PN as the function of offset frequency, measured for three different resonators having Qs of 970, 1300 and 1590. Lowest PN is achieved for the resonator having the highest Q (1590).

PN is mainly influenced by Q of the resonator and the carrier power (average power in the resonator), as indicated by the Leeson's equation. Figure 3.6 shows the measured PN from three different resonators having Qs of 970, 1300 and 1590. The resonators are chosen based on the relative difference of almost 20% in their Qs in order to demonstrate the effect of Q of the resonator on the PN of the oscillator. Among the three resonators, the lowest PN of -95 dBc/Hz and -123 dBc/Hz at the offset frequency of 1 kHz and 10 kHz, respectively, is achieved for the resonator with the highest Q of 1590. With the reduction of 20% and 40% in Q, the PN increases by almost 8% and 16% at the offset frequency of 1 kHz, and 5% and 10% at the offset frequency of 10 kHz, respectively. The resonators are measured at the same carrier power and at their resonance frequency in order to draw a fair comparison between the resonators of different Qs.
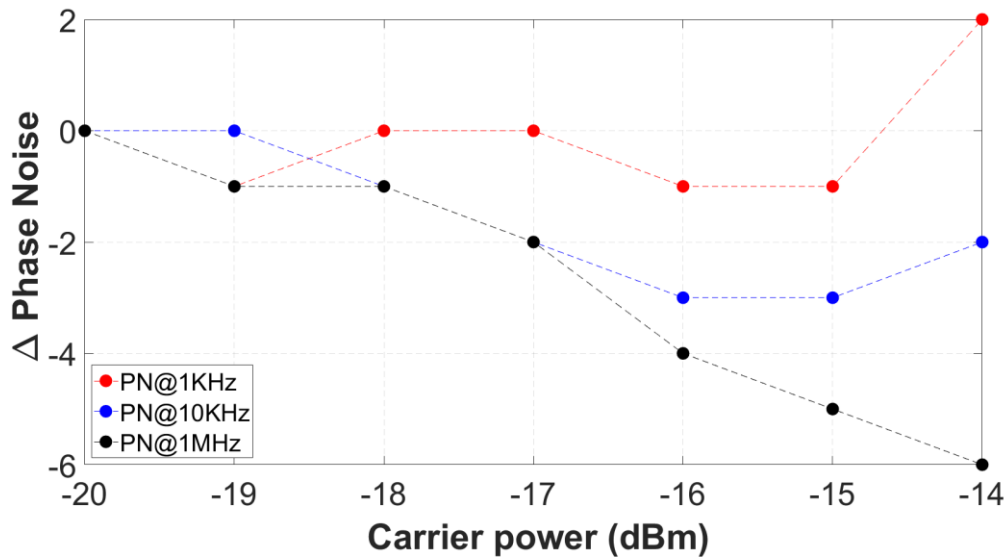
Figure 3.7: Change in PN as the function of carrier power from -20 dBm to -14 dBm. PN improves with the increasing carrier power for the resonator operating in the linear region. Carrier power higher than -15 dBm pushes the resonator towards the non-linearity leading to the increase in PN. PN at 1 MHz constantly reduces with the increasing carrier power.

All three measurements in Figure 3.6 are performed at -20 dBm carrier power. The reason to put this power is to stay below the point where the system shows nonlinear behavior. This is illustrated in Figure 3.7, where we show the change in PN at three different offset frequencies (1 kHz, 10 kHz and 1 MHz) for a particular oscillator for a range of carrier powers from -20 dBm to -14 dBm. The phase shifter operation

point is optimized for every single case to minimize PN. PN at 1 MHz offset matches very well the prediction, as it decreases linearly with increasing carrier power. This is expected since at that region (see Figure 3.6) we are in the noise floor of the system. At 10 kHz offset, we observe a dependence close to prediction up until -16 dBm carrier power, from where the PN increases. At 1 kHz offset, the PN remains approximately flat until it starts increasing at around -15 dBm. This marks -15 dBm the point where nonlinearity becomes detrimental for PN via amplitude-phase conversion [27]. For this reason, all the measurements we present from here onwards are taken at -20 dBm.

As mentioned in the previous section, we fabricate resonators with the varying electrode coverages to study the influence of k_t^2 of the resonator on the PN of the oscillator (Figure 3.2). Three sets of identical resonators having k_t^2 from the range of 30% to 40%, operating at resonance with the same carrier power, are used to measure the PN as shown in Figure 3.8. Importantly, we do not observe any change in PN for different k_t^2 in the resonator. This indicates that k_t^2 does not play any significant role in the noise performance of the oscillator, also indicated by Leeson's equation.
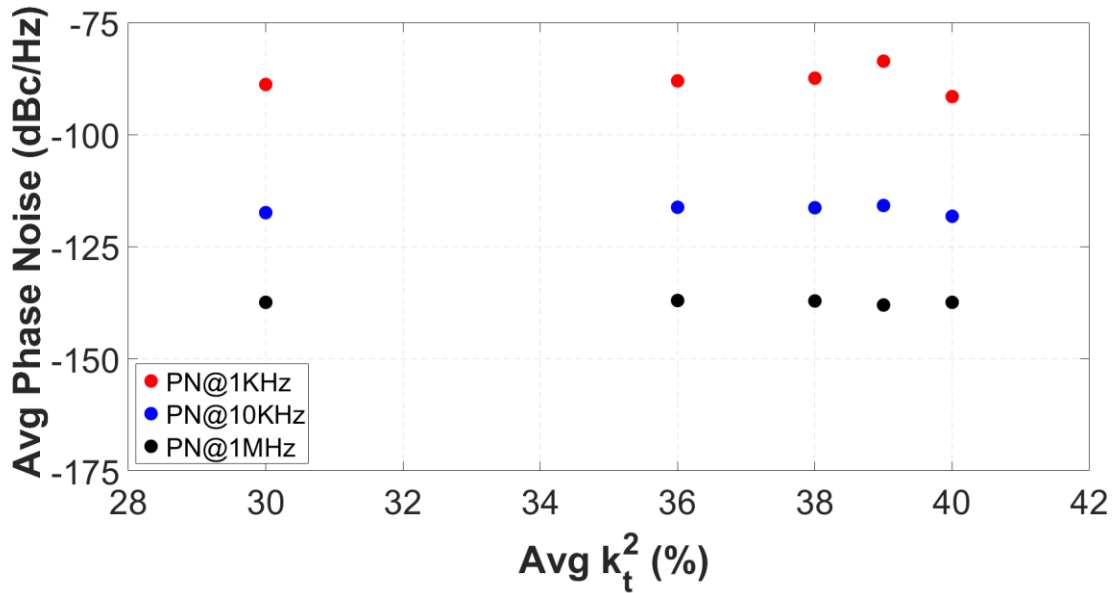
Figure 3.8: PN as the function of k_t^2 of the resonator at the offset frequency of 1 kHz, 10 kHz and 1 MHz. PN almost remains constant for the resonators having different k_t^2 indicating that PN of the oscillator is independent of resonator's k_t^2. Each data point is the average of three identical devices.

We also look at the dependence of the PN of the oscillator and Q of the resonator. Our sample of 35 different resonators with varying Q from 500 to 3000 and measured PN at the offset frequency of 1 kHz and 10 kHz while keeping all the measurement parameters constant (Figure 3.9). The data points are fitted to the power law function and the slope of line is compared with the theoretical value of Q^{-2}, predicted by the Leeson's equation. The measured PN at the offset frequency of 1 kHz and 10 kHz scales as $Q^{-2.43}$ and $Q^{-2.54}$, respectively, which deviates from the theoretical value. At this point, we do not know the reason for this deviation and further investigation needs to be done. Table 3.1 shows the comparison of PN performance from this work and from a selection of existing literature.
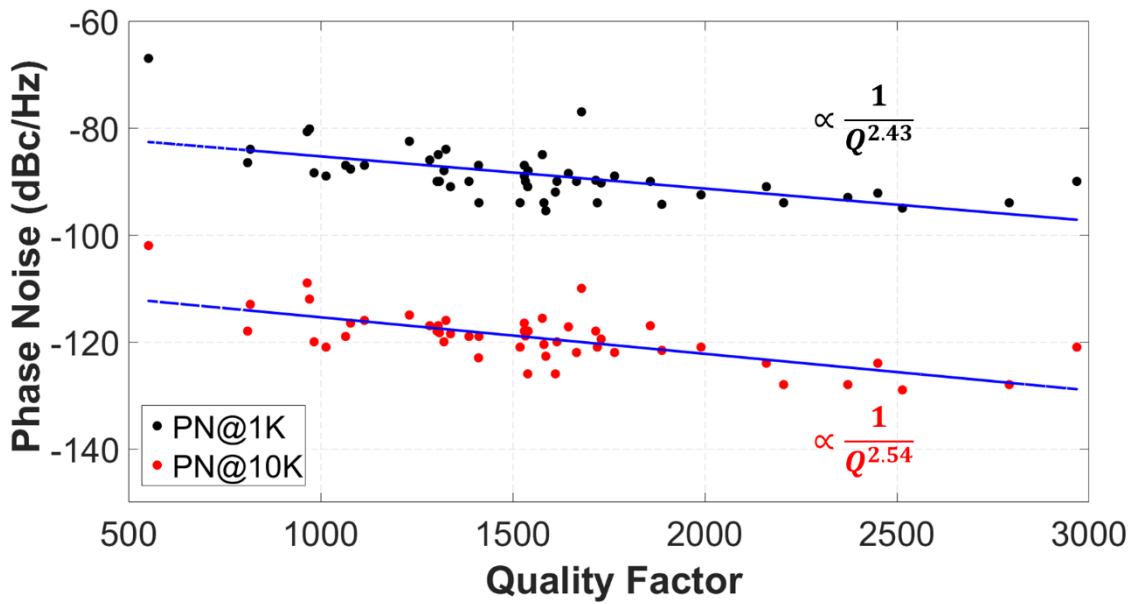
Figure 3.9: PN as the function of Q of the resonator at the offset frequency of 1 kHz and 10 kHz. The Qs are fitted to the power law function in order to extract the PN trend.

3.5 Conclusion

This work demonstrates the development of a MEMS oscillator based on a LN shear mode resonator operating at 300 MHz. We fabricate devices using our novel 3-mask process flow with the intention to achieve a wide range of k_t^2 and Q. For this purpose, we vary EC from 20% to 70% resulting in 25% change in k_t^2 from 40% to 30% with the steady Q of 1500. Moreover, we also sweep g from 0.25λ to 3λ, leading to resonators with Q from 500 to 3000.

We build our oscillator circuit using discrete components such as amplifier, phase shifter, coupler and attenuator along with the fabricated resonator in a close loop. We used RF probes to contact the resonator in the loop resulting in a faster measurement time as compared to the wire bonding technique. Furthermore, we also develop the measurement protocol in order to compare the PN obtained from different resonators. First, it is necessary to tune the oscillation frequency using phase shift as close as possible to the resonance frequency of the resonator as it offers minimum insertion loss and improves the PN. Secondly, the carrier power should be kept constant for all the measurements as a higher carrier power favors the resonator with the lower PN.

We demonstrate the influence of Q and carrier power on the PN and show that both improve the stability of the oscillator. For the Q of 2500, the measured PN of -96 dBc/Hz and -129 dBc/Hz at the offset frequency of 1 kHz and 10 kHz, respectively, is achieved which is 20% and 15% improvement in PN at the offset frequency of 1 kHz and 10 kHz, respectively, for the resonator with Q of 970. Similarly, the increasing carrier power reduces the PN of the oscillator as long it is operating in the linear regime. Lastly, we also study the influence of k_t^2 on the PN and conclude that PN is independent of the resonator's k_t^2 as it remained constant around -88 dBc/Hz and -117 dBc/Hz at the offset frequency of 1 kHz and 10 kHz, respectively, for the change in k_t^2 from 30% to 40%.

Table 3.1: PHASE NOISE PERFORMANCE COMPARISON of MEMS based oscillators

MEMS Resonators	Paper	Freq. (MHz)	PN 1 kHz (dBc/Hz)	PN 10 kHz (dBc/Hz)	Normalized Freq. (MHz)	PN 1 kHz (dBc/Hz)	PN 10 kHz (dBc/Hz)
AlScN LVR	[15]	193	-99	-123	500	-91	-115
AlN LVR	[15]	234	-91	-120	500	-84	-113
AlN LVR	[28]	1050	-91	-106	500	-97	-112
AlN LVR	[12]	222	-98	-130	500	-91	-123
AlN LVR	[7]	268	-94		500	-89	
LN LVR	[19]	178	-72		500	-63	
LN LVR	[29]	150	-84.4		500	-74	
LN LVR	This work	305	-96	-129	500	-92	-125

3.6 References

[1]   C. T. Nguyen, "Vibrating RF MEMS overview: applications to wireless communications," in *Micromachining and Microfabrication Process Technology X*, 2005, vol. 5715, p. 11.

[2]   G. Piazza, "Integrated aluminum nitride piezoelectric microelectromechanical system for radio front ends," *J. Vac. Sci. Technol. A Vacuum, Surfaces, Film.*, vol. 27, no. 4, pp. 776–784, Jul. 2009.

[3]   C. S. Lam, "A review of the recent development of mems and crystal oscillators and their impacts on the frequency control products industry," in *Proceedings - IEEE Ultrasonics Symposium*, 2008, pp. 694–704.

[4]   M. C. Chao, P. J. B. Lin, P. W. X. Lin, and J. Wang, "A perspective for the quartz crystal devices industry and technologies in Taiwan and China," in *IFCS 2014 - 2014 IEEE International Frequency Control Symposium, Proceedings*, 2014.

[5]   R. Thirunarayanan, D. Ruffieux, and C. Enz, "Reducing energy dissipation in ULP systems: PLL-Free FBAR-based fast startup transmitters," in *IEEE Transactions on Microwave Theory and Techniques*, 2015, vol. 63, no. 4, pp. 1110–1117.

[6]   V. M. Zackriya, J. Reuben, and H. M. Kittur, "A low power dual modulus prescaler for fractional-N PLL synthesizer," in *2014 International Conference on Electronics and Communication Systems, ICECS 2014*, 2014.

[7]   M. Rinaldi, C. Zuo, J. Van Der Spiegel, and G. Piazza, "Reconfigurable CMOS oscillator based on multifrequency AlN contour-mode MEMS resonators," *IEEE Trans. Electron Devices*, vol. 58, no. 5, pp. 1281–1286, May 2011.

[8]   J. T. M. Van Beek and R. Puers, "A review of MEMS oscillators for frequency reference and timing applications," *J. Micromechanics Microengineering*, vol. 22, no. 1, p. 35, Jan. 2012.

[9]   A. Kourani, Y. Yang, and S. Gong, "A Ku-Band Oscillator Utilizing Overtone Lithium Niobate RF-MEMS Resonator for 5G," *IEEE Microw. Wirel. Components Lett.*, vol. 30, no. 7, pp. 681–684, Jul. 2020.

[10]   S. Gong and G. Piazza, "Design and analysis of lithium-niobate-based high electromechanical coupling RF-MEMS resonators for wideband filtering," *IEEE Trans. Microw. Theory Tech.*, vol. 61, no. 1, pp. 403–414, 2013.

[11]   F. V. Pop, A. S. Kochhar, G. Vidal-Álvarez, and G. Piazza, "Laterally vibrating lithium niobate MEMS resonators with 30% electromechanical coupling coefficient," in *Proceedings of the IEEE International Conference on Micro Electro Mechanical Systems (MEMS)*, 2017, pp. 966–969.

[12]   C. Zuo, N. Sinha, J. Van Der Spiegel, and G. Piazza, "Multi-frequency pierce oscillators based on piezoelectric AlN contour-mode MEMS resonators," in *2008 IEEE International Frequency Control Symposium, FCS*, 2008, pp. 402–407.

[13]   A. Lozzi, M. Liffredo, E. T. T. Yen, J. Segovia-Fernandez, and L. G. Villanueva, "Phase Noise Measurements of Aluminum Scandium Nitride Oscillators," in *2019 20th International Conference on Solid-State Sensors, Actuators and Microsystems and Eurosensors XXXIII, TRANSDUCERS 2019 and EUROSENSORS XXXIII*, 2019, pp. 909–912.

[14]   M. H. Li, R. Lu, T. Manzaneque, and S. Gong, "Low Phase Noise RF Oscillators Based on Thin-Film Lithium Niobate Acoustic Delay Lines," *J. Microelectromechanical Syst.*, vol. 29, no. 2, pp. 129–131, Apr. 2020.

[15]   A. Lozzi, M. Liffredo, E. T. T. Yen, J. Segovia-Fernandez, and L. G. Villanueva, "Evidence of Smaller 1/F Noise in AlScN-Based Oscillators Compared to AlN-Based Oscillators," *J. Microelectromechanical Syst.*, 2020.

[16]   M. Rinaldi, C. Zuniga, B. Duick, and G. Piazza, "Use of a single multiplexed CMOS oscillator as direct frequency read-out for an array of eight AlN contour-mode NEMS resonant sensors," in *Proceedings of IEEE Sensors*, 2010, pp. 2666–2670.

[17]   A. Lozzi, E. Ting-Ta Yen, P. Muralt, and L. G. Villanueva, "Al0.83Sc0.17N Contour-Mode Resonators with Electromechanical Coupling in Excess of 4.5%," *IEEE Trans. Ultrason. Ferroelectr. Freq. Control*, vol. 66, no. 1, pp. 146–153, Jan. 2019.

[18]   M. Faizan and L. G. Villanueva, "Frequency-scalable fabrication process flow for lithium niobate based Lamb wave resonators," *J. Micromechanics Microengineering*, vol. 30, no. 1, p. 15008, Dec. 2020.

[19]   A. Kourani and S. Gong, "A Tunable Low-Power Oscillator Based on High-Q Lithium Niobate MEMS Resonators and 65-nm CMOS," in *IEEE Transactions on Microwave Theory and Techniques*, 2018, vol. 66, no. 12, pp. 5708–5723.

[20]   A. Kourani, R. Lu, T. Manzaneque, Y. Yang, A. Gao, and S. Gong, "A 175 MHz 72 µw Voltage Controlled Oscillator with 1.4% Tuning Range based on Lithium Niobate MEMS Resonator and 65 nm CMOS," in *IEEE MTT-S International Microwave Symposium Digest*, 2018, vol. 2018–June, pp. 567–570.

[21]   A. Kourani, R. Lu, and S. Gong, "A Wideband Oscillator Exploiting Multiple Resonances in Lithium Niobate MEMS Resonator," *IEEE Trans. Ultrason. Ferroelectr. Freq. Control*, vol. 67, no. 9, pp. 1854–1866, Sep. 2020.

[22]   A. Kourani, R. Lu, A. Gao, and S. Gong, "A 300-500 MHz Tunable Oscillator Exploiting Ten Overtones in Single Lithium Niobate Resonator," *IFCS/EFTF 2019 - Jt. Conf. IEEE Int. Freq. Control Symp. Eur. Freq. Time Forum, Proc.*, May 2019.

[23]   I. E. Kuznetsova, B. D. Zaitsev, S. G. Joshi, and I. a Borodina, "Investigation of acoustic waves in thin plates of lithium niobate and lithium tantalate.," *IEEE Trans. Ultrason. Ferroelectr. Freq. Control*, vol. 48, no. 1, pp. 322–328, 2001.

[24]   M. Faizan and L. G. Villanueva, "Optimization of Inactive Regions of Lithium Niobate Shear Mode Resonator for Quality Factor Enhancement (submitted)," *J. Microelectromechanical Syst.*, 2020.

[25]   F. He, R. Ribas, C. Lahuec, and M. Jézéquel, "Discussion on the general oscillation startup condition and the Barkhausen criterion," *Analog Integr. Circuits Signal Process.*, vol. 59, no. 2, pp. 215–221, May 2009.

[26]   E. Rubiola and V. Giordano, "On the 1/f frequency noise in ultra-stable quartz oscillators," in *Proceedings of the IEEE International Frequency Control Symposium and Exposition*, 2006, pp. 759–766.

[27]   L. G. Villanueva *et al.*, "Surpassing fundamental limits of oscillators using nonlinear resonators," *Phys. Rev. Lett.*, vol. 110, no. 17, Oct. 2012.

[28]   C. Zuo, J. Van Der Spiegel, and G. Piazza, "1.05-GHz CMOS oscillator based on lateral- field-excited piezoelectric AlN contour- mode MEMS resonators," in *IEEE Transactions on Ultrasonics, Ferroelectrics, and Frequency Control*, 2010, vol. 57, no. 1, pp. 82–87.

[29]   A. Kourani *et al.*, "A 150 MHz voltage controlled oscillator using lithium niobate RF-MEMS resonator," in *IEEE MTT-S International Microwave Symposium Digest*, 2017, pp. 1307–1310.

4 Conclusion and Outlook

4.1 Conclusion

This work focuses on the design, fabrication and characterization of high performance Lamb wave resonators on thin film LN for RF filters and oscillators. The research goals of the project are to (1) develop an in-depth understanding of electrical properties of LN material, choice of an appropriate material cut and in-plane device orientation to maximize the piezoelectric response of the intended modes, (2) develop a reliable and reproducible process flow for the fabrication of LN resonators with a high device yield, (3) improve the resonator k_t^2 by the design optimization of electrodes, (4) study the effect of inactive region of the resonator on the Q and subsequently improve Q by design modification and (5) build an oscillator circuit based on LN resonator and study the effect of k_t^2 and Q on phase noise (PN) of the oscillator.

The project started with the study of LN material where we developed Matlab codes for the matrix rotation using Euler angles to achieve material properties of different orientation cuts, followed by calculating K^2 for different modes in X-cut, Y-cut and Z-cut LN. The anisotropic nature of LN requires not only the selection of an appropriate crystal cut but also the correct in-plane orientation of the devices for maximizing K^2, as it is strongly influenced by both of the parameters. Interestingly, X-cut LN can produce both S0 and SH0 with the highest possible K^2 but with different device orientations. The highest K^2 for S0 and SH0 mode is achieved when the devices are oriented at 30° and 170° from +y axis, respectively. After the modelling of LN material, COMSOL is used to perform 2D and 3D FEM simulations of LN resonator to study the influence of different geometrical parameters such as electrode coverage, gap, bus and anchor on the k_t^2 and Q of the resonator.

Fabrication of LN resonators in the cleanroom is the most challenging part of the project as more than half of the duration of the PhD is focused on optimizing different fabrication processes in the cleanroom. We present a frequency scalable process flow using E-beam lithography for the fabrication of ultra-high frequency devices. The first step of the process flow involves the writing of Al electrodes on top of 400 nm thick X-cut LN with a buried 1 μm SiO_2 on HR Si substrate. The electrodes are deposited by evaporating a 100 nm thick layer of Al followed by liftoff. The second step requires the etching of LN using 150 nm thick Cr as a hard mask for achieving a straight side wall profile. Cr is etched in Ion Beam Etcher (IBE) followed by etching of LN layer using CHF_3/Ar gases with 50/100 sccm concentration in Reactive Ion Etcher (RIE). The final step of the process is the most crucial step as it involves suspending the devices that could

lead to the collapse from anchors. The release process includes the etching of openings on the sides of the devices in SiO$_2$ layer using C$_4$F$_8$ in RIE all the way to the Si substrate, followed by the isotropic etching of Si using SF$_6$ gas in RIE to make deep cavities underneath the devices. As the devices are released from the frontside of the chip, a 5 μm thick layer of photoresist should be used to protect the topside of the devices during the long dry etching of Si.

Frontside release comes with some fabrication challenges as it requires extra steps to protect the topside of the resonators during Si etching. Although the thick layer of photoresist provides the necessary protection but it is very difficult to remove it afterwards from the suspended structures without risking the breaking of devices. Additionally, the isotropic etching of Si gives an uncontrollable release area around the resonator where even a small variation in the width of the undercut drastically affects Q resulting in a non-predictable response of the resonator. For the second generation of process flow, we release the devices from the backside of the chip by making well-defined windows in Si substrate and etch all the way to the LN layer. We do so by using the front-back alignment technique of Mask-Less Aligner (MLA) laser writing tool to accurately align the backside windows with the devices on the frontside of the chip followed by Deep Reactive Ion Etching (DRIE) of Si using Bosch process to release the devices. Backside release process helps to achieve well-defined undercut resulting in a stable and reproducible Q. The developed process flow is used to fabricate S0 and SH0 mode resonators operating at 300 MHz and 500 MHz, respectively.

Our FEM simulations suggest a strong dependence of k_t^2 on the electrode coverage (EC) or duty factor of the electrodes which leads us to fabricate devices with varying electrode coverages from 20% to 70% for Al and Pt electrodes. For S0 mode resonator, our measurements suggest a constant value of k_t^2 around 30% for low electrode coverage from 20% to 40%, and a significant drop of 35% in k_t^2 for higher electrode coverages (> 40%). We also believe that the material of the electrodes does not affect k_t^2 as a similar trend is observed for devices with Al and Pt electrodes. However, it significantly affects the Q of the resonator as the resistivity of the metal contributes to the overall material losses. Devices with Al electrodes showed two times higher Q than the devices with Pt electrodes. We demonstrate devices with the highest reported k_t^2 of 31% and 40% for S0 and SH0 modes with Q of 720 and 590, respectively, in X-cut LN.

The next effort is done to optimize the Q of SH0 mode resonator by studying the influence of different inactive region elements such as gap, bus and anchor on the Q. We believe that a similar analysis can be applied for the S0 mode resonator. We fabricate devices by varying the dimensions of anchor, bus and

112

gap separately with the constant undercut of 0.5λ. By doing the anisotropic etching of Si from the backside of the chip, we have a constant width of the undercut for all the devices across the chip, thus minimizing the variation in Q due to the undercut. For the anchors, we sweep the width (W_a) from $\lambda/4$ to λ (in steps of $\lambda/4$) for the length (L_a) of $\lambda/2$ and $3\lambda/4$. We achieve the highest Q of 1400 for the anchors having the same W_a and L_a. For the bus and gap, we fabricate devices having a bus (W_b) equal to 0.3λ, 0.5λ and 0.75λ with the gap (g) swept from 0.5λ to 3λ in steps of 0.25λ, and a constant W_a and L_a of 0.75λ. The highest Q of 1900 is achieved for $g = 2\lambda$ and $W_b = 3\lambda/4$ with the k_t^2 of 41% resulting in the highest-ever achieved Figure-of-Merit (FoM) of 780 for SH0 mode resonators in X-cut LN.

For addressing the needs of 5G compatible filters, we fabricate an A1 mode resonator in Z-cut LN operating at 4.5 GHz. The design consists of 25 to 50 pairs of Al electrode fingers on top of 60 to 80 μm-wide LN membranes with fixed edges. The first step of the process flow consists of defining the openings on the backside of the chip for making membranes in LN layer. Bosch process is used to etch the Si all the way to the SiO₂ layer followed by wet etching of SiO₂ in HF solution. The second step involves the use of E-beam lithography to write the electrodes on top of the suspended LN membranes followed by liftoff of 100 nm thick Al electrodes. Our measurements suggest that complete removal of SiO₂ from underneath the membranes is essential for the spurious free response of the resonator. We demonstrate that fully released resonators exhibit k_t^2 and Q up to 28% and 300, respectively, for frequencies around 5 GHz. This performance is in agreement with the FEM simulations and is suitable for the next generation RF-filter technology.

Finally, we use our fabricated 2-port SH0 mode resonator to develop an oscillator circuit consisting of an amplifier, phase shifter, coupler and attenuator along with the resonator as a frequency setting element in the closed loop. We use RF probes to connect the resonator with the discrete components and measure phase noise (PN). PN is used to evaluate the noise performance of the oscillator as it directly relates to its frequency stability. We develop the measurement protocol to compare the PN obtained from different resonators. First, it is important to match the oscillator carrier frequency with the resonance frequency of the resonator using the phase shift to maximize the PN. Secondly, the carrier power should be kept constant for all the measurements as a higher carrier power favors the resonator with the lower PN. We also study the dependence of PN on Q and carrier power and show that both improve the PN of the oscillator as indicated by the Leeson equation. Moreover, we also demonstrate the influence of k_t^2 on PN and conclude that PN is independent of k_t^2 as it remains constant for the resonators with k_t^2 from 30% to

40%. Ultimately, we achieve an ultra-low phase noise of -96 dBc/Hz and -129 dBc/Hz, at the offset frequency of 1 kHz and 10 kHz, respectively, for the resonator with Q of 2500.

4.2   Outlook

Lamb wave resonators based on LN technology are famous for having a high k_t^2 that translates to a wider bandwidth for the filters. However, the large piezoelectric response of the LN material is a double-edged sword that not only excites the fundamental mode with high k_t^2 but also the spurious modes along with it. The presence of in-band and out-of-band spurious modes and higher order harmonics poses a serious challenge for their implementation in commercial applications. Minimizing spurious modes while maintaining high k_t^2 and Q of the intended mode is an active area of research and will remain the focus of future works.

Secondly, we believe that the k_t^2 of 30% and 41% for the S0 and SH0 modes, respectively, demonstrated in this work are the highest possible achievable values for k_t^2 in X-cut LN, and with the Qs up to 3000 are nonetheless impressive. However, we think that there is still room for improvement in Q by using a low resistive metal for the electrodes and further optimizing the inactive regions of the resonator. Some groups have shown significant improvement in Q by modelling the release area (undercut) around the resonator [1][2]. Most of this work has been done on AlN resonators but the same technique can be implemented on LN resonators to improve Q.

In this work, we investigate the highest possible k_t^2 for S0 and SH0 mode resonators in X, Y and Z cut of LN, and Z-cut for A1 mode resonator based on its k_t^2, though a higher k_t^2 has been demonstrated for A1 mode devices in Y-cut LN [3]. Nonetheless, there are many different LN cuts and orientations available on different substrates thanks to the advancement in thin film technology. It would be very interesting to explore these cuts for further improvement in the performance of Lamb wave resonators.

4.3   References

[1]   A. Lozzi, A. De Pastina, E. T. T. Yen, and L. G. Villanueva, "Engineered acoustic mismatch for anchor loss control in contour mode resonators," *Appl. Phys. Lett.*, vol. 114, no. 10, 2019.

[2]   B. Gibson, K. Qalandar, C. Cassella, G. Piazza, and K. L. Foster, "A Study on the Effects of Release Area on the Quality Factor of Contour-Mode Resonators by Laser Doppler Vibrometry," *IEEE Trans. Ultrason. Ferroelectr. Freq. Control*, vol. 64, no. 5, pp. 898–904, 2017.

[3]   V. P. Plessky, J. Koskela, and S. Yandrapalli, "Crystalline Y-cut Lithium Niobate Layers for the Bulk Acoustic Wave Resonator (YBAR)," in *2020 IEEE International Ultrasonics Symposium (IUS)*, 2020, pp. 1–4.

Appendix: Automatic Identification of S0 and SH0 modes in Eigen Frequency Analysis

In COMSOL, Eigen or Model frequency analysis is a quick way to observe the mode of vibration at the resonance frequency and calculate Q using real ($re(w)$) and imaginary ($im(w)$) parts of eigenvalues as:

$$Q = \frac{re(w)}{2.\,im(w)} \tag{A.1}$$

This can be done by simulating a number of modes (for example, 10 or 20) around the expected resonance frequency and manually plotting total displacement in the structure followed by visually selecting the required mode from the list of all the simulated modes. This process gets tedious and time consuming, if one needs to sweep a range of values of a geometrical dimension and calculate Q for each value by inspecting every simulated mode. Thus, we develop a selection protocol using COMSOL and Matlab for the automatic detection of S0 and SH0 modes from the list of large number of modes. It helps to study the influence of different geometrical parameters on Q of the resonator efficiently and accurately.

COMSOL is used to record the lateral displacement components (x for S0 mode and y for SH0 mode) for all the modes along the center-line of the resonator shown in Fig. A1 (a) and their respective eigen frequencies. Matlab is used to develop a selection criteria based on the data from COMSOL to identify the required mode. The periodic displacement of electrode fingers (Fig. A1 (b)) for S0 and SH0 modes gives sinusoidal behavior with the highest magnitude among the other modes. The selection criteria is as follows:

- Identify peaks in the displacement plot
- Verify that the number of peaks = the number of electrode fingers
- Compute amplitude ratio of peaks with respect to their mean $\frac{u_{peaks}}{mean(u_{peaks})}$
- Find the modes for which the amplitude ratio for all peaks is in the interval [0.5 1.5]
- Select the mode with the highest amplitude ratio as the intended S0 or SH0 mode
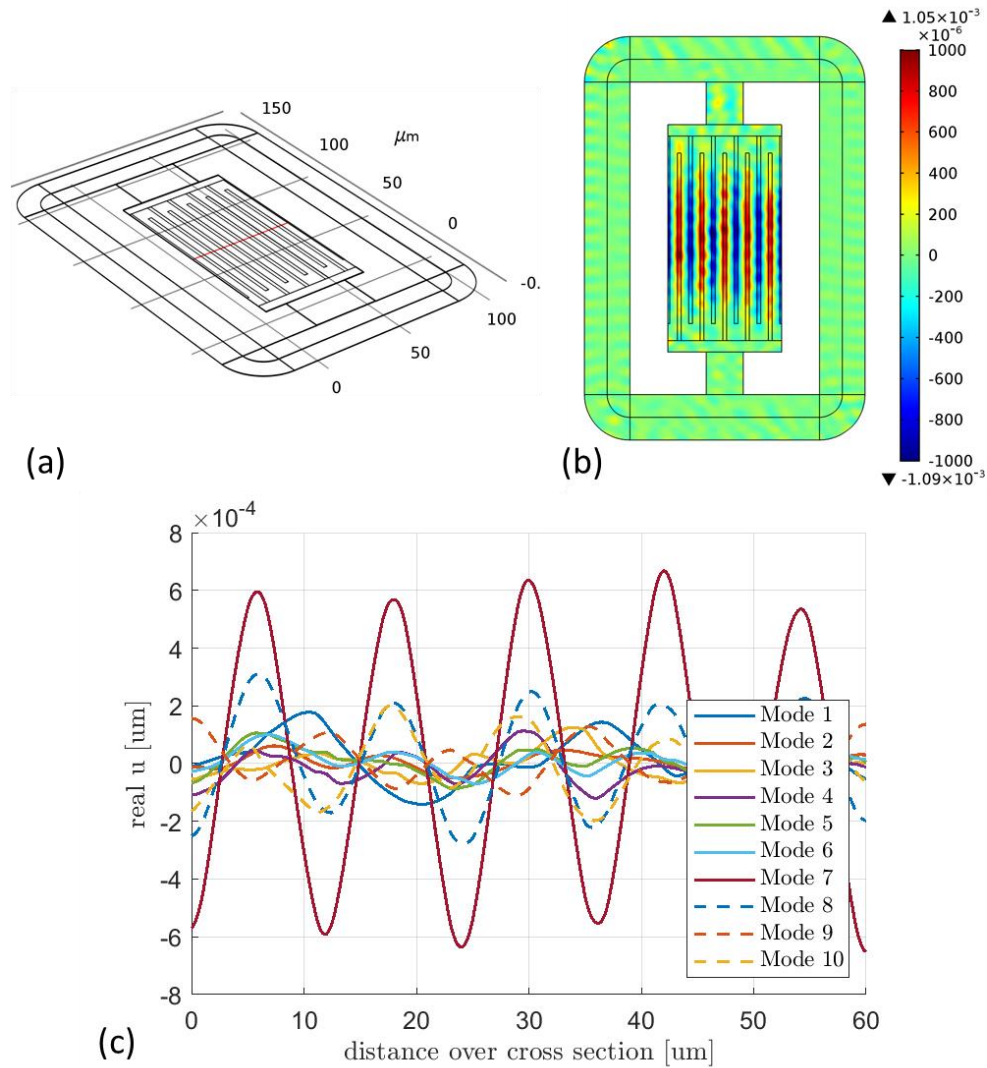
Figure A: (a) Centre-line where the displacement values are recorded for the selection criteria. (b) FEM model showing the periodic displacement of electrode fingers for S0 and SH0 modes. (c) Displacement plot for 10 different modes where mode 7 fulfils the selection criteria and is selected as the correct mode.

Inputs to the Matlab code:

       CSV file containing Eigen values for all the modes

       TXT file containing the x and y displacement values for all the modes

```
%% Code made my Christine ROTH (Semester project)
clear; close all;
set(0,'DefaultFigureColormap',feval('jet'));

%REQUIRED INPUTS
    N_FINGERS=9; %complete fingers!
    last_row_excel=1325;
%% IMPORT FILES
```

116

```matlab
%THIS IS THE DATA EXTRACTED USING THE TABLE EVALUATION_GLOBAL
%YOU HAVE TO MANUALLY INSERT THE INDEX OF THE LAST LINE IN THE EXCEL SHEET
%Import
        [~, ~, raw] =
xlsread('BC_DATA_GLOBAL_ALL.xlsx','1',sprintf('A6:H%i',last_row_excel));
        stringVectors = string(raw(:,4));
        stringVectors(ismissing(stringVectors)) = '';
        raw = raw(:,[1,2,3,5,6,7,8]);
        data = reshape([raw{:}],size(raw));
    % Allocate imported array to column variable names
        par_anchor_w = data(:,1);
        par_anchor_l = data(:,2);
        foi = data(:,3);
        lambdaHz = stringVectors(:,1);
        real1s = data(:,4);
        imag1s = data(:,5);
        NDOF = data(:,6);
        Q = data(:,7);
    % Clear temporary variables
    clearvars data raw stringVectors lambdaHz foi last_row_excel;
    disp('IMPORT TABLE DATA DONE')
%% THIS IS THE LINE DATA IN THE MODEL ANALYSIS EXTRACTED FROM THE 1D PLOT
% Be aware that the x coordinate needs to be 0 in the beginning of the
% curve (this is parametrized, but in case you edit, it could be lost.)
    %Import
        filename = 'BC_DATA_LINE_ALL.txt';
        delimiter = {'\t',' '};
        startRow = 9;
        formatSpec = '%f%f%*s%*s%*s%*s[^\n\r]';
        fileID = fopen(filename,'r');
        dataArray = textscan(fileID, formatSpec, 'Delimiter', delimiter,
'MultipleDelimsAsOne', true, 'TextType', 'string', 'EmptyValue', NaN, 'HeaderLines'
,startRow-1, 'ReturnOnError', false, 'EndOfLine', '\r\n');
        fclose(fileID);
    % Allocate imported array to column variable names
        cln2x = dataArray{:, 1};
        cln2x_realu = dataArray{:, 2};
    % Clear temporary variables
        clearvars filename delimiter startRow formatSpec fileID dataArray ans;
%% POSTPROCESSING OF LINE DATA
% cln2x are the line x coordinates and cln2x_realu the y coordinates
% they are one after another, but as they all start with 0 we can seperate
% them. Check at the end, that the dimensions match with the ones from the
% GLOBAL import!
    %find starting point of each curve set
        zero=find(cln2x==0);
% README! DATASTORAGE
    %all data will be combined in a single structure called SOLUTIONS. To
    %acess is, you can use SOLUTIONS(a).attribute(b). Dimensions can vary.
    %the number(a) coresponds to the geometry/solution number in comsol, b
    %is the access using table indices.
    %the function horcat and vertcat, allow to evaluate several structure
    %elements at once. It is used several times.
        SOLUTIONS=struct;
    %for each curve
    for i=1:length(zero)
        %if it is the first of 10 modes assign the right x coordinates to the
solution number.
        %uncomment to check all curves in figures!
        if mod(i,10)==1
            j=1;
            set=floor(i/10)+1;
            %figure(floor(i/10)+1);hold on;
```

```matlab
                %xlabel 'distance over cross section [um]';
                %ylabel 'real u';
                SOLUTIONS(set).x=0:1:60;
                SOLUTIONS(set).realu=zeros(length(SOLUTIONS(set).x),10);
            end
            %ind are the indices in the vector cln2x corresponding to the
            %currently treated set.
            try
                ind=zero(i):zero(i+1)-1;
            catch
                ind=zero(i):length(cln2x);
            end
            %we interpolate the curves to have all the times the same number of
            %points, independent of the mesh.
                %plot(cln2x(ind),cln2x_realu(ind),'DisplayName',sprintf('Mode
%i',mod(i,10)))

SOLUTIONS(set).realu(:,j)=interp1(cln2x(ind),cln2x_realu(ind),SOLUTIONS(set).x);
                j=j+1;
                legend;
        end
    clearvars ans i ind j set zero cln2x cln2x_realu;
    disp('IMPORT and TREATMENT LINE DATA DONE')
    save('all_data.mat')
%}
%% ASSING GLOBAL DATA TO SOLUTION
%%{
% number of degrees of freedon is used to split the data as it is unique
% for each geometry. If this has error, use dimensions instead
    [NDOF_unique ind]=unique(NDOF,'stable');
    for i=1:length(ind)
        SOLUTIONS(i).NDOF=NDOF(ind(i));
        SOLUTIONS(i).par_anchor_l=par_anchor_l(ind(i));
        SOLUTIONS(i).par_anchor_w=par_anchor_w(ind(i));
        SOLUTIONS(i).Q=Q(NDOF==NDOF(ind(i)))';
        SOLUTIONS(i).realf=real1s(NDOF==NDOF(ind(i)))';
        SOLUTIONS(i).imagf=imag1s(NDOF==NDOF(ind(i)))';
    end
disp('HOW to access SOLUTIONS:')
disp('SOLUTIONS(geometry number).attribute(lines vector, colums number of mode)')
%}
%% IDENTIFICATION OF S0
%%{
    nanmodes=[];
    clear m_interest maximum_u_real_in_i
% for all geometries m
    for m=1:size(SOLUTIONS,2)
        % we analyse the real displacement curves on the centerline of the
        % device
            interest=SOLUTIONS(m).realu;
        % possible modes with regularity criterion
            keep=[];
            keep_amp=[];
    %for all 10 modes per geometry
        for i=1:10
            %identify peaks
            [c d]=findpeaks(abs(interest(:,i)));
            %find meanratio between peak value and mean of all peaks
            meanratio=c./mean(c);
            %there should be as many peaks as fingers
            if length(c)==N_FINGERS;
                %the relative amplitude should be similar
                if ((min(meanratio)>0.5)&(max(meanratio)<1.5))
```

118

```matlab
                    keep=[keep i];
                    keep_amp=[keep_amp max(c)];
                end
            end
        end
    %from the regular curves with the correct number of peaks, we keep the
    %one with the highest amplitude, and discard all others.
        if length(keep)>0
            SOLUTIONS(m).S0=keep(keep_amp==max(keep_amp));
            SOLUTIONS(m).Q_S0=SOLUTIONS(m).Q(SOLUTIONS(m).S0);
            SOLUTIONS(m).freq=SOLUTIONS(m).realf(SOLUTIONS(m).S0);
        else
            SOLUTIONS(m).S0=nan;
            SOLUTIONS(m).Q_S0=nan;
            SOLUTIONS(m).freq=nan;
            nanmodes=[nanmodes;SOLUTIONS(m).par_anchor_w SOLUTIONS(m).par_anchor_l];
        end
    end
% extract from the nanmodes the maximum displacement for easy verification
% in comsol (use this values to scale plots
    for i=1:size(nanmodes,1)

m_interest(i)=find((vertcat(SOLUTIONS.par_anchor_w)==nanmodes(i,1))&(vertcat(SOLUTIO
NS.par_anchor_l)==nanmodes(i,2)));
        maximum_u_real_in_i(i)=max(max(abs(SOLUTIONS(m_interest(i)).realu)));
    end

    disp('IDENTIFICATION SH0 DONE, non-identifyable geometries were:')
    disp('par_anchor_w par_anchor_l m_interest')
    horzcat(nanmodes, m_interest',maximum_u_real_in_i')


%% PLOT RESULTS

SOLUTIONS(79).Q_S0=NaN
%%{
l=unique(vertcat(SOLUTIONS.par_anchor_l),'stable');
w=unique(vertcat(SOLUTIONS.par_anchor_w),'stable');
[ww,ll]=meshgrid(w,l);

%Quality factor S0
    figure(1000);
        interest=reshape(vertcat(SOLUTIONS.Q_S0),size(ww));
        surf(ww,ll,interest,'DisplayName','Quality',...
         'LineWidth',2,'EdgeColor','interp',...
            'FaceColor','none');
        xlim([0,max(w)]);
            ylim([0,max(l)]);
            %zlim([0, 30000]);
            caxis([0, 12000]);
            %set(gca, 'DataAspectRatio', [diff(get(gca, 'XLim')) diff(get(gca,
'XLim')) diff(get(gca, 'ZLim'))])
            caxis([0, 4000]);
            colorbar;
            %caxis([min(min(interest)), max(max(interest))]); colorbar();
        xlabel 'w [x wavelength]'; ylabel 'l [x wavelength]'; zlabel 'Q SH0'
    %title 'WITH BC: SH0 Quality'
%Frequency (real) S0
    figure(1001);
        interest=reshape(vertcat(SOLUTIONS.freq),size(ww));
        surf(ww,ll,interest,'DisplayName','Frequency',...
             'LineWidth',2,'EdgeColor','interp',...
            'FaceColor','none');
```

```matlab
        xlim([0,max(w)]);
            ylim([0,max(l)]);
            zlim([2.60e8, 6e8]);
            caxis([min(min(interest)), max(max(interest))]);    colorbar();
        xlabel 'w [x wavelength]'; ylabel 'l [x wavelength]'; zlabel 'Frequency SH0'
    title 'WITH BC: SH0 Frequency'
%Identification number of frequency for COMSOL
    figure(1002); hold on; grid on;
        DATA=vertcat(SOLUTIONS.S0);
        interest=reshape(DATA,size(ww));
        s=surf(ww,ll,interest,'DisplayName','NO of MODE',...
        'LineWidth',2,'EdgeColor','interp',...
            'FaceColor','none');
        %scatter3(w,l,DATA,[],C,'filled');
        xlim([0,max(w)]);
            ylim([0,max(l)]);
            zlim([0, 10]);
        caxis([0.5, 10.5]); colorbar;
        xlabel 'w [x wavelength]'; ylabel 'l [x wavelength]'; zlabel 'NUMBER SH0'
        view(2)
    title 'WITH BC: SH0 no of identified SH0 mode'
    %%
        % Save plots as figures and png
        for i=1000:1002
            figure(i);
            view(2);
                set(gcf, 'units', 'centimeters', 'pos', [0 0 10 10]);
                saveas(gcf,sprintf('1_figure%g_2D_BC.png',i))
                saveas(gcf,sprintf('1_figure%g_2D_BC.fig',i))
                saveas(gcf,sprintf('1_figure%g_3D_BC.eps',i))
            view(3);
                set(gcf, 'units', 'centimeters', 'pos', [0 0 15 10]);
                saveas(gcf,sprintf('1_figure%g_3D_BC.png',i))
                saveas(gcf,sprintf('1_figure%g_3D_BC.fig',i))
                saveas(gcf,sprintf('1_figure%g_3D_BC.eps',i))
        end
            view(2)
%}
%% Isolate geometries that are of further interest from graphs
%%{
interest_sweep=horzcat(vertcat(SOLUTIONS(find(vertcat(SOLUTIONS.Q_S0)>7290)).par_anc
hor_w),...
    vertcat(SOLUTIONS(find(vertcat(SOLUTIONS.Q_S0)>7290)).par_anchor_l),...
    vertcat(SOLUTIONS(find(vertcat(SOLUTIONS.Q_S0)>7290)).Q_S0));

[w_interest]=unique(interest_sweep(:,1),'stable');
interest_geometries=[];
for w=w_interest'
    Q_interest=max(interest_sweep(interest_sweep(:,1)==w,3));
    interest_geometries=[interest_geometries;...
        interest_sweep(interest_sweep(:,3)==Q_interest,1),...
        interest_sweep(interest_sweep(:,3)==Q_interest,2)];
end
disp('par_anchor_w par_anchor_l')
interest_geometries=[interest_geometries; nanmodes(:,1:2)]
%}
BC_SOLUTIONS=SOLUTIONS;
disp('TREATMENT IS DONE')
save('SOLUTIONS_V6_MODEL','BC_SOLUTIONS')
```

Photographic credits

- Fig. 1.1a-b: Ericsson, "Mobile network traffic Q1 2020 – Mobility Report," 2020. [Online]. Available: https://www.ericsson.com/en/mobility-report/reports/june-2020/mobile-traffic-q1. [Accessed: 30-Nov-2020].

- Fig. 1.1c: Yole, "5G impact on RF Front End Modules & Connectivity for Cellphones," 2018.

- Fig. 1.1d: Yole, "STATUS OF THE MEMS INDUSTRY 2018- Market & Technology report," 2018.

- Fig. 1.2: J. Iannacci, "Expectations versus actual market of RF-MEMS: Analysis and explanation of a repeatedly fluctuating scenario," in *RF-MEMS Technology for High-Performance Passives.* , IOP Publishing.

- Fig. 1.9: Y. Yang, R. Lu, T. Manzaneque, and S. Gong, "Toward Ka Band Acoustics: Lithium Niobate Asymmetrical Mode Piezoelectric MEMS Resonators," *IFCS 2018 - IEEE Int. Freq. Control Symp.*, pp. 1–5, 2018.

Curriculum Vitae

Muhammad Faizan

Chemin du Calvaire 19,
Lausanne 1005, Switzerland.
Nationality: Pakistani
Contact: +41779925808
Email: faizan_nust@yahoo.com

Summery:

An Electrical Engineer with 5 years of experience in MEMS conception, design, fabrication and testing with rigorous and creative problem solving approach, combined with the ability to work in international teams.

Work Experience:

Doctoral researcher at "EPFL, Switzerland", from Feb 2017 – To date
- Design, fabrication and characterization of Bulk acoustic resonators for RF filters and oscillators.
- $2 \times$ enhancement in device performance compared to the state of the art for lithium niobate based lamb wave resonators.
- Development and optimization of multiple fabrication process flows to achieve maximum device yield and uniformity.
- Electrical and optical characterization of MEMS devices.
- Proficient in Matlab, ADS, COMSOL, ANSYS Structural Mechanics, HFSS and MAXWELL simulation softwares.

Assistant Manager at "National Electronics Complex of Pakistan", from Feb 2013 – August 2014
- Development of OFDM Transceiver on National Instruments PXIe-1075 & 1085 equipment.
- Algorithm development for Buried Cable Intrusion Detection System on LabView and Matlab.
- Hands on experience in signal processing algorithm development, modeling & implementation of communication systems and radio link designing.

Cleanroom Experience (5 Years):

Fabrication of MEMS/NEMS devices
- Hands on experience in E-beam and photo-lithography techniques, dry etching, wet etching, ultra-thin multilayers deposition, wire bonding and wafer dicing.
- Proficient in working with piezoelectric materials such as aluminum nitride, aluminum scandium nitride and lithium niobate.
- Experience in handling and working with different polymers (ECI 3007, SU-8, ZEP, PMMA etc.).

Manufacturing of Microfluidics Chips via Silicon Wafer Master
- Hands-on experience in master fabrication, PDMS casting, degassing, molding, cutting and bonding.

Characterization of Microsystems
- Proficient in characterization of micro devices using Scanning Electron microscope (SEM), X-Ray Diffraction, AC/DC Probe station, Spectroscopic Reflectometer, Optical Microscope, Profilometer and Interferometer.

Educational Qualifications:

2017-2020   PhD in Microsystems and Microelectronics
Specialization: Microelectromechanical systems (MEMS)
Swiss Federal Institute of Technology at Lausanne (EPFL), Switzerland

2014-2016   MSc in Smart Systems Integration (**Erasmus Mundus Course**)
Specialization: Microelectromechanical systems (MEMS)
Heriot Watt University, United Kingdom
Overall Grade: Passed with Distinction

2008-2012   B.E in Electrical Engineering
Specialization: Telecommunication
National University of Sciences and Technology (NUST), Pakistan
GPA: 3.61/4.0 (A+)

Completed Projects:

- Design and development of Microwave Sampling Beam-former Receiver at 5.8 GHz.
- Design, fabrication and characterization of Piezoelectric NEMS Resonator for mass sensors
- Modelling of CMOS compatible MEMS Tactile sensor and its readout circuitry on ANSYS Multiphysics.
- Modelling of car crash airbag deployment system consisting of a MEMS sensor, an analog signal conditioning circuit and digital signal processing unit.

Selected Scientific Publications:

- Frequency-scalable fabrication process flow for lithium niobate based Lamb wave resonators
Faizan et al, J. Micromech. Microeng. 30 015008
DOI: 10.1088/1361-6439/ab5b7b

- Fabrication Of Lithium Niobate Bulk Acoustic Resonator For 5G Filters
Faizan et al, Transducers 2019
DOI: 10.1109/TRANSDUCERS.2019.8808179

- Laterally excited bulk wave resonators (XBARs) based on thin Lithium Niobate platelet for 5GHz and 13 GHz filters
Plessky et al, IMS 2019
DOI: 10.1109/MWSYM.2019.8700876

Achievements:

- Awarded Erasmus Mundus Scholarship (worth €47,500) for master degree by the European Union (2014-2016).
- Awarded performance based merit scholarship for bachelor degree by the National University of Sciences and Technology, Pakistan (2008-2012).